

University of Windsor

## Scholarship at UWindsor

---

Electronic Theses and Dissertations

Theses, Dissertations, and Major Papers

---

2009

### Improving the Corrosion Resistance of a High-Strength Aluminum-Copper Casting Alloy

Madhavan Manivannan  
*University of Windsor*

Follow this and additional works at: <https://scholar.uwindsor.ca/etd>

---

#### Recommended Citation

Manivannan, Madhavan, "Improving the Corrosion Resistance of a High-Strength Aluminum-Copper Casting Alloy" (2009). *Electronic Theses and Dissertations*. 7891.  
<https://scholar.uwindsor.ca/etd/7891>

This online database contains the full-text of PhD dissertations and Masters' theses of University of Windsor students from 1954 forward. These documents are made available for personal study and research purposes only, in accordance with the Canadian Copyright Act and the Creative Commons license—CC BY-NC-ND (Attribution, Non-Commercial, No Derivative Works). Under this license, works must always be attributed to the copyright holder (original author), cannot be used for any commercial purposes, and may not be altered. Any other use would require the permission of the copyright holder. Students may inquire about withdrawing their dissertation and/or thesis from this database. For additional inquiries, please contact the repository administrator via email ([scholarship@uwindsor.ca](mailto:scholarship@uwindsor.ca)) or by telephone at 519-253-3000ext. 3208.

**Improving the Corrosion Resistance of a High-Strength Aluminum-Copper Casting Alloy**

**By**

**Madhavan Manivannan**

**A Thesis**

**Submitted to the Faculty of Graduate Studies  
through the Department of Mechanical, Automotive and  
Materials Engineering in Partial Fulfillment of the  
Requirements for the Degree of Master of Applied Science at the  
University of Windsor**

**Windsor, Ontario, Canada  
2009**

**© 2009 Madhavan Manivannan**

## DECLARATION OF CO-AUTHORSHIP /PREVIOUS PUBLICATION

This thesis includes [ISSN. 1442-0139, Paper 019] original paper that has been previously published in peer reviewed conference proceedings, as follows:

Thesis Chapter	Publication title	Publication status*
Chapter 4	M. Manivannan., J.H. Sokolowski and D.O. Northwood, An investigation of the effect of various heat treatments on the corrosion resistance of a high-strength Aluminum-Copper casting alloy, Corrosion & Prevention 2008, Wellington, New Zealand, November 16-19, 2008. Conference Proceedings, ISSN. 1442-0139, Paper 019, p. 1-10	published

I hereby declare that this thesis incorporates the outcome of a joint research under the supervision of Dr. Jerry H. Sokolowski and Dr. Derek O. Northwood. I am aware of the University of Windsor Senate Policy on Authorship and I certify that I have properly acknowledged the contribution of other researchers to my thesis, and have obtained written permission from each of the co-authors to include the above material in my thesis.

I certify that, with the above qualification, this thesis, and the research to which it refers, is the product of my own work.

I certify that I have obtained a written permission from the copyright owner(s) to include the above published material(s) in my thesis. I certify that the above material describes work completed during my registration as graduate student at the University of Windsor.

I declare that, to the best of my knowledge, my thesis does not infringe upon anyone's copyright nor violate any proprietary rights and that any ideas, techniques, quotations, or any other material from the work of other people included in my thesis,

published or otherwise, are fully acknowledged in accordance with the standard referencing practices. Furthermore, to the extent that I have included copyrighted material that surpasses the bounds of fair dealing within the meaning of the Canada Copyright Act, I certify that I have obtained a written permission from the copyright owner(s) to include such material(s) in my thesis.

I declare that this is a true copy of my thesis, including any final revisions, as approved by my thesis committee and the Graduate Studies office, and that this thesis has not been submitted for a higher degree to any other University of Institution.

## **ABSTRACT**

The B206 alloy (up to 5 wt% Cu) is the strongest aluminum foundry alloy in current use. B206 alloy can be used in a number of automotive applications, e.g. suspension knuckles and vehicle control arms, to reduce vehicle weight. Elimination of hot tearing has reawakened the interest in the 206 alloy family. However, the B206 alloy is susceptible to intergranular/pitting corrosion which restricts its current applications.

A heterogeneous distribution of Cu-containing intermetallic precipitates in the as-cast condition resulted in severe intergranular corrosion. The improved 3-step ST + 2-step AA provides better corrosion resistance compared to 2-step ST + 1-step AA. Longer first step AA time eliminated intergranular corrosion but resulted in low level pitting corrosion. The elongation was found to decrease with the increase in AA temperature and time. It is difficult to obtain both excellent corrosion resistance and elongation ( $\geq 10\%$ ) for the overaged condition.

## **ACKNOWLEDGEMENTS**

1. The author wishes to express his sincere gratitude to Dr. Derek O. Northwood and Dr. Jerry H. Sokolowski for their support, supervision and valuable discussions throughout this work.
2. This research was funded by AUTO21, a member of the Network of Centres of Excellence of Canada program, United States Council for Automotive Research (USCAR) through Dr. J. H. Sokolowski and the Natural Sciences and Engineering Research Council of Canada (NSERC) through a Discovery Grant awarded to Dr. D. O. Northwood.
3. I would like to sincerely thank all the collaborators in this thesis project especially from Dr. W. Kasprzak, Marta Aniolek, Mr. Blair Warnock, Dr. J. Fred Major (from Novelis), Dr. Geoffrey K. Sigworth & Eric McCarty (USCAR representatives), Dr. J. Szpunar & Mr. N.A.P. Kiran Kumar (McGill University) for their technical support. Thanks are also given to Dr. Glenn Byczynski & Dr. Robert Mackay (from Nemak). I greatly appreciate the valuable opportunities and assistance received from the Nemak of Canada Corporation, Windsor.
4. I would like to extend my thanks to the Advisory Committee Dr. Paul Henshaw, Dr. Xueyuan Nie and Dr. Henry Hu for their support.
5. I wish to express my appreciation to Ms. Ellen Moosberger and Ms. Barbara Tattersall for their assistance. Also the assistance of Mr. J. Robinson and the entire Technical Support Centre (U of W) was invaluable. Thanks to Mr. Daniel Szablewski and Mr. Nathan D. Reade for their support during my studies. I also wish to acknowledge the SEM analysis work from JEOL.

## TABLE OF CONTENTS

<b>DECLARATION OF CO-AUTHORSHIP/PREVIOUS PUBLICATION.....</b>	<b>iii</b>
<b>ABSTRACT.....</b>	<b>v</b>
<b>ACKNOWLEDGEMENTS.....</b>	<b>vi</b>
<b>LIST OF TABLES.....</b>	<b>xi</b>
<b>LIST OF FIGURES.....</b>	<b>xiii</b>
<b>LIST OF ABBREVIATIONS.....</b>	<b>xxii</b>
<b>CHAPTER</b>	
<b>1: INTRODUCTION.....</b>	<b>1</b>
1.1 General Background.....	1
1.2 Objectives.....	2
<b>2: LITERATURE REVIEW.....</b>	<b>3</b>
2.1 Introduction.....	3
2.2 Key Alloying and Impurity elements.....	4
2.2.1 Copper.....	4
2.2.2 Manganese.....	4
2.2.3 Magnesium.....	5
2.2.4 Silicon.....	5
2.2.5 Iron.....	5
2.2.6 Tin.....	6
2.2.7 Titanium.....	6
2.2.8 Nickel.....	6
2.3 History of Casting Al-Cu alloy.....	6
2.3.1 Al-Cu phase diagram.....	6
2.3.1.1 B206 alloy.....	7
2.3.1.2 Solidification reactions of 206.2 alloy.....	8
2.4 Casting Technology.....	8
2.4.1 Permanent Mold Casting Process.....	8
2.4.2 Hot-cracking of Al-Cu-Mn-Mg alloy.....	9
2.4.2.1 Effect of Silicon on the fluidity and hot cracking of Aluminum-Copper alloy.....	9

2.4.2.2 Fatigue crack growth in cast Al-Cu alloy A206 with different levels of porosity.....	10
2.5 Heat Treatment of Al-Cu alloys.....	10
2.5.1 Solution Treatment.....	10
2.5.2 Precipitation hardening.....	11
2.5.3 Natural Aging.....	12
2.5.4 Artificial Aging (AA).....	12
2.5.4.1 Single stage Artificial Aging (AA).....	12
2.5.4.2 Multi-stage Artificial Aging (AA).....	14
2.5.5 Effect of Si on the microstructure and mechanical properties of Al-4.5%Cu alloys.....	16
2.5.6 Effect of Cu and Si on mechanical properties in Al-Cu-Si-Mg alloys.....	17
2.5.7 Chemistry/Property relationship in AA206 alloy.....	18
2.5.8 Mechanical properties of B206 alloy.....	18
2.6 Corrosion of Al-Cu alloys.....	19
2.6.1 Immersion testing of heat treated 201 alloys in NaCl/H <sub>2</sub> O <sub>2</sub> corrosive solution.....	20
2.6.2 Stress Corrosion Cracking.....	21
2.6.2.1 Intergranular stress corrosion behaviour of Al-Cu-Mg-Ag alloys.....	21
2.6.2.2 Pitting corrosion of Al-Cu alloys.....	23
2.6.2.3 Copper redeposition during the dissolution in NaCl solution.....	25
2.6.2.4 Effect of quench delay time on corrosion behaviour of Al 2024 alloy....	26
2.6.2.5 Stress Corrosion Cracking (SCC) after 2-step aging.....	26
2.7 Quality index of Al alloys.....	27
2.7.1 Caceres analytical model.....	27
2.7.2 Quality index by Murat Tiryakioglu.....	29
2.7.3 Ductility potential of 206 alloys.....	30
2.7.4 Quality index of B206 alloy.....	31
<b>3: EXPERIMENTAL DETAILS.....</b>	<b>32</b>
3.1 Tensile test bar casting.....	32
3.1.1 Chemical Composition of B206 alloy specimens.....	32
3.2 UMSA platform.....	33
3.3 First Series Heat Treatment.....	35



3.3.1 2-step Solution Treatment (ST).....	35
3.3.2 Natural Aging (NA) followed by 1-step Artificial Aging (AA).....	36
3.4 Second Series Heat Treatment.....	38
3.5 Third Series Heat Treatment.....	38
3.5.1 Modified 3-step Solution Treatment.....	38
3.5.2 Aging (Natural + Artificial).....	39
3.6 Corrosion Test Sample Preparation.....	42
3.7 Corrosion Testing Methods.....	42
3.7.1 Immersion corrosion Testing.....	42
3.7.2 Potentiodynamic Testing.....	43
3.7.3 Tribocorrosion tests.....	44
4: RESULTS AND DISCUSSIONS.....	47
4.1 As-cast Structure analysis before the immersion corrosion test.....	47
4.2 As-cast Structure analysis after the immersion corrosion test.....	51
4.3 Metallographic Analysis of corrosion mode and severity for First Series Heat Treatment conditions.....	54
4.4 Mechanical Properties analysis for second series heat treatments.....	64
4.5 Metallographic Analysis for third series heat treatments.....	66
4.5.1 Heat Treatment and corrosion test data for the machined samples.....	66
4.5.2 Heat Treatment and corrosion test data for the non machined samples.....	70
4.6 Comparison of immersion corrosion behaviour of heat treated samples subjected to 2 vs. 3-step ST and 1 vs. 2-step AA (with & without NA).....	75
4.7 Analysis of mechanical properties for third series heat treatments.....	76
4.7.1 Comparison of UTS, YS for 3-step ST, NA (0 & 24 hrs), 2-step AA and 2-step ST, NA (72 hrs), 1-step AA.....	77
4.7.2 Effect of total aging (NA and AA) time on YS and elongation on for third series heat treatments.....	78
4.7.3 Comparison of mechanical properties & corrosion resistance for the Third Series Heat Treatment Experiments.....	79
4.8 SEM fracture analysis of the tensile test bars subjected to 3-step ST & 2-step AA conditions (with & without NA).....	83
4.9 Quality Index of B206 alloy subjected to 3-step ST, NA (0&24h), & 2-step AA.....	89
4.9.1 True stress-strain curves.....	89

4.9.2 K & n values.....	94
4.9.3 Quality index plot.....	95
4.10 Potentiodynamic Polarization testing.....	96
4.10.1 SEM examination of selected specimens from potentiodynamic corrosion testing.....	98
4.10.2 Comparison of potentiodynamic and immersion testing.....	100
4.10.3 SEM & Optical Metallography (OM) showing the relationship between the distributions of Cu-intermetallics and intergranular corrosion.....	102
4.11 Tribocorrosion testing.....	104
4.11.1 Dry Wear Test.....	104
4.11.2 Wear in a Corrosive Medium.....	105
4.11.3 Open Circuit Potential (OCP) Measurements.....	108
5: SUMMARY AND CONCLUSIONS.....	109
6: RECOMMENDATIONS FOR FUTURE WORK.....	112
REFERENCES.....	113
PUBLICATIONS RESULTING FROM THIS WORK.....	122
VITA AUCTORIS.....	123

## LIST OF TABLES

<b>Table 2.1:</b> Registered B206.0 alloy composition.....	7
<b>Table 2.2:</b> Formation of various phases during the solidification process in a B206 alloy.....	8
<b>Table 2.3:</b> Mechanical properties of Al-4.5%Cu alloys with Si addition.....	16
<b>Table 2.4:</b> Mechanical properties of the alloys after T4 heat treatment.....	17
<b>Table 2.5:</b> Effect of Cu content of Al-Cu-Si-Mg alloys on mechanical properties.....	17
<b>Table 2.6:</b> Effect of Si content of Al-Cu-Si-Mg alloys on mechanical properties.....	17
<b>Table 2.7:</b> Heat treatments applied to the tensile samples used in constructing Fig. 2.16.....	29
<b>Table 2.8:</b> The datasets used for yield strength-elongation relationship.....	31
<b>Table 3.1:</b> Chemical Composition of B206 alloy specimens.....	32
<b>Table 3.2:</b> Heating cycle of the B206 alloy.....	35
<b>Table 3.3:</b> Cooling cycle of the B206 alloy.....	35
<b>Table 3.4</b> 3-step Solution Treatment (ST) schedule .....	39
<b>Table 3.5</b> Natural Aging (NA) (0 and 24 hrs) followed by one step Artificial Aging (AA) performed at 175°C for 12 hrs .....	39
<b>Table 3.6</b> Summary of Natural Aging (NA) and Artificial Aging (AA) parameters for machined samples: Natural Aging (NA) (0 hrs and 24 hrs) followed by a two step Artificial Aging (AA) treatment .....	40
<b>Table 4.1:</b> X-ray microanalysis quantitative data for Fig. 4.2.....	49

<b>Table 4.2: X-ray microanalysis quantitative data for Fig. 4.3.....</b>	<b>50</b>
<b>Table 4.3: X-ray microanalysis quantitative data for Fig. 4.5a).....</b>	<b>53</b>
<b>Table 4.4: Corrosion results for the first series heat treatments.....</b>	<b>59</b>
<b>Table 4.5: X-ray microanalysis quantitative data for Fig. 4.12a).....</b>	<b>62</b>
<b>Table 4.6: X-ray microanalysis quantitative data for Fig. 4.14a).....</b>	<b>64</b>
<b>Table 4.7: Summary of corrosion data for the machined B206 samples.....</b>	<b>67</b>
<b>Table 4.8: Summary of corrosion data for the non machined B206 samples.....</b>	<b>71</b>
<b>Table 4.9: Summary of mechanical properties for third series heat treated B206 alloy.....</b>	<b>76</b>
<b>Table 4.10: n and K values for the third series heat treated samples.....</b>	<b>94</b>
<b>Table 4.11: Results of potentiodynamic corrosion testing.....</b>	<b>97</b>
<b>Table 4.12: Comparison of potentiodynamic polarization testing with the immersion testing and mechanical property results.....</b>	<b>101</b>
<b>Table 4.13: Results of wear track width.....</b>	<b>105</b>
<b>Table 4.14: Results of wear track width (in the presence of corrosive medium).....</b>	<b>107</b>
<b>Table 4.15: Coefficient of friction measured during corrosive wear.....</b>	<b>107</b>

## LIST OF FIGURES

<b>Figure 2.1:</b> Aluminum rich portion of the Al-Cu phase diagram.....	7
<b>Figure 2.2:</b> Microstructure of B206 alloys (a) grains (b) interconnected dendrites.....	8
<b>Figure 2.3:</b> a) Variation of fluidity with different contents of Si. b) Variation of hot cracking tendency with different contents of Si.....	9
<b>Figure 2.4:</b> Effect of artificial aging on elongation for duralumin (artificial aging was applied immediately after quenching from about 510°C.....	13
<b>Figure 2.5:</b> Effect of artificial aging on elongation for duralumin (artificial aging was applied after complete age-hardening at room temperature for 5 days.....	14
<b>Figure 2.6:</b> Effect of artificial aging on elongation for duralumin (artificial aging was applied after age-hardening at room temperature and cold-rolled.....	14
<b>Figure 2.7:</b> Schematic representation of the three stages of T6I6 interrupted aging treatment.....	15
<b>Figure 2.8:</b> Microstructure of the as-cast alloys: (a) Al-4.5%Cu-1%Si (b) Al-4.5%Cu-2%Si.....	16
<b>Figure 2.9:</b> Range of mechanical properties in five aluminum casting alloys.....	19
<b>Figure 2.10:</b> Intergranular corrosion characteristics of aged 201 alloy.....	20
<b>Figure 2.11:</b> (a) Shows an under-aged condition where the boundary has the heaviest concentration difference between Cu-depleted zones and the supersaturated matrix (b) Represents a peak-aged or over-aged condition where the Cu depletion zones around Cu-containing precipitates begin to overlap with each other not only at the boundaries but also in the matrix (c) Represents a schematic of the Cu-depleted matrix that would be associated with an extremely over-aged condition.....	22
<b>Figure 2.12:</b> Pit germination time distribution (25mm 2024 alloy, E = +300 mV/SCE, 0.0035 mol l <sup>-1</sup> Cl <sup>-</sup> ).....	24

<b>Figure 2.13:</b> Variation of pit germination rate with the chloride ion concentration E=300 mV/SCE; (a) 25 mm 2024 alloy (b) 1.6 mm 2024 alloy (c) 99.99% Al.....	24
<b>Figure 2.14:</b> (a), (c), (f) & (i) Al-3.84%Cu alloy in 0.5 M NaCl for five days.....	25
<b>Figure 2.15:</b> Cross section of the surface exposed to 3.5% NaCl pH=4 solutions (a) Quench delay time = 27 s. (b) Quench delay time = 81 s.....	26
<b>Figure 2.16:</b> A quality index chart and tensile data for the Al-Cu-Si-Mg alloy with (a) 0.1%Mg and (b) 0.5%Mg. The arrows indicate the strength-ductility path for samples.....	28
<b>Figure 2.17:</b> Yield strength-elongation relationship in 206 casting alloy. The highest point follows a curvilinear trend.....	30
<b>Figure 3.1:</b> B206 tensile tests bar.....	32
<b>Figure 3.2:</b> UMSA Platform at the University of Windsor.....	33
<b>Figure 3.3:</b> Temperature vs. Time curve of the UMSA Melting and Solidification Cycles for the B206 alloy.....	34
<b>Figure 3.4:</b> First derivative of the heating (melting) and cooling (solidification) curves vs. temperature for the B206 alloy.....	34
<b>Figure 3.5:</b> 2-step Solution Treatment and 1-step Artificial Aging Treatment.....	37
<b>Figure 3.6:</b> 3-step Solution Treatment and 2-step Artificial Aging Treatment.....	41
<b>Figure 3.7:</b> (a) Overall view of the UMSA test sample, (b) schematic drawing of the UMSA test sample.....	42
<b>Figure 3.8:</b> (a) specimen immersed in the corrosive solution, (b) corroded specimen.....	43
<b>Figure 3.9:</b> (a) Solarton 1285 potentiostat (b) 3-electrode setup.....	44
<b>Figure 3.10:</b> Tribocorrosion apparatus at McGill University.....	45

<b>Figure 3.11:</b> Overview of the heat treatments and its corresponding testing methods...	46
<b>Figure 4.1:</b> SEM micrographs of the as-cast B206 test sample before the immersion corrosion test.....	47
<b>Figure 4.2:</b> a) SEM micrograph of the as-cast B206 test sample before the immersion corrosion test b) X-Ray microanalysis spectrum.....	48
<b>Figure 4.3:</b> a) SEM micrograph of the as-cast B206 test sample before the immersion corrosion test.....	50
<b>Figure 4.4:</b> SEM micrographs of the as-cast B206 test sample after the immersion corrosion test.....	51
<b>Figure 4.5:</b> a) SEM micrograph of the as-cast B206 test sample after the immersion corrosion test b) X-ray microanalysis spectrum.....	52
<b>Figure 4.6:</b> LOM Micrographs: a) As-cast condition b) 2-step ST (493-504°C/2h, 527-532°C/8h, water quenching (66°C)) and NA 24 hrs c) 2-step ST (493-504°C/2h, 527-532°C/8h, water quenching (66°C)) and NA 168 hrs.....	54
<b>Figure 4.7:</b> LOM Micrographs: a) 2-step ST(493-504°C/2h, 527-532°C/8h, water quenching (66°C)) and AA @ 150°C/0.5hb) 2-step ST (493-504°C/2h, 527-532°C/8h, water quenching (66°C)) and AA @ 150°C/1h c) 2-step ST (493-504°C/2h, 527-532°C/8h, water quenching (66°C)) and AA @ 150°C/2h d) 2-step ST (493-504°C/2h, 527-532°C/8h, water quenching (66°C)) and AA @ 150°C/8h.....	55
<b>Figure 4.8:</b> LOM Micrographs: a) 2-step ST (493-504°C/2h, 527-532°C/8h, water quenching (66°C)), NA 24h and AA @ 160°C/5h b) 2-step ST (493-504°C/2h, 527-532°C/8h, water quenching (66°C)), NA 24h and AA @ 160°C/10h c) 2-step ST (493-504°C/2h, 527-532°C/8h, water quenching (66°C)), NA 24h and AA @ 160°C/24h d) 2-step ST (493-504°C/2h, 527-532°C/8h, water quenching (66°C)), NA 24h and AA @ 160°C/48h.....	56

**Figure 4.9:** LOM Micrographs: a) 2-step ST (493-504°C/2h, 527-532°C/8h, water quenching (66°C)), NA 24h and AA @ 180°C/2.5h b) 2-step ST (493-504°C/2h, 527-532°C/8h, water quenching (66°C)), NA 24h and AA @ 180°C/5h c) 2-step ST (493-504°C/2h, 527-532°C/8h, water quenching (66°C)), NA 24h and AA @ 180°C/10h d) 2-step ST (493-504°C/2h, 527-532°C/8h, water quenching (66°C)), NA 24h and AA @ 180°C/120h.....57

**Figure 4.10:** LOM Micrographs: a) 2-step ST (493-504°C/2h, 527-532°C/8h, water quenching (66°C)), AA @ 200°C/0.5h b) 2-step ST (493-504°C/2h, 527-532°C/8h, water quenching (66°C)), AA @ 200°C/1h c) 2-step ST (493-504°C/2h, 527-532°C/8h, water quenching (66°C)), AA @ 200°C/2h d) 2-step ST (493-504°C/2h, 527-532°C/8h, water quenching (66°C)), AA @ 200°C/3h e) 2-step ST (493-504°C/2h, 527-532°C/8h, water quenching (66°C)), AA @ 200°C/8h.....58

**Figure 4.11:** a), b), c), d), e) & f) SEM micrographs before immersion corrosion test.....60

**Figure 4.12:** a) SEM micrograph of the test sample (subjected to 2-step ST (493-504°C/2h, 527-532°C/8h, water quenching (66°C)) and AA @ 200°C/3h) before immersion corrosion test b) X-ray microanalysis spectrum.....61

**Figure 4.13:** SEM micrographs of the test sample (subjected to 2-step ST (493-504°C/2h, 527-532°C/8h, water quenching (66°C)) and AA @ 200°C/3h) after immersion corrosion test.....62

**Figure 4.14:** a) SEM/BSE micrograph of the test sample (subjected to 2-step ST (493-504°C/2h, 527-532°C/8h, water quenching (66°C)) and AA @ 200°C/3h) after the immersion corrosion test b) X-ray microanalysis spectrum.....63

**Figure 4.15:** Effect of Artificial Aging time on the Ultimate Tensile Strength (UTS) for the second series heat treatments involving 2-step ST, NA (3 days), and 1-step AA.....64

**Figure 4.16:** Effect of Artificial Aging time on the Yield Strength (YS) for the second series heat treatments involving 2-step ST, NA (3 days), and 1-step AA....65



**Figure 4.17:** Effect of Artificial Aging time on the elongation for the second series heat treatments involving 2-step ST, NA (3 days), and 1-step AA.....65

**Figure 4.18:** LOM Micrographs: a) 0-B-8: 3-step ST(515°C/3h,530°C/8, 535°C/4h, water quenching (66°C)), 2-step AA @ (190°C/0.5h, 50°C/1h (water quenching), 130°C/20h) b) 0-C-8: 3-step ST(515°C/3h,530°C/8, 535°C/4h, water quenching (66°C)), 2-step AA @ (190°C/0.5h, 50°C/1h (water quenching), 130°C/30h) c) 0-D-8: 3-step ST(515°C/3h,530°C/8, 535°C/4h, water quenching (66°C)), 2-step AA @ (190°C/4h, 50°C/1h (water quenching), 130°C/20h) d) 0-E-8: 3-step ST(515°C/3h,530°C/8, 535°C/4h, water quenching (66°C)), 2-step AA @ (190°C/4h, 50°C/1h (water quenching), 130°C/30h).....68

**Figure 4.19:** LOM Micrographs: a) 24-B-8 : 3-step ST(515°C/3h,530°C/8h, 535°C/4h, water quenching (66°C)), 24h NA, 2-step AA @ (190°C/0.5h, 50°C/1h (water quenching), 130°C/20h) b) 24-C-8 : 3-step ST(515°C/3h,530°C/8h, 535°C/4h, water quenching (66°C)), 24h NA, 2-step AA @ (190°C/0.5h, 50°C/1h (water quenching), 130°C/30h) c) 24-D-8 : 3-step ST(515°C/3h,530°C/8h, 535°C/4h, water quenching (66°C)), 24h NA, 2-step AA @ (190°C/4h, 50°C/1h (water quenching), 130°C/20h) d) 24-E-8 : 3-step ST(515°C/3h,530°C/8h, 535°C/4h, water quenching (66°C)), 24h NA, 2-step AA @ (190°C/4h, 50°C/1h (water quenching), 130°C/30h).....69

**Figure 4.20:** LOM Micrographs: a) 0-F-8: 3-step ST (515°C/3h, 530°C/8h, 535°C/4h, water quenching (66°C)), 1-step AA @ (175°C/12h) b) 24-F-8: 3-step ST 515°C/3h,530°C/8h, 535°C/4h, water quenching (66°C)), 24h NA, 1-step AA @ (175°C/12h).....70

**Figure 4.21:** LOM Micrographs: a) 0-B-8\*: 3-step ST (515°C/3h, 530°C/8, 535°C/4h, water quenching (66°C)), 2-step AA @ (190°C/0.5h, 50°C/1h (water quenching), 130°C/20h) b) 0-C-8\*: 3-step ST (515°C/3h, 530°C/8, 535°C/4h, water quenching (66°C)), 2-step AA @ (190°C/0.5h, 50°C/1h (water quenching), 130°C/30h).....72

**Figure 4.22:** LOM Micrographs: a) 0-D-8\*: 3-step ST (515°C/3h,530°C/8, 535°C/4h, water quenching (66°C)), 2-step AA @ (190°C/4h, 50°C/1h (water quenching), 130°C/20h) b) 0-E-8\*: 3-step ST (515°C/3h,530°C/8, 535°C/4h, water quenching (66°C)), 2-step AA @ (190°C/4h, 50°C/1h (water quenching), 130°C/30h) c) 24-B-8\*: 3-step ST (515°C/3h,530°C/8h, 535°C/4h, water quenching (66°C)), 24h NA, 2-step AA @ (190°C/0.5h, 50°C/1h (water quenching), 130°C/20h) d) 24-C-8\*: 3-step ST (515°C/3h,530°C/8h, 535°C/4h, water quenching (66°C)), 24h NA, 2-step AA @ (190°C/0.5h, 50°C/1h (water quenching), 130°C/30h).....73

**Figure 4.23:** LOM Micrographs: a) 24-D-8\*: 3-step ST (515°C/3h,530°C/8h, 535°C/4h, water quenching (66°C)), 24h NA, 2-step AA @ (190°C/4h, 50°C/1h (water quenching), 130°C/20h) b) 24-E-8\*: 3-step ST (515°C/3h,530°C/8h, 535°C/4h, water quenching (66°C)), 24h NA, 2-step AA @ (190°C/4h, 50°C/1h (water quenching), 130°C/30h) c) 0-F-8\*: 3-step ST (515°C/3h, 530°C/8h, 535°C/4h, water quenching (66°C)), 1-step AA @ (175°C/12h) d) 24-F-8\*: 3-step ST (515°C/3h,530°C/8h, 535°C/4h, water quenching (66°C)), 24h NA, 1-step AA @ (175°C/12h).....74

**Figure 4.24:** Corrosion depths for the machined samples heat treated using ST (2-step & 3-step), NA (0 & 24 hrs) and AA (1-step & 2-step) conditions.....75

**Figure 4.25:** Comparison of the average UTS and YS for 3-step ST, NA (0 & 24 hrs), two step AA conditions and 2-step ST, NA (72 hrs), one step AA conditions.....77

**Figure 4.26:** Average Yield Strength (YS) (MPa) vs. (NA & AA) Total Aging Time (hrs) for one and two step AA.....78

**Figure 4.27:** Average Elongation vs. (NA & AA) Total Aging Time, hrs for one and two step AA.....79

**Figure 4.28:** Average UTS and maximum corrosion depths for third series heat treatments.....80

<b>Figure 4.29:</b> Average YS and maximum corrosion depths for third series heat treatments.....	81
<b>Figure 4.30:</b> Average elongation and the maximum corrosion depths for third series heat treatments.....	82
<b>Figure 4.31:</b> a) SEM Micrograph of fractured sample 24-C-8, (250 X).....	83
<b>Figure 4.32:</b> b) SEM Micrograph of fractured sample 24-C-8, (500 X).....	83
<b>Figure 4.33:</b> c) SEM Micrograph of fractured sample 24-C-8, (1000 X).....	84
<b>Figure 4.34:</b> d) SEM Micrograph of fractured sample 24-C-8, (2000 X).....	84
<b>Figure 4.35:</b> SEM Micrograph of fractured sample 0-B-8, (250 X).....	85
<b>Figure 4.36:</b> SEM Micrograph of fractured sample 0-B-8, (500 X).....	85
<b>Figure 4.37:</b> SEM Micrograph of fractured sample 0-B-8, (1000 X).....	86
<b>Figure 4.38:</b> SEM Micrograph of fractured sample 0-D-8, (250 X).....	87
<b>Figure 4.39:</b> SEM Micrograph of fractured sample 0-D-8, (500 X).....	87
<b>Figure 4.40:</b> SEM Micrograph of fractured sample 0-D-8, (1000 X).....	88
<b>Figure 4.41:</b> SEM Micrograph of fractured sample 0-D-8, (2000 X).....	88
<b>Figure 4.42:</b> Flow curves of 0-B series: 3-step ST (515°C/3h, 530°C/8, & 535°C/4h), 2-step AA @ (190°C/0.5h, 50°C/1h (water quenching), & 130°C/20h).....	90
<b>Figure 4.43:</b> Flow curves of 0-C series: 3-step ST (515°C/3h, 530°C/8, & 535°C/4h), 2-step AA @ (190°C/0.5h, 50°C/1h (water quenching), & 130°C/30h).....	90
<b>Figure 4.44:</b> Flow curves of 0-D series: 3-step ST (515°C/3h, 530°C/8, & 535°C/4h), 2-step AA @ (190°C/4h, 50°C/1h (water quenching), & 130°C/20h).....	91
<b>Figure 4.45:</b> Flow curves of 0-E series: 3-step ST (515°C/3h, 530°C/8, & 535°C/4h), 2-step AA @ (190°C/4h, 50°C/1h (water quenching), & 130°C/30h).....	92

<b>Figure 4.46:</b> Flow curves of 24-C series: 3-step ST (515°C/3h, 530°C/8h, & 535°C/4h), 24h NA, 2-step AA @ (190°C/0.5h, 50°C/1h (water quenching), & 130°C/30h).....	92
<b>Figure 4.47:</b> Flow curves of 24-D series: 3-step ST (515°C/3h, 530°C/8h, & 535°C/4h), 24h NA, 2-step AA @ (190°C/4h, 50°C/1h (water quenching), & 30°C/20h).....	93
<b>Figure 4.48:</b> Flow curves of 0-F series: 3-step ST (515°C/3h, 530°C/8h, & 535°C/4h), 1-step AA @ (175°C/12h).....	93
<b>Figure 4.49:</b> Flow curves of 24-F series: 3-step ST (515°C/3h, 530°C/8h, & 535°C/4h), 24h NA, 1-step AA @ (175°C/12h).....	94
<b>Figure 4.50:</b> A quality index chart and tensile data for the B206 alloy.....	95
<b>Figure 4.51:</b> Potentiodynamic polarization curves for heat treated B206 alloy.....	98
<b>Figure 4.52:</b> SEM micrographs of specimens following potentiodynamic corrosion testing 24-F-8: 3-step ST (515°C/3h, 530°C/8h, 535°C/4h, water quenching 66°C), 24h NA, 1-step AA @ (175°C/12h): (a) 75X and (b) 500X. 0-F-8: 3-step ST (515°C/3h, 530°C/8h, 535°C/4h, water quenching 66°C), 1-step AA @ (175°C/12h): (c) 75X and (d) 500X.....	99
<b>Figure 4.53:</b> SEM micrographs of specimens following potentiodynamic corrosion testing 0-C-8: 3-step ST (515°C/3h, 530°C/8h, 535°C/4h, water quenching 66°C), 2-step AA @ (190°C/0.5h, 50°C/1h (water quenching), 130°C/30h): (e) 75X and (f) 500X. 0-D-8: 3-step ST (515°C/3h, 530°C/8h, 535°C/4h, water quenching 66°C), 2-step AA @ (190°C/4h, 50°C/1h (water quenching), 130°C/20h):(g) 75X and (h) 500X.....	100
<b>Figure 4.54:</b> SEM & Optical Metallography images: (a), (c), (e) 0-C-8 (shorter first step AA time (0.5 hr) at 190°C and the second stage at 130°C for 30 hrs without NA). (b), (d), (f) 0-D-8 (longer first step AA time (4 hrs) at 190°C and the second stage at 130°C for 20 hrs without NA).....	103
<b>Figure 4.55:</b> Dry wear track for test samples: a) 24-F-8: 3-step ST (515°C/3h, 530°C/8h, 535°C/4h, water quenching 66°C), 24h NA, 1-step AA @ (175°C/12h). b) 0-	

C-8: 3-step ST (515°C/3h, 530°C/8h, 535°C/4h, water quenching 66°C), 2-step AA @ (190°C/0.5h, 50°C/1h (water quenching), 130°C/30h). c) 0-D-8: 3-step ST (515°C/3h, 530°C/8h, 535°C/4h, water quenching 66°C), 2-step AA @ (190°C/4h, 50°C/1h (water quenching), 130°C/20h).....104

**Figure 4.56:** Wear track measured when the samples were exposed to a corrosive medium a) 24-F-8: 3-step ST (515°C/3h, 530°C/8h, 535°C/4h, water quenching 66°C), 24h NA, 1-step AA @ (175°C/12h). b) 0-C-8: 3-step ST (515°C/3h, 530°C/8h, 535°C/4h, water quenching 66°C), 2-step AA @ (190°C/0.5h, 50°C/1h (water quenching), 130°C/30h). c) 0-D-8: 3-step ST (515°C/3h, 530°C/8h, 535°C/4h, water quenching 66°C), 2-step AA @ (190°C/4h, 50°C/1h (water quenching), 130°C/20h).....106

**Figure 4.57:** OCP varying with time during and after the tribocorrosion experiments...108

## **List of Abbreviations**

**AA –Artificial Aging**

**BSE – Back-Scattered Electrons**

**DSC –Differential Scanning Calorimetry**

**EDS – Energy Dispersive Spectroscopy**

**GP- Guinier-Preston ( $\text{Al}_2\text{Cu}$ )**

**GPB- Guinier-Preston-Bagariastkij ( $\text{Al}_2\text{CuMg}$ )**

**LOM – Light Optical Microscope**

**NA – Natural Aging**

**OCP – Open Circuit Potential**

**OM – Optical Metallography**

**SEM – Scanning Electron Microscope**

**ST- Solution Treatment**

**TEM – Transmission Electron Microscope**

**UMSA – Universal Metallurgical Simulator and Analyzer**

**UTS – Ultimate Tensile Strength, MPa**

**YS – Yield Strength, MPa**

## **CHAPTER 1: INTRODUCTION**

### **1.1 General Background**

The AA 206 family of Al casting alloys (up to 5 wt% Cu) have mechanical properties approaching that of ductile iron, e.g. elongations up to 25%. Primarily limited to military and aerospace applications because of their tendency towards hot shortness, these alloys are also seeing increased interest as candidates for automotive suspension applications. Grain refining has improved this alloy's castability by reducing its susceptibility to hot tearing [1].

B206 is a registered alloy that takes advantage of a discovery related to the grain refinement by Ti additions [2]. Currently, B206 alloy automotive applications are restricted due to its susceptibility to the intergranular stress corrosion which is detrimental to the cast component high cycle fatigue performance. Intergranular corrosion can be controlled by high temperature Artificial Aging and a long aging time (T7 temper designation). However, the overaged condition will lead to poorer mechanical properties of the alloy. Thus, a heat treatment that balances both the corrosion resistance and mechanical properties is the main concern for the B206 alloy.

Heat Treatment of the B206 alloy should be optimized for the homogeneous dissolution of the Al-Cu phases during Solution Treatment (ST) and a uniform distribution of Al-Cu precipitates during the Artificial Aging (AA) treatment.

In this study, the corrosion behaviour has been examined, principally using immersion testing and potentiodynamic testing, on samples that have been subjected to different heat treatment schedules involving a 2-step or 3-step solution treatment and different aging schedules (natural and artificial). The heat treatment schedules that produce the optimum mechanical properties [1] are not necessarily those that produce the most corrosion resistant materials [2]. If B206 is to be used in automotive applications such as suspension components, then high ductility (elongations >7%) is required for crashworthiness [2].

## **1.2 Objectives**

The main objective of this research work is to develop a heat treatment condition that gives both excellent corrosion resistance (no intergranular corrosion) and mechanical properties (270 MPa Yield Strength (YS), 310 MPa Ultimate Tensile Strength (UTS) and minimum 10% total elongation of B206 alloy). The detailed objectives are as follows:

- To perform immersion corrosion testing, potentiodynamic polarization testing and tribocorrosion analysis for the heat treated specimens.
- To characterize the as-cast and heat treated samples of AA 206 alloy for corrosion resistance and mechanical properties.
- To compare the results of heat treated samples subjected to 2-step vs. 3-step Solution Treatment (ST) and 1-step vs. 2-step Artificial Aging (AA) with and without Natural Aging (NA).



## CHAPTER 2: LITERATURE REVIEW

### 2.1 Introduction

The first aluminum casting alloy used in America was an Al-8% Cu alloy, known as No.12 alloy [3]. An Al-10% Cu alloy (No.122) was used for automotive pistons and cylinder heads. In 1909, Alfred Wilm discovered that an Al-4.5%Cu-0.5%Mn alloy would strengthen by aging after a quench from an elevated temperature. This alloy was called 'Duralumin', and formed the basis for the Al-Cu family of alloys used today [4]. The Al-Cu casting alloys have excellent mechanical properties, high temperature strength, and low cycle fatigue properties but they are difficult to cast, primarily because of hot cracking [5]. As years went by, foundrymen discovered that additions of other elements, especially Si, improved castability. Hence, the family of Al-Cu alloys has been largely supplanted by Al-Cu-Si and Al-Si-Mg alloys [5].

It has long been well known that grain refinement reduces the tendency for hot cracking in net-shaped castings [5]. The study which shows this most clearly is a 1970 paper by Davies [6], who found the total length of hot tears in a casting was proportional to the as-cast grain size. In the early 1930's, Ti was added to grain refine Al-Cu casting alloys [7]. The improvement in castability was considerable, and this quickly became the established practice [5]. Foundrymen found that the best (smallest) grain sizes occurred at concentrations above 0.15 wt% Ti [8], the solubility limit of the  $TiAl_3$  intermetallic in pure aluminum. This became the accepted practice, as shown by the chemical composition limits of the Aluminum Association for the 201,202,204 and 206 alloys: A minimum Ti content of 0.15% is specified [5]. A combination of grain refinement and thermal management of the mold temperature is necessary for the elimination of hot tears in A206.0 and A535.0 (Al-(6.2-7.5)Mg-(0.1-0.25)Mn-0.15max.Si-0.15max.Fe-0.05max.Cu-(0.1-0.25)Ti) alloys [9].

Aluminum-Copper alloys, such as the aluminum 206 alloy, offer both high strength and excellent ductility with the values approaching some grades of ductile iron and significantly higher than those of aluminum 356 alloys. The Aluminum-copper 206 alloy has a number of potential applications to reduce vehicle weight, including automotive suspension knuckles, vehicle control arms, differential carrier parts, aerospace and military castings [1, 10, 11].

Although high strength is achieved in aluminum alloys by the presence of Cu as an alloying element, copper is particularly deleterious to the corrosion behaviour of Al alloys owing to galvanic couples between the copper-rich intermetallic inclusions and the adjacent copper-depleted matrix [12].

## **2.2 Key Alloying and Impurity elements**

### **2.2.1 Copper**

Copper is the main alloying element in B206 casting alloys. It is one of the most important alloying elements for aluminum due to its relatively high solubility in aluminum and its strengthening effect. The alloy strengthening will be a maximum for copper additions between 4 and 6%, depending upon the influence of other elements. Copper, as a principal alloying element in aluminum, imparts substantial precipitation hardening characteristics and excellent elevated temperature properties to the alloy. Often copper is accompanied by magnesium in order to accelerate and increase age hardening at room temperature [13].

### **2.2.2 Manganese**

Manganese is a common impurity in primary aluminum. It can be present in many Al-Cu alloys in amounts up to 1% and can completely enter the (Al) solid solution after solidification. Often, manganese is added to Al-Cu alloys to mitigate the detrimental effects of impurities such as iron and silicon [14]. Manganese is also added to reduce the embrittling effect. It gets combined with iron and silicon and increases the strength in solid solution. Addition of manganese causes the precipitation of magnesium to be more general and allows for a low magnesium content [15]. The presence of Fe, Si and Ni may result in formation of Mn-bearing phases of eutectic origin. This results in a reduction of the manganese concentration in the aluminum matrix [16].

An addition of 0.25% manganese has no appreciable influence upon aging of binary aluminum-copper alloys, but 0.5-1.0% manganese distinctly reduces the extent of aging. In the alloys containing 0.5-1.0% manganese, the undissolved constituent contains copper as well as manganese. Its presence would reduce the amount of copper

remaining in solid solution. This is the reason for the decreased precipitation-hardening obtained at room temperature with these alloys [17].

### **2.2.3 Magnesium**

Magnesium is added to enhance the response of aluminum-copper alloys to heat treatment. Magnesium additions to aluminum-copper alloys increase the strength after solution treatment and quenching. With increasing magnesium content, the sub-grain size is increased and the dislocation density is decreased [18]. Magnesium forms the  $\text{Al}_2\text{CuMg}$  phase, which in the course of non-equilibrium solidification precipitates as part of the ternary eutectic  $(\text{Al}) + \text{Al}_2\text{Cu} + \text{Al}_2\text{CuMg}$  at  $505\text{-}507^\circ\text{C}$ , and makes the solidification range much broader [16].

### **2.2.4 Silicon**

Silicon, after iron, is the highest impurity level in electrolytic commercial aluminum (0.01 to 0.15%) [15]. Silicon is added to Al-Cu alloys to increase the fluidity in the casting and curtail hot shortness. Hence Al-Cu alloys have been steadily replaced by Al-Cu-Si alloys. However, addition of silicon substantially reduces the ductility of the alloy. It does not form any phases with copper and possesses relatively high solubility in (Al). This improves the castability but Si is bad for alloy thermal stability [16]. The presence of 0.25% silicon in a binary aluminum-copper alloy had no effect on the aging characteristics [17].

### **2.2.5 Iron**

Iron forms phases with manganese, nickel and copper. It is the principal impurity in Al-Cu-Si alloys. An increase in iron content affects the mechanical properties, especially ductility (elongation) fracture toughness, and possibly, other properties. Castability is less sensitive to the presence of this element [16]. For an Al-Cu binary alloy, the amount of age-hardening at room temperature decreased proportionately with the amount of iron present, and the aging was completely eliminated with iron additions of up to 1.5% [17].

### **2.2.6 Tin**

Trace element or micro alloying additions of Sn are well known to increase the hardening response of Al-Cu alloys during elevated temperature (130°C and 190°C) aging. Ternary additions of Sn results in an extremely fine and uniform dispersion of  $\theta'$  precipitates, which effectively strengthen the Al-1.7%Cu alloy [19].

### **2.2.7 Titanium**

Titanium is added as a grain refiner and it is very effective in reducing the grain size [20]. It also produces a better dispersion of insoluble constituents, porosity and non-metallic inclusions, resulting in a significant improvement in the mechanical properties of the material [18]. Since grain size controls the distribution [21] of the porosity and the constituents, the mechanical properties of these alloys are very sensitive to grain size. With the addition of AlTi5B1, a modification of the solidification structure and a smaller solidification grain size are obtained [18].

### **2.2.8 Nickel**

Nickel with copper forms  $Al_6Cu_3Ni$  or  $Al_3(Cu, Ni)_2$ . These compounds are thermally stable and can improve the mechanical properties at elevated temperatures. However, they reduce the copper concentration in aluminum [16].

## **2.3 History of casting Al-Cu alloys**

### **2.3.1 Al-Cu phase diagram**

In the binary aluminum-copper system, the aluminum-rich terminal solid solution is in equilibrium with the intermetallic phase  $\theta$   $Al_2Cu$ , since some solid solubility exists [18]. The eutectic phases that separate from the liquid in the solidification reaction are  $CuAl_2$ , which is an intermetallic phase containing 53.5wt% Cu, and the aluminum solid solution, which contains 5.65wt% Cu [14].

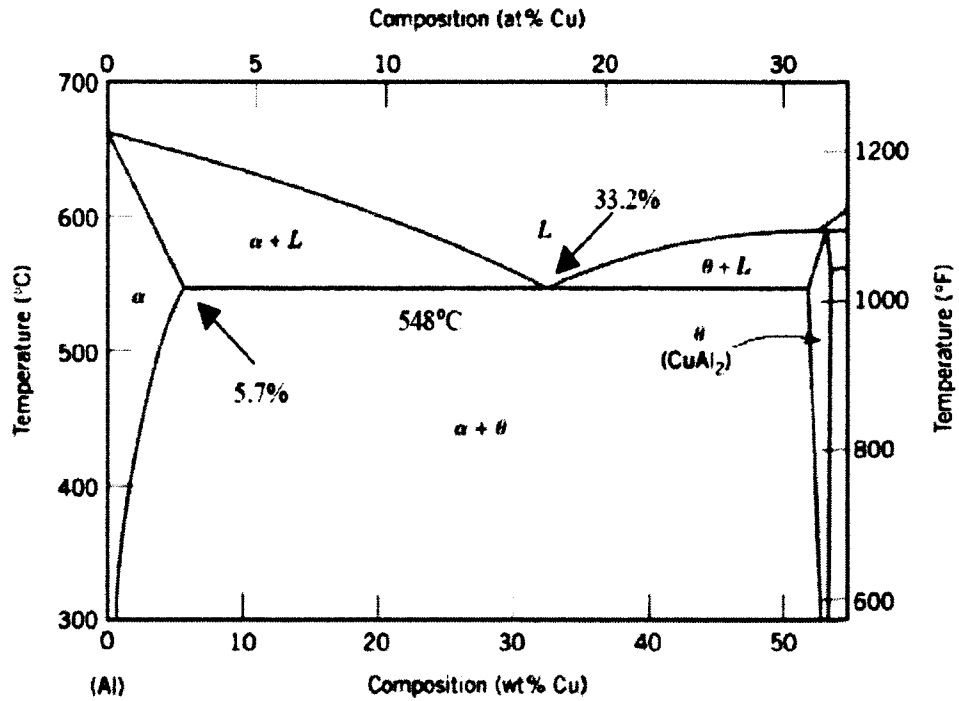


Figure 2.1: Aluminum rich portion of the Al-Cu phase diagram [14].

### 2.3.1.1 B206 Alloy

The B206 alloy has a copper content in the range of 4.5% - 5.5%. The composition of B206 alloy is given in Table 2.1:

Table 2.1: Registered B206.0 alloy composition [2].

Cu	Mg	Mn	Fe	Ti	Si	Zn	Others	Al
4.2-5.0	0.15-0.35	0.2-0.5	0.10	0.10	0.05	0.10	0.15	balance

### 2.3.1.2 Solidification reactions of B206 alloy

The solidification sequence of the B206 alloy is summarized in Table 2.2 [22].

**Table 2.2:** Formation of various phases during the solidification process in a B206 alloy [22].

Reactions	Temperature (°C)
Development of dendrite network	651-649
Liquid $\rightarrow$ (Al) + Al <sub>6</sub> (MnCuFe)	649
Liquid + Al <sub>6</sub> (MnCuFe) $\rightarrow$ (Al) + Al <sub>20</sub> Cu <sub>2</sub> Mn <sub>3</sub>	616
Liquid $\rightarrow$ (Al) + Al <sub>20</sub> Cu <sub>2</sub> Mn <sub>3</sub> + Al <sub>2</sub> Cu + Al <sub>7</sub> Cu <sub>2</sub> Fe	537
Liquid $\rightarrow$ (Al) + Al <sub>2</sub> Cu + Al <sub>2</sub> CuMg + Mg <sub>2</sub> Si	512

A network of coherent dendrites forms at about 10-15°C below the liquidus temperature and at about 0.30-0.35 fraction solid during the solidification. The remaining fraction liquid (0.65-0.70) has to solidify in the interdendritic region over 170-180°C. Therefore, B206 alloy castings are very susceptible to hot tearing [14, 22].

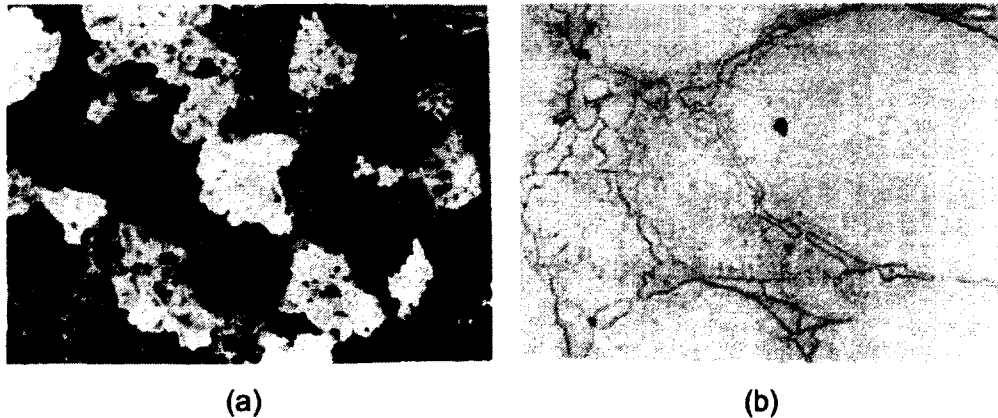


Figure 2.2: Microstructure of B206 alloys (a) grains (b) interconnected dendrites [14].

## 2.4 Casting Technology

### 2.4.1 Permanent Mold Casting Process

Permanent mold refers to the tooling used to produce aluminum castings. The molds or dies are usually made of high alloy iron or steel (both very dense). The cavity surfaces of the mold are coated with a thin layer of heat resistant material such as clay or sodium sulfate. The metal molds that consist of two or more parts are then assembled. The molds are preheated to a set temperature and through the use of water-cooling and other radiation techniques a very close thermal balance is maintained. The molten metal

is then poured into a sprue at the top of the mold. The metal flows into the mold cavity through the runner system by the pressure and velocity induced by gravity. When the metal has solidified, the mold is opened and the casting is removed [23].

The advantages of permanent mold casting process, compared to sand casting processes are better surface finish, precise and consistent dimensional control and improved mechanical properties. Significant energy savings can be achieved by using gravity and/or low-pressure permanent-mold casting processes, with sand or permanent-mold cores. Energy savings of about 250kWh per ton of castings are possible by switching from sand to permanent mold [24].

## 2.4.2 Hot cracking of Al-Cu-Mn-Mg alloy

### 2.4.2.1 Effect of Silicon on the fluidity and hot cracking of Aluminum-Copper alloy

Weijing et al [25] reported that the addition of Si can improve the fluidity and the hot cracking tendency of Al-5.0Cu-0.4Mn-0.3Mg alloy. Fluidity can be measured by the length of the spiral mold obtained. The fluidity property of the alloy rises in the beginning and then decreases with an increase of Si content from 1 to 2%. As can be seen from Figure 2.3 (a), its fluidity property increases again after the addition of 2% Si content. The fluidity was tested by spiral mold test, and the hot cracking was tested using hot crack ring mold [25]. The hot cracking tendency decreases sharply with the increase of Si content: see Figure 2.3 (b).

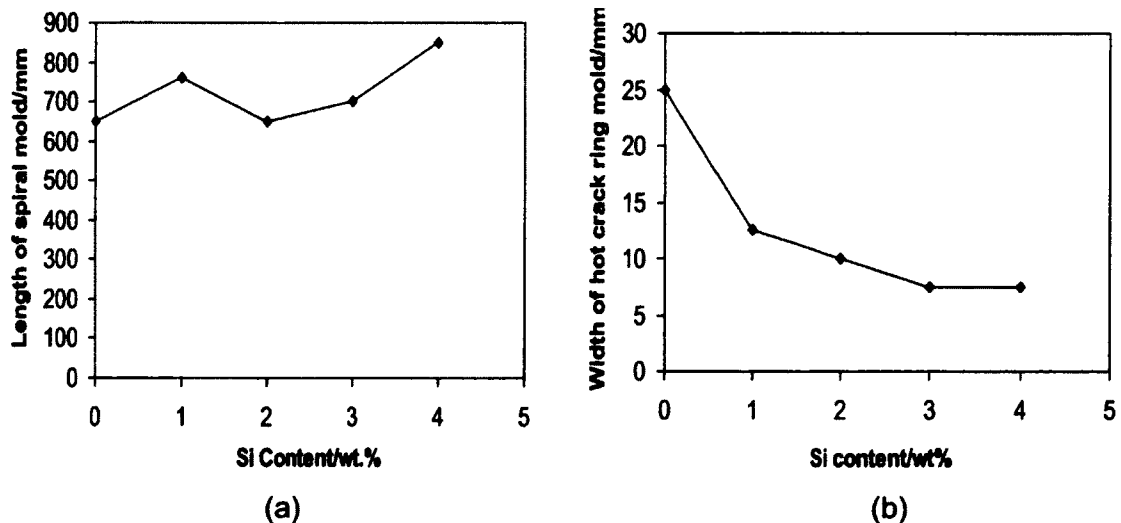


Figure 2.3: a) Variation of fluidity with different contents of Si. b) Variation of hot cracking tendency with different contents of Si [25].

#### **2.4.2.2 Fatigue crack growth in cast Al-Cu alloy A206 with different levels of porosity**

Porosity is one of the important casting defects that have a direct impact on the mechanical properties of the casting. Cast alloys frequently contain macro and microscopic pores resulting from either interdendritic shrinkage (which are usually irregular in shape) or from entrapped hydrogen and other gases (which tend to have a nearly spherical shape) [26]. The A206 alloy is the highest purity version of the 206 series alloys. It is commonly used in aerospace applications. A206 has also been used in automotive suspension components such as knuckles [2]. Rading et al [27] studied the effect of porosity on the fatigue crack growth for two different casting conditions (casting with chill and without a chill) of the A206 alloy. The study covered both near threshold and mid range regimes. No systematic relationship between casting conditions (chilled or non chilled) and the average level of porosity was observed [27]. They also found that the fatigue crack growth rate increases with increasing levels of porosity, especially close to the threshold regime. Hot isostatic pressing (HIP) process reduces the porosity level from 4% to less than 0.4%. However, its effect on fatigue crack growth rate is limited to the near threshold regime [27].

#### **2.5 Heat Treatment of Al-Cu alloys**

Heat Treatment is generally carried out to obtain an optimum combination of ductility, strength and corrosion resistance of aluminum casting alloys. In its broadest meaning, heat treatment comprises all thermal practices intended to modify the metallurgical structure of casting in such a way that physical and mechanical characteristics are controllably altered to meet specific engineering criteria. The steps involved in the heat treatment of Al-Cu alloys are:

- Solution Treatment (ST),
- Quenching and
- Natural/Artificial Aging.



### **2.5.1 Solution Treatment**

Solution treatment is designed to maximize the solubility of elements that participate in any subsequent aging treatment. It is most effective near the solidus and eutectic temperature where maximum solubility exists. However, incipient melting of low temperature eutectics must be avoided. The maximum temperature should be above the solvus temperature [28]. Solution Treatment (ST) at low temperatures will not dissolve the copper-rich intermetallic components in the aluminum matrix [29].

Cu and Mg are taken into solid solution during Solution Treatment (ST), and the structure becomes homogeneous. Quenching (rapid cooling) performed at the end of the solution treatment traps the copper dissolved in the aluminum yielding the desired super-saturated solid solution.

It has been reported that the  $\text{Al}_2\text{Cu}$  phase can contribute to the solid solution strengthening and second phase strengthening of Al-Cu alloys [30]. In casting alloys containing 5%Cu, the concentration of manganese in the super-saturated solid solution during solidification can reach 2%. Formation of the nonequilibrium (Al) +  $\text{CuAl}_2$  eutectics and a supersaturated solution of Mn in (Al) causes deviation from equilibrium during solidification [31]. Precipitation of manganese will occur only when copper in the solid solution reaches the required concentration [32].

### **2.5.2 Precipitation hardening**

Precipitation hardening can occur if the second phase is soluble at higher temperature but exhibits decreasing solid solubility with decreasing temperature. The mechanism of strengthening by age hardening after solution treatment involves the formation of coherent clusters of solute atoms [33]. The formation of a coherent precipitate in a precipitation-hardening system, such as Al-Cu, occurs in a number of steps. The Al-Cu alloy contains regions of solute segregation, or clustering after quenching from a solid solution. Guinier and Preston first detected this local clustering and named it the GP zone. With additional aging, large clumps of copper atoms on the {100} planes of the matrix were formed. This structure is GP2 or  $\theta''$ . Next, definite platelets of  $\text{CuAl}_2$  or  $\theta'$  form on the {100} planes of the matrix. With still further aging, the equilibrium phase

$\text{CuAl}_2$  or  $\theta$  is formed. High proportions of  $\theta$  precipitates formed by increasing the time and temperature soften the alloy and is said to be over-aged [34].

### **2.5.3 Natural Aging (NA)**

Natural aging is a spontaneous precipitation process that occurs at room temperature for days and weeks after Solution Treatment (ST). The excess solute in supersaturated  $\alpha$ -aluminum will precipitate slowly at room temperature. Solute atoms either cluster or segregate to selected atomic lattice planes, depending on the alloy systems, to form the GP zones, which are more resistant to movement of dislocations through the lattice and hence are stronger [33].

Abis et al [35] observed the early stages of transformation of a metastable  $\text{Al4.4Cu1.7Mg}$  alloy during Natural Aging (NA). The alloy has been homogenized at  $500^\circ\text{C}$  for 10 h and cold rolled down to 1.5mm thickness. It is then solution treated at  $520^\circ\text{C}$  for 1 h and water quenched at room temperature. DSC investigations, TEM observations, and the corresponding initial hardening increase suggest the formation of Guinier-Preston-Bagariastkij- $\text{Al}_2\text{CuMg}$  (GPB) + Guinier-Preston- $\text{Al}_2\text{Cu}$  (GP) zones [35].

### **2.5.4 Artificial Aging (AA)**

Artificial aging is a process of heating the castings in the as-quenched condition to intermediate temperatures. It produces the transitional (metastable) forms of the equilibrium precipitate of a particular alloy system. These transitional precipitates remain coherent with the solid solution matrix and thus contribute to precipitation strengthening [33]. Ductility is greatly affected by the artificial aging. Ductility will be high in the as-quenched condition and decreases during elevated temperature hardening.

#### **2.5.4.1 Single stage Artificial Aging (AA)**

A single step AA is the hardening process at a particular temperature. It is often thought that once an aluminum alloy is artificially aged at an intermediate temperature (eg. T6 temper at  $190^\circ\text{C}$ ), the microstructure and mechanical properties remain unchanged for an indefinite period at lower temperature [36]. However, recent observations made on an Al-Cu-Mg alloy with a much lower solute content have indicated that vacancies may remain mobile at room temperature after these alloys were first aged at  $180^\circ\text{C}$  [37]. Such

mobility will facilitate solute diffusion leading to possible further (secondary) precipitation at room temperature [38].

Meissner [39] studied the effect of natural + artificial aging on the duralumin (4.2%Cu, 0.5%Mg, 0.25%Mn, 0.3%Fe, and 0.3% Si). Artificial aging temperature ranged from 50°C to 200°C and the Artificial Aging (AA) time was 20 hrs and 40 hrs.

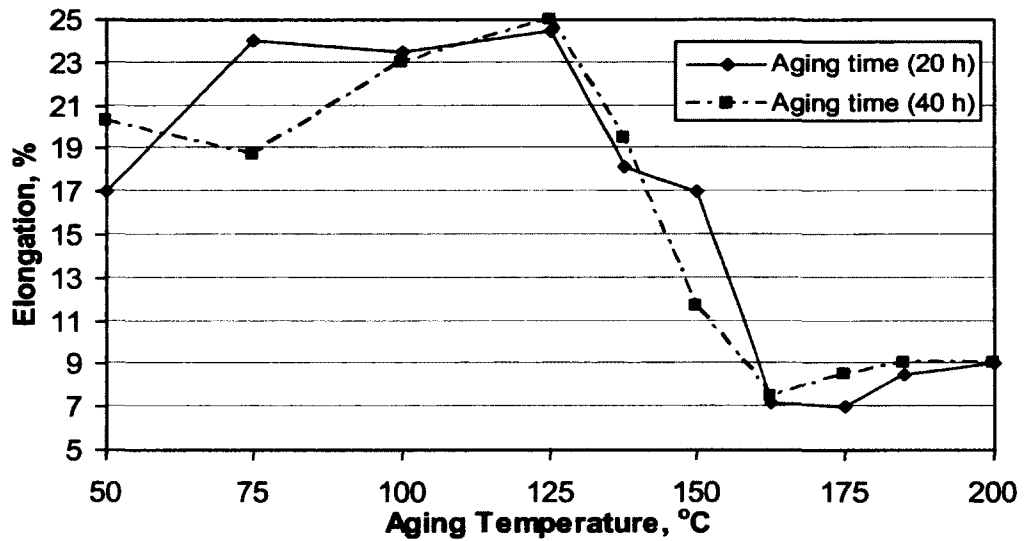


Figure 2.4: Effect of artificial aging on elongation for duralumin (artificial aging was applied immediately after quenching from about 510°C [39]).

The characteristics shown in Figures 2.4 and 2.5, which plot elongation vs. aging temperature, are almost the same. This clearly indicates that natural aging has no effect on the duralumin. The treatment of cold-rolling gives a high yield-point, combined with high tensile strength and high elongation (refer Fig. 2.6).

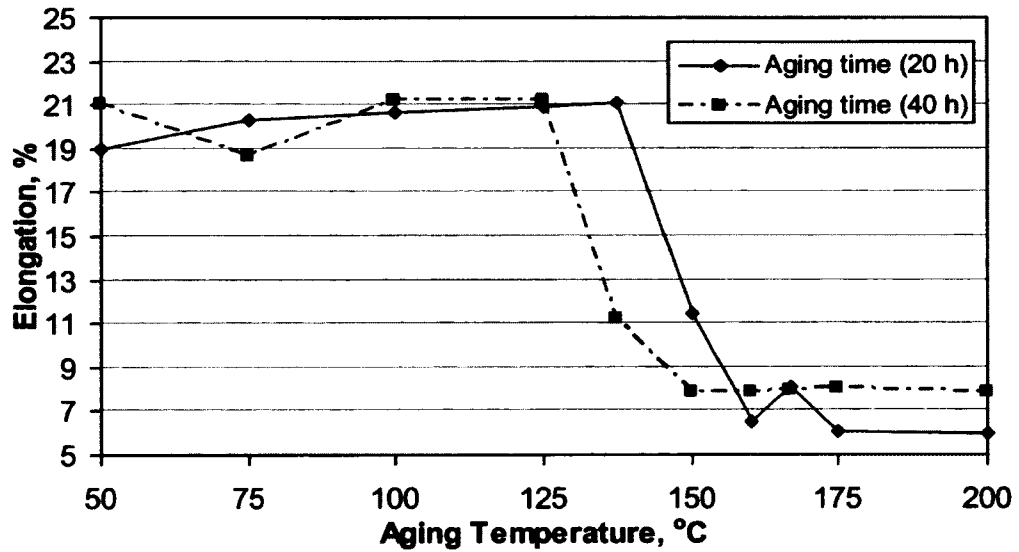


Figure 2.5: Effect of artificial aging on elongation for duralumin (artificial aging was applied after complete age-hardening at room temperature for 5 days [39]).

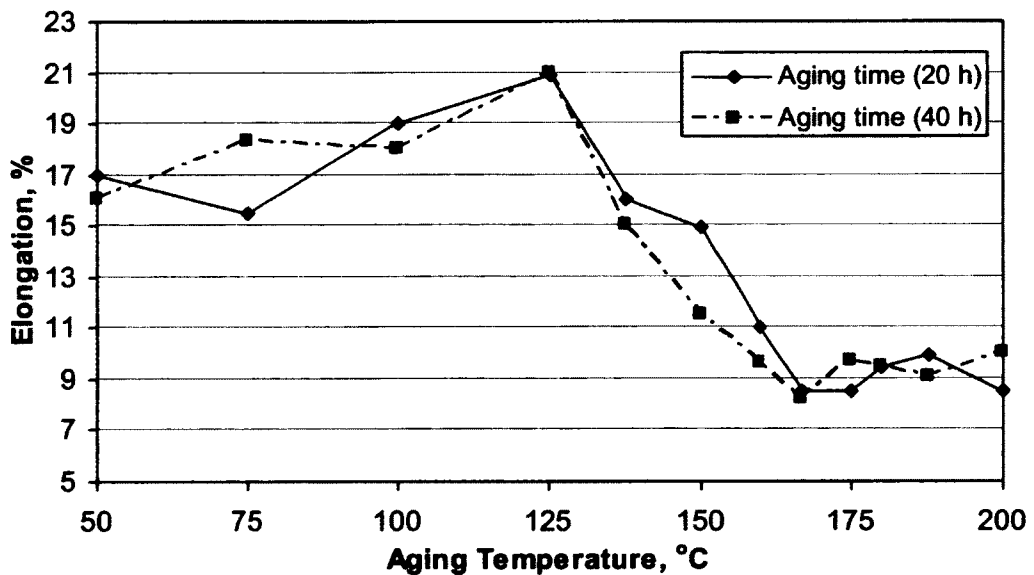


Figure 2.6: Effect of artificial aging on elongation for duralumin (artificial aging was applied after age-hardening at room temperature and cold-rolled [39]).

#### 2.5.4.2 Multi-stage Artificial Aging

As noted by Lumley, Polmear and Morton [15], multistep aging treatments are often used to improve the properties of aluminum alloys. A well known example is the T73 temper in which Artificial Aging at 100°C is followed by a second treatment at a higher temperature

(160°C). Another duplex treatment is to naturally age at room temperature after quenching and before artificial aging.

More recently, another form of multi-stage aging treatments, namely interrupted aging treatment (designated T6I6), has been reported and is claimed to be very effective in further improvement in the strength achievable via a standard T6 treatment. The T6I6 treatment is a heat treatment that involves interrupting a T6 treatment by quenching the alloy, followed by aging at lower temperature (25-65 °C) for a given period of time before the T6 treatment is resumed until peak hardness is obtained [40].

Goh et al [41] studied the effects of multi-step aging treatments on age-hardening response of aluminum alloys. They reported that multi-step aging treatments have little effect in AA6111, Al-4.0Cu-0.8Mg, and Al-4.0Cu-0.8Mg-0.8Si alloys despite a refinement in precipitate distribution.

Gao et al [36] reported on a 3-stage T6I6 interrupted aging treatment (see Figure 2.7). Interrupted aging results in nucleation of finely dispersed precipitates in the final aged microstructure [42, 43]. Alloys subjected to the T6I6 treatment have improved tensile strength, hardness and fracture toughness ranging from 5-30%, depending on the composition and specific processing conditions [38, 42].

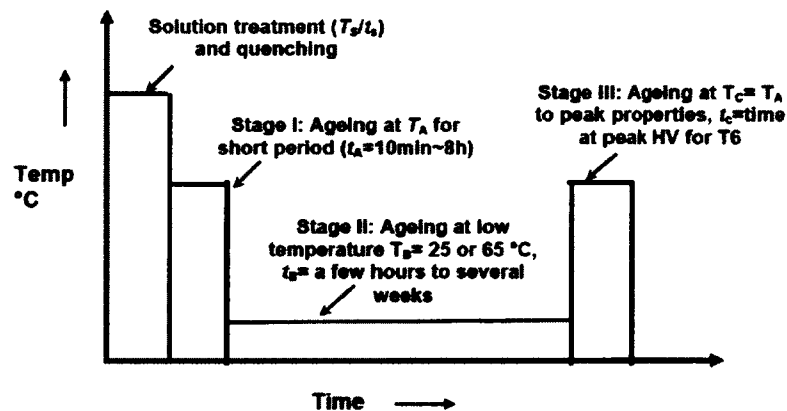


Figure 2.7 Schematic representation of the three stages of T6I6 interrupted aging treatment. The selection of a long initial Stage I and a suitable Stage II aging time is important. In the most cases, the Stage II aging at 25°C shows a more beneficial effect than aging at 65°C [36].

### 2.5.5 Effect of Si on the microstructure and mechanical properties of Al-4.5%Cu alloys

Han et al [30] reported on the effects of a Si addition on Al-4.5%Cu cast alloys. They used four alloys namely: Al-4.5%Cu, Al-4.5%Cu-1%Si, Al-4.5%Cu-2%Si and Al-4.5%Cu-3%Si (wt%). The coarse plate-like Si phases were distributed at the grain boundaries of the as-cast alloys: Fig. 2.8. The influence of Si on the mechanical properties of alloys depends on its morphology and distribution.

In the as-cast condition, the elongation decreases with an increase in Si content (refer to Table 2.3). After T4 heat treatment, Al-4.5%Cu-2%Si alloy possess the optimum mechanical property (refer to Table 2.4). This is due to the transformation of plate-like Si into spherical particles. Fine spherical Si particles are precipitated after quenching of Al-4.5%Cu-2%Si alloy [30].

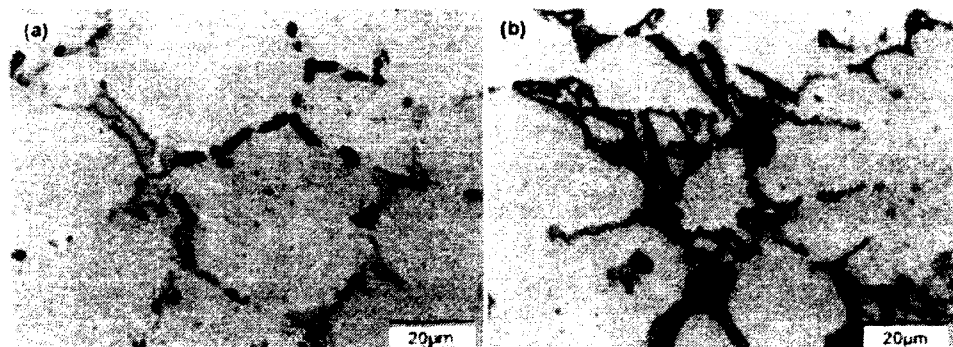


Figure 2.8: Microstructure of the as-cast alloys: (a) Al-4.5%Cu-1%Si (b) Al-4.5%Cu-2%Si [30].

Table 2.3: Mechanical properties of as-cast Al-4.5%Cu alloys with Si addition [30].

Alloy	Tensile Strength, MPa	Elongation, %	Hardness, HB
Al-4.5%Cu	187	10.6	51.8
Al-4.5%Cu-1%Si	181	7.2	54.8
Al-4.5%Cu-2%Si	179	6.4	57.1
Al-4.5%Cu-3%Si	184	6.0	58.4

**Table 2.4:** Mechanical properties of the alloys (as in Table 2.3) after T4 heat treatment [30].

<b>Alloy</b>	<b>Tensile Strength, MPa</b>	<b>Elongation, %</b>	<b>Hardness, HB</b>
Al-4.5%Cu	244	11.8	64.9
Al-4.5%Cu-1%Si	232	7.8	60.8
Al-4.5%Cu-2%Si	313	11.6	78.4
Al-4.5%Cu-3%Si	232	5.6	70.2

### 2.5.6 Effect of Cu and Si on mechanical properties in Al-Cu-Si-Mg alloys

Zeren [44] studied the effect of Cu and Si on Al-Cu-Si-Mg alloys with 1, 3, 4.5, 6 wt.% copper and 0, 5, 7, 12, 18 wt.% silicon. Mg varied in the range of 0.90 – 1.06 wt. %. Alloys were solution treated at 490°C for 4h, quenched in water and then aged at 180°C for 5, 10, 15, 20 h.

**Table 2.5:** Effect of Cu content of Al-Cu-Si-Mg alloys on mechanical properties [44].

<b>Alloy</b>	<b>Tensile Strength (MPa)</b>	<b>Hardness (HB)</b>	<b>Elongation (%)</b>
Alloy 1 (1% Cu)	152	45	12.7
Alloy 2 (3% Cu)	290	85	7.5
Alloy 3 (4.5% Cu)	360	105	5.4
Alloy 4 (6% Cu)	402	118	2.5

**Table 2.6:** Effect of Si content of Al-Cu-Si-Mg alloys on mechanical properties [44].

<b>Alloy</b>	<b>Tensile Strength (MPa)</b>	<b>Hardness (HB)</b>	<b>Elongation (%)</b>
Alloy 1 (0.5% Si)	152	45	12.7
Alloy 2 (7% Si)	164	65	7.2
Alloy 3 (12% Si)	180	90	3.0
Alloy 4 (18% Si)	200	102	1.1

An increase in Cu content results in an increase in tensile strength and hardness (due to precipitation hardening) accompanied by a decrease in elongation [44]. Similarly, by

increasing the Si content, hardness and tensile strength increases and elongation decreases. An optimum combination of Cu and Si content is necessary for good mechanical properties.

### **2.5.7 Chemistry/Property relationships in AA206 alloy**

Sigworth and Major [2] reported that the 206 alloys in the T4 temper will show sufficiently high ductility to exceed the >7% elongation requirement that is currently accepted as the standard for automotive suspension components. They also found that the sensitivity of Fe and Si impurities to mechanical properties is not high in the T4 temper. Achieving high ductility using 206 alloys in the T7 temper is a greater challenge. For that, they suggested low impurity levels and fast solidification rates to achieve >7% elongation in the T7 temper [2].

The T4 and T7 heat treatment cycles are listed below [2]:

T4: Ramp from room temperature to 480°C in 1 hour  
Continue ramping from 480°C to 495°C in ½ hour  
Hold at 495°C for 2 hours  
Ramp from 495°C to 528°C in ½ hour  
Hold 10 hours at 528°C  
Quench into 65°C water  
Wait 7 days before mechanical testing

T7: Solution treatment is same as outlined in above T4 schedule  
After the 65°C water quench hold 24 hrs at room temperature  
Age 4 hrs at 200°C  
Cool to room temperature in still air.

### **2.5.8 Mechanical properties of B206 alloy**

Sigworth and Major [2] reported on the tensile properties of the B206 alloy together with those for the more commonly used aluminum alloys (Fig. 2.9). The B206 alloy exhibits mechanical properties superior to conventional Al-Si-Mg and Al-Si-Cu alloys.



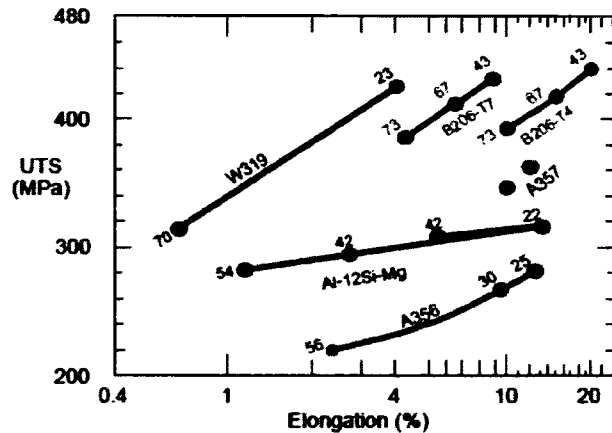


Figure 2.9: Range of mechanical properties in five aluminum casting alloys [2].

## 2.6 Corrosion of Al-Cu alloys

Al alloys in aqueous environments are prone to localized corrosion attack, because they generally contain significant amounts of constituent particles with different electrochemical activity compared to the matrix, and these particles readily form local galvanic cells on the metal surface [45].

Among the different forms of localized corrosion, intergranular corrosion is encountered most often in technologically important metallic materials like aluminum alloys that suffer severe degrees of various corrosion types in different environments [46, 47]. Pits and intergranular corrosion can be potential sites for initiation of cracks, resulting in catastrophic failure by stress corrosion cracking or corrosion fatigue. In principle, both pitting and intergranular corrosion result from a local breakdown of the passive film that forms on the surface, but the exact mechanism of the breakdown is still not clear. Attack that occurs at intermetallic particles or in the matrix of a grain is called pitting, whereas attack restricted to grain boundary regions is called intergranular corrosion. From an electrochemical point of view, both pitting and intergranular corrosion processes seem to be very similar in nature [48].

Corrosion studies of multiphase alloys are often complicated in nature [49]. The presence of the  $\theta$ -Al<sub>2</sub>Cu phase in the Al-Cu alloy made it difficult to understand its corrosion behaviour. The Al-Cu alloy is a multiphase alloy with an  $\alpha$ -Al matrix and  $\theta$ -Al<sub>2</sub>Cu precipitate. In the presence of a corrosive medium, the  $\alpha$ -Al matrix starts dissolving and the  $\theta$  phase (since it contains Cu) acts as a noble phase. Thus, a higher volume fraction of the  $\theta$ -Al<sub>2</sub>Cu phase in the alloy will result in higher (less active) corrosion potential according to the mixed potential theory [49].

Agarwala and Murty [49] performed a controlled potential corrosion test on the Al-4.5Cu alloy in 3.5% NaCl solution. It was reported that the preferential dissolution of the  $\alpha$ -matrix phase occurred in the anodic potential range of -0.300 to -0.500 V. However, as the applied polarizing potential was made more negative, a transition in corrosion characteristics occurred. Gradually,  $\alpha$ -matrix regions became immune and corrosion initiated along the  $\theta$ -Al<sub>2</sub>Cu phase. At a more cathodic potential of -0.900 V, accelerated corrosion of the  $\theta$  phase occurred, along with some dissolution of the copper-rich  $\alpha$ -matrix phase [49].

### 2.6.1 Immersion testing of heat treated 201 alloys in NaCl/H<sub>2</sub>O<sub>2</sub> corrosive solution

A heat treated 201 alloy containing copper (4.85%) and silver (0.72%) as major alloying elements is susceptible to stress corrosion cracking. Misra and Oswald [50] reported on its intergranular corrosion susceptibility as a function of microstructural condition, and related this behaviour to the precipitation kinetics during the aging process. They conducted intergranular tests on the solution treated and solution treated-aged specimens by immersing them in sodium chloride-hydrogen peroxide solutions for six hours. The severity of intergranular corrosion was measured in terms of the depth of corrosion penetration in the grain boundary region. For 201 alloys, intergranular attack increases with increase in artificial aging time (0 to 8 hrs), reaches a maximum at 8 hrs, and then decreases when overaged (refer to Fig.2.10).

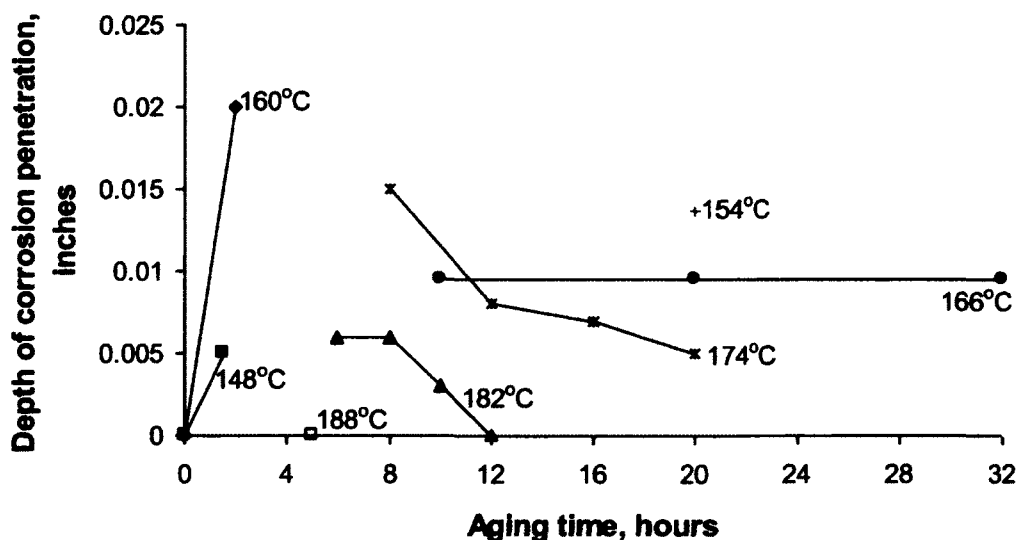


Figure 2.10: Intergranular corrosion characteristics of aged 201 alloy [50].

## **2.6.2 Stress corrosion cracking**

Aluminum and its alloys can fail by cracking along grain boundaries when simultaneously exposed to specific environments (water vapour, aqueous solutions, organic liquids and liquid metals) and stresses of sufficient magnitude. Stress-corrosion cracking in aluminum alloys is characteristically intergranular [51]. Intergranular (intercrystalline) corrosion is a selective attack of grain boundaries or closely adjacent regions without appreciable attack of the grains themselves. Intergranular corrosion is caused by potential differences between the grain-boundary region and the adjacent grain bodies [51].

### **2.6.2.1 Intergranular stress corrosion behaviour in Al-Cu-Mg-Ag alloys**

Al-Cu-Mg-Ag alloys can offer improved mechanical properties [52] but often exhibit susceptibility to localized corrosion and intergranular stress corrosion cracking [53, 54]. The presence of the grain boundary precipitates usually raises the susceptibility of these alloys to intergranular localized attack [55]. The copper content in solid solution in Al alloys directly correlates to the pitting potential of Al-Cu alloys [56]. Increasing the Cu content in the solid solution increases the pitting and repassivation potential associated with the matrix. The  $\text{Al}_2\text{CuMg}$  phase increases in size and density but its composition is unaltered upon over-aging. Thus, the presence of  $\text{Al}_2\text{CuMg}$  on grain boundaries cannot easily explain the susceptibility to intergranular stress corrosion cracking [57].

Little et al [57] reported on the improvement in resistance to intergranular stress corrosion cracking of the over-aged condition T8+ condition (i.e., T8 temper (peak aged) followed by an additional thermal exposure of 5000 h at 107.2°C) of two Al-Cu-Mg-Ag alloys (Al-5.0%Cu-0.8%Mg-0.5%Ag and Al-5.4%Cu-0.5%Mg-0.5%Ag). The 5000 h at 107.2°C thermal treatment was conducted to simulate the possible time of exposure to service conditions that could include elevated temperatures [57]. According to the Al-Cu phase diagram, the equilibrium solubility of Cu in an Al matrix is 5.65% at 548°C, less than 1% at 200°C and a little less than 0.1% at 107.2°C [58]. This T8+ condition results in eliminating the differential Cu concentration adjacent to the grain boundary compared to that of the grain interior. The resultant levelling of Cu concentration leads to the suppression of a preferential dissolution path at the grain boundaries associated with

intergranular stress corrosion cracking [57]. Figure 2.11 show the effect of aging on the copper depleted zones.

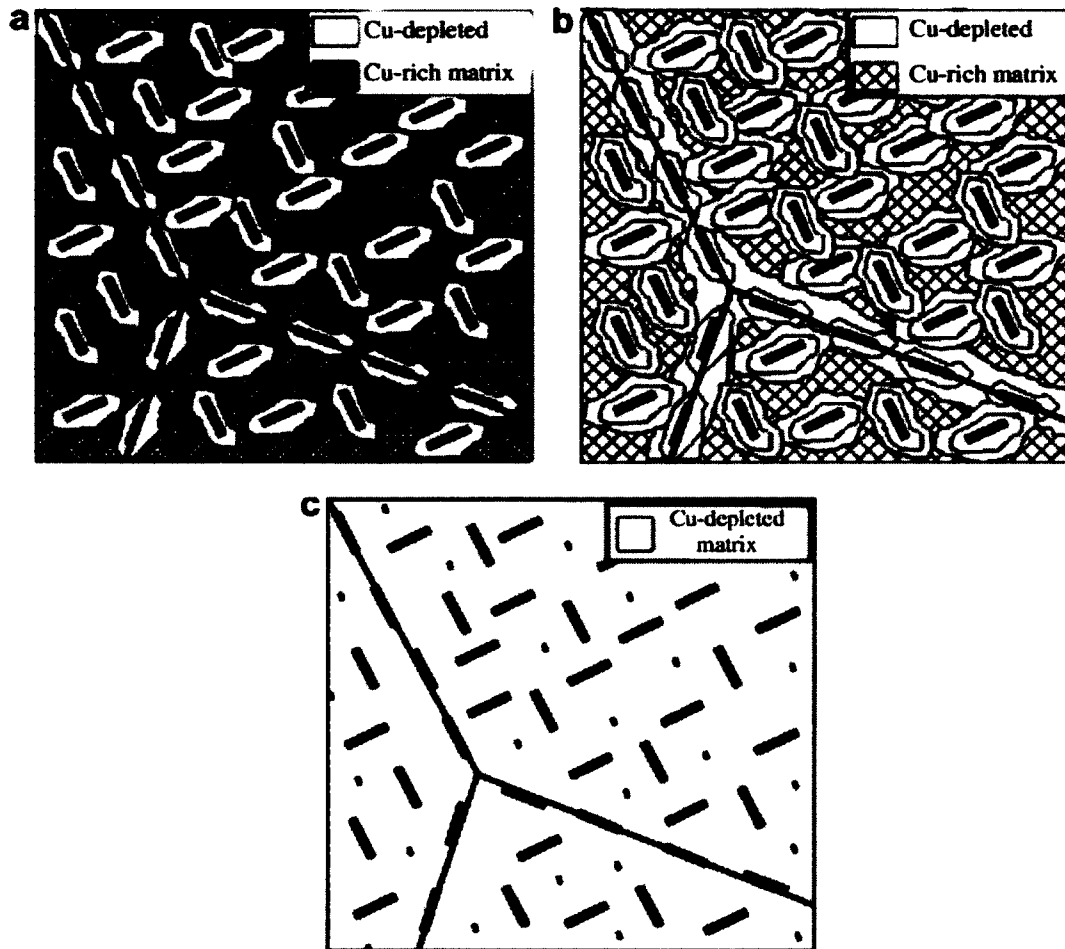


Figure 2.11: (a) Shows an under-aged condition where the boundary has the heaviest concentration difference between Cu-depleted zones and the supersaturated matrix (highest Cu in matrix). (b) Represents a peak-aged or over-aged condition where the Cu depletion zones around Cu-containing precipitates begin to overlap with each other not only at the boundaries but also in the matrix (c) Represents a schematic of the Cu-depleted matrix that would be associated with an extremely over-aged condition (lowest Cu in matrix). The preferential Cu depleted path along grain boundaries is eliminated. With the long aging times more nanoscale precipitates will form. Long aging times clearly shows a decrease in the amount of copper in solid solution possibly due to an increase in the number of nanoscale precipitates [57].

### 2.6.2.2 Pitting corrosion of Al-Cu alloys

Pitting is the most common corrosion attack on aluminum alloys. Pits form at localized discontinuities in the oxide film on aluminum exposed to atmosphere, fresh or salt water, or other neutral electrolytes[59]. The shape of the pits can vary from shallow, saucer-like depressions to cylindrical holes and the pit cavity is roughly hemispherical [59]. Aggressive anions, such as the halides, induce breakdown of the protective passive film and can result in catastrophic failure of the material. Intergranular corrosion can occur along with the pitting corrosion. The 2xxx series alloys are the least resistant to pitting corrosion. Reducing the aggressivity of the corrosive solution (for example, chloride ion concentration, oxidizing agents, temperature) can prevent the pitting attack [60].

Aluminum alloys containing a large proportion of copper are more susceptible to pitting corrosion than others [61]. Kim and Buchheit [62] examined high purity Al, Al-0.2Cu and Al-2.0Cu exposed to 0.1M NaCl solution. They determined that copper additions (up to 2.0wt. %) to aluminum decrease susceptibility to pit initiation provided that copper is retained in solid solution. This is observed as an increase in pitting potential with increase in copper content in an alloy [62].

Blanc et al [63] studied the susceptibility of pitting corrosion of pure aluminum and 2024 T351 alloy (containing 4.54 %Cu) in 0.1 mol/litre Na<sub>2</sub>SO<sub>4</sub> solutions containing chloride ions. Pure aluminum was used as a reference material. They found that the logarithm of the pit germination rate varied linearly with chloride concentration for both materials.

Foley [64] considered four steps to explain the role of Cl<sup>-</sup> anion. They are (a) adsorption of Cl<sup>-</sup>, (b) formation of intermediate complexes and soluble species, (c) thinning of the oxide film, and (d) direct attack of metal. Pits are formed when aggressive species such as chloride ions are in the electrolyte. In Figure 2.12, pit germination time  $t$  obeys an exponential law [64]:

$$-\ln(1-P) = \lambda t \quad 2.1$$

Where  $\lambda$  is the pit germination rate and  $P$  is the pitting probability.

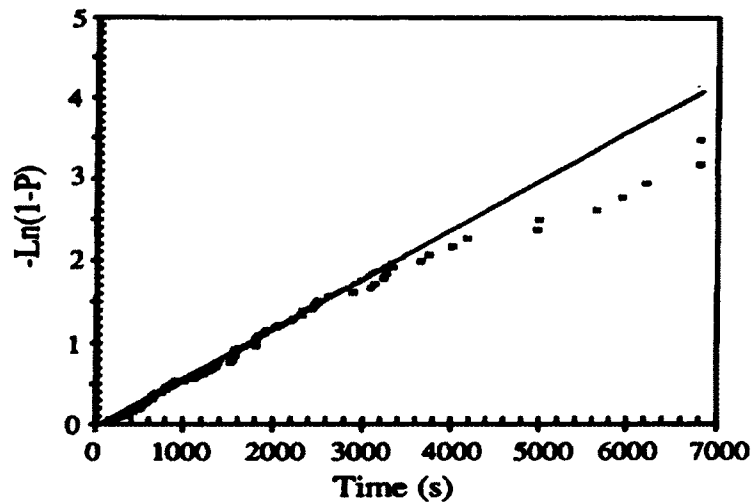


Figure 2.12: Pit germination time distribution (25mm thick plate of 2024 alloy,  $E = +300$  mV/SCE,  $0.0035 \text{ mol l}^{-1} \text{ Cl}^-$ ) [63].

The pit germination rate  $\lambda$  increased as the chloride ion concentration in the electrolyte increased (refer to Fig. 2.13). For concentrations of chloride ions equal to, or higher than,  $0.004 \text{ mol l}^{-1}$ , the logarithm of  $\lambda$  varies linearly with the logarithm of the chloride concentration [64].

$$\lambda = k [\text{Cl}^-]^n$$

2.2

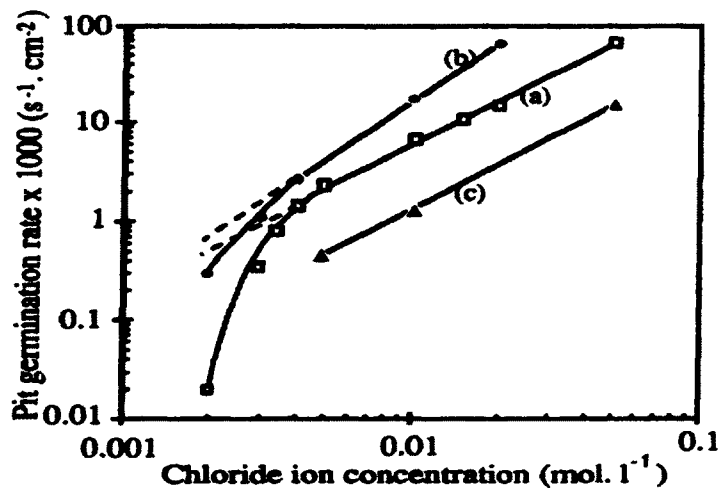


Figure 2.13: Variation of pit germination rate with the chloride ion concentration  $E=300$  mV/SCE; (a) 25 mm thick plate of 2024 alloy (b) 1.6 mm thick sheet of 2024 alloy (c) 99.99% Al [63].

Blanc et al [63] found that the precipitates enriched with Al, Cu and Mg dissolved during prepolarization in sodium sulphate and copper became redeposited on the passive film of 2024 alloy. This is the reason for high susceptibility to pitting corrosion.  $\text{Cl}^-$  ions are

aggressive towards precipitates enriched with copper and thus form pits. Copper also had an influence on the pit germination rate [63].

### 2.6.2.3 Copper redeposition during the dissolution in NaCl solution

The electrochemical effects of corrosion can be stronger in Al-Cu alloys than in alloys of many other types because of the large differences in electrode potential that can occur with variations in amount of copper in solid solution and because of the presence of non-uniformities in solid solution concentration [65]. Warraky et al [65] examined the enrichment of Cu and the type of attack occurring during the dissolution of Al-3.84%Cu alloy in 0.5M NaCl. They found that Cu clusters had concentrated around the edges of the specimens and two types of localized corrosion (intergranular and pitting) were evident, which were concentrated mainly around the Cu clusters and in the regions where a higher concentration of Cu is evident. In Figure 2.14, bright Cu-rich deposits are evident over the surface and were due both to the deposition of Cu from solution and to the dissolution of Al to produce a surface enriched with Cu [65].

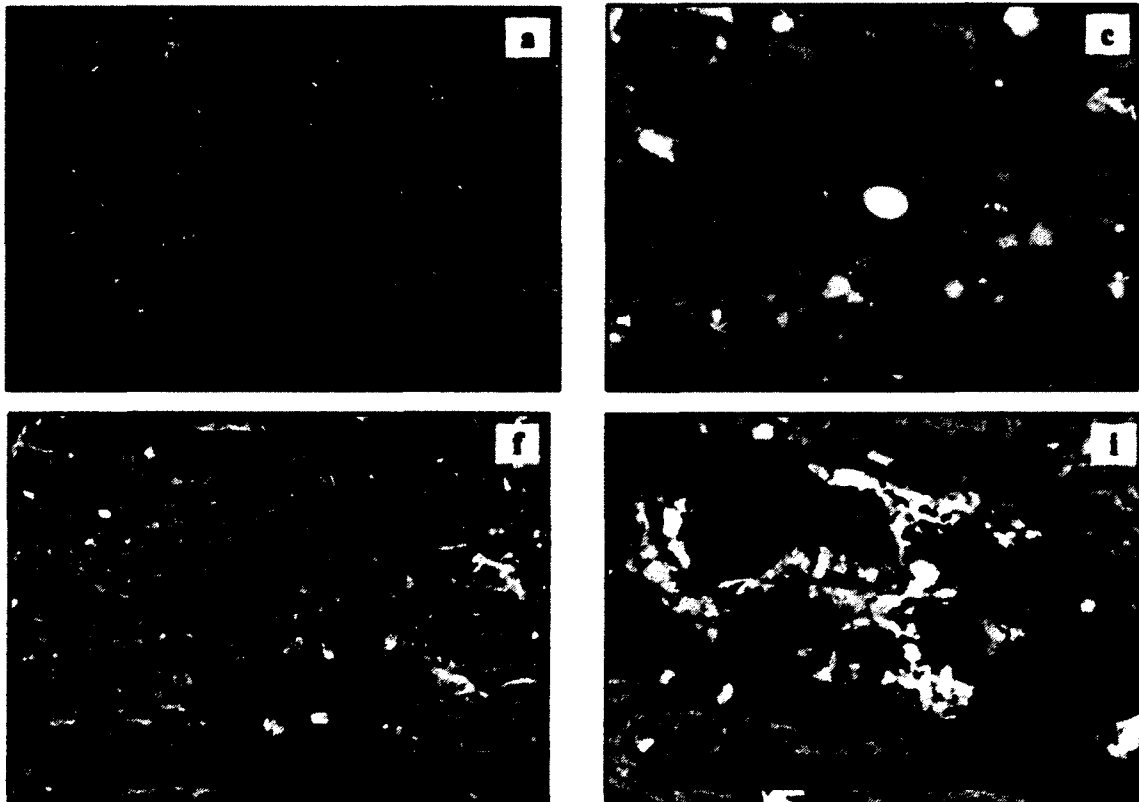


Figure 2.14: (a), (c), (f) & (i) Al-3.84%Cu alloy in 0.5 M NaCl for five days [65].

#### 2.6.2.4 Effect of quench delay time on corrosion behaviour of Al 2024 alloy

Campestrini et al [66] examined the effect of quench delay time on intermetallic particles and corrosion behaviour of Al 2024 (Al-4.4%Cu-1.5%Mg-0.6%Mn-0.5%Si-<0.5%Fe) alloy. They found that the increase in quench delay time forms complicated shell-shaped particles, with a difference in chemical composition between the core and the surface layer. These shell-shaped particles were the reason for localized corrosion of the Al 2024 alloy. Shorter quench delay time between 3 s and 27 s show general corrosion after immersion in NaCl for 24 h whereas longer quench delay time results in pitting attack. Quench delay times from 3 to 27 s result in a coarsening of the round shaped particles (Al-Cu-Mg precipitates). Figure 2.15 shows an increase in corrosion attack with increase in quench delay time [66].

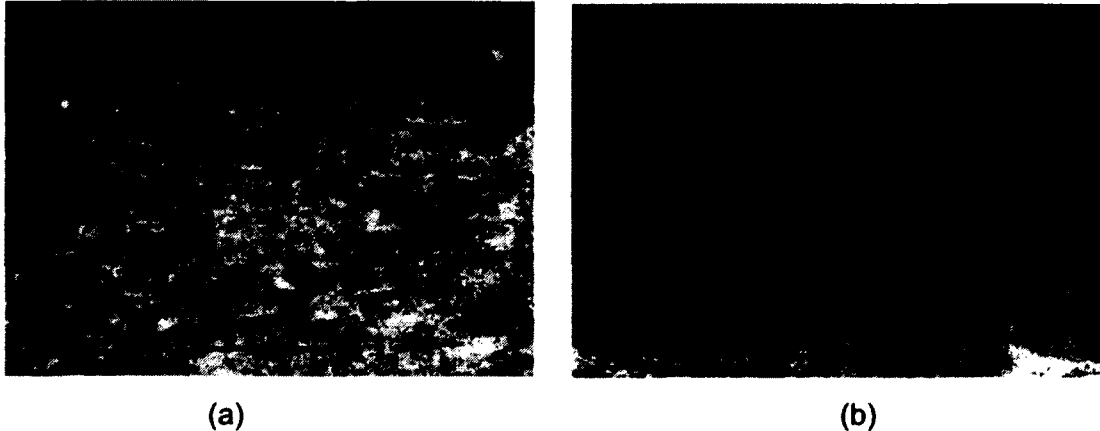


Figure 2.15: Cross section of the Al2024 alloy surface exposed to 3.5% NaCl pH=4 solutions. (a) Quench delay time = 27 s. (b) Quench delay time = 81 s [66].

#### 2.6.2.5 Stress Corrosion Cracking (SCC) after 2-step aging

Zailiang et al [67] studied the stress corrosion cracking of a high strength Al-4.4%Cu-0.6%Mg-0.8%Si alloy. Samples were solution treated at 500°C for 40 min followed by cooling in water, and then subjected to one step aging and two step aging conditions. The type and shape of precipitates on grain boundaries played a significant role in the stress corrosion cracking resistance. It was believed that narrow precipitate free zones will cause a higher SCC sensitivity, but there are many low angle grain boundaries with narrow precipitate free zones which do not follow a cracking path. Precipitate free zone width was found to increase with increase in aging temperature and time. They also concluded the precipitates on high-angle grain boundaries were as follows: GP zones



and  $\theta''$  phases are much more sensitive to SCC; continuous  $\theta'$  is the most sensitive to SCC; and the discontinuous  $\theta$  phase has no SCC sensitivity. A two-step aged specimen (160°C for 8h + 190°C for 2h) reduced the stress corrosion cracking sensitivity to a greater extent than a one step aged specimen (160°C for 8h). This is because of the second step aging at 190°C for 2h which introduced a large discontinuous  $\theta$  phase on the high angle grain boundaries [67].

## 2.7 Quality Index for Al alloys

The Quality index, Q is an empirical parameter that is often used to characterize the mechanical performance of 356/357 casting alloys [68]. The first quality index developed by Drouzy et al [68] is given by

$$Q = UTS + d \log (s_f) \quad 2.3$$

where UTS is the tensile strength (MPa),  $s_f$  is the elongation to fracture (%). Lines generated with Eq. 2.3 are called iso-Q lines.

The Yield Stress (YS) is related to UTS and  $s_f$  by

$$YS = a UTS - b \log (s_f) - c \quad 2.4$$

Although the concept was developed for 356/357 alloys, it has occasionally been applied to other alloy systems including 359, 319, 201 and Mg base alloys [68, 69]. Among the quality factors developed so far, only the ones by Cáceres and Tiryakioğlu et al supply a measure in terms of the ratio of the current to achievable ductility. Both indices determine the achievable quality from the work hardening characteristics of the specimen [70].

### 2.7.1 Cáceres analytical model

This analytical model provides an overview of the strength-ductility relationship of the material. The model describes the material with the following Ramberg-Osgood relationship [71]:

$$\sigma = K\epsilon^n \quad 2.4$$

where  $\sigma$  is the true stress,  $K$  is the strength coefficient,  $n$  is the strain hardening exponent and  $\epsilon$  is the true strain.

Eq. 2.5 and 2.7 were used for calculating iso- $q$  lines and iso-YS lines in Figure 2.16.

Ignoring the elastic component of the total strain, the nominal stress-strain curve can be approximated by

$$P = K [\ln(1+s)]^n e^{-\ln(1+s)} \cong K s^n e^{-s} \quad 2.5$$

$$n = s / q \quad 2.6$$

$$P = K s^{s/q} e^{-s} \quad 2.7$$

where  $P$  and  $s$  are the engineering values of stress and strain,  $q$  is the relative ductility parameter. The relative ductility parameter  $q$ , defined as the ratio between the strain hardening exponent of the material,  $n$  and the elongation to fracture,  $s_f$ .

The Quality index developed by Caceres is given by

$$Q = K [(qn)^n e^{-qn} + 0.4 \log(100qn)] \quad 2.8$$

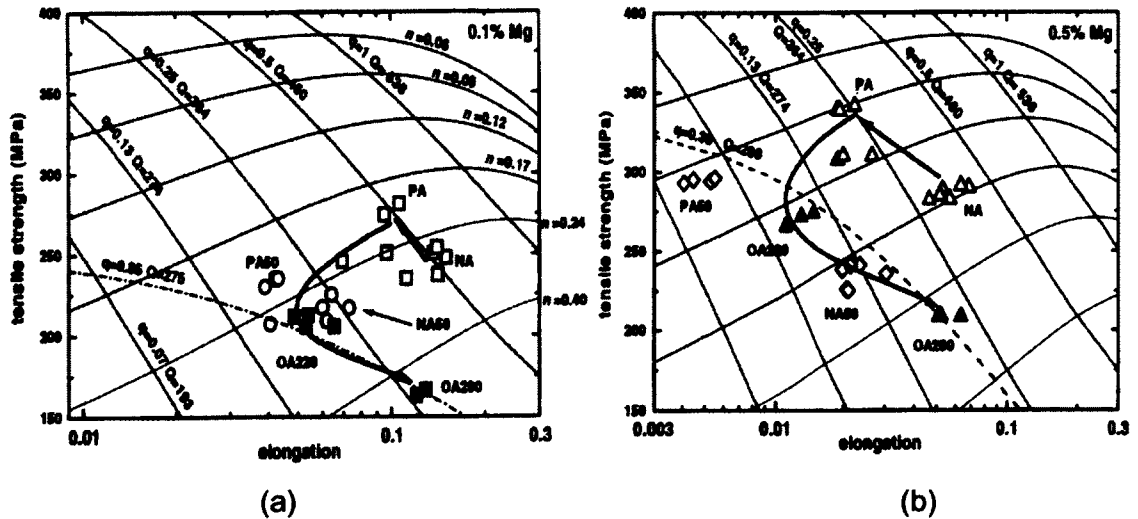


Figure 2.16: A quality index chart and tensile data for the Al-Cu-Si-Mg alloy with (a) 0.1%Mg and (b) 0.5%Mg. The arrows indicate the strength-ductility path for samples [68].

For the overaged materials, a new chart would be necessary, but to keep the data together on a single chart a single iso-q line (dotted lines in Fig. 2.16) was calculated for each overaged material for the alloy with 0.1%Mg and 0.5%Mg, respectively [68]. Heat treatments used in the quality index chart, Fig. 2.16, are listed in Table 2.7 [68]. All the samples were solution treated at 505°C for 9 hrs and quenched in warm water (60°C). For NA and NA50, Natural Aging (NA) was carried out for 3-8 weeks.

**Table 2.7:** Heat treatments applied to the tensile samples used in constructing Fig. 2.16

DAS ( $\mu\text{m}$ )	Natural Aging (NA)	32h/160°C Peak aging (PA)	20h/220°C Over Aging (OA)	24h/280°C Over Aging (OA)
25	NA	PA	OA220	OA280
50	NA50	PA50	**	**

The transition from higher Q-value to lower Q-value results in a circular pattern in quality index that closely resembles the behaviour of Al-Cu-Mg-Ag alloy 201 (refer to Fig.2.16) [68]. These charts allow for a systematic assessment of the effect of temper, microstructural parameters, and chemical composition on the mechanical performance of the material [71].

### 2.7.2 Quality index by Murat Tiryakioglu

Tiryakioglu et al [72] introduced a quality index,  $Q_E$  for Al-7%Si-Mg alloys based on the energy absorbed by the sample during tension test until failure. Toughness is given by

$$\psi = \int_0^{\epsilon_f} \sigma \, d\epsilon \quad 2.9$$

where  $\sigma$  is the true stress (MPa),  $\epsilon$  is the true strain, and  $\epsilon_f$  the true fracture strain.

This quality index can be used for all specimens regardless of their composition and processing history [72].

$$Q_E = \frac{\psi}{\psi_c} \quad 2.10$$

where  $\psi$  is the toughness of the specimen and  $\psi_c$  is the target toughness. Target toughness is the threshold toughness of the specimen. Toughness is calculated by the area under the true stress-strain curve.

### 2.7.3 Ductility potential of 206 alloys

Tiryakioglu et al [70] also reported on the ductility potential of 206 alloys. They used the yield strength-elongation relationship on premium quality castings. The material at and around the largest stress concentration yields before the rest of the material, flows plastically and work-hardens, making up, at least partially, for the loss in resistance to deformation. Thus yield strength should be relatively insensitive to defects, as is commonly observed [70]. Tiryakioglu et al introduced an empirical equation to predict the expected elongation ( $e_{F(e)}$ ) as a function of yield strength.

$$e_{F(e)} = \beta_0 \exp(-\beta_1 \sigma_Y) \quad 2.11$$

The curve drawn in Fig. 2.17 follows Eq. 2.11. The new quality index of 206 alloy castings developed by Tiryakioglu et al is given by [70].

$$Q_T = \frac{e_F}{71 \exp(-0.004\sigma_Y)} \quad 2.12$$

$e_F$  is the elongation to fracture (%) and  $\sigma_Y$  is the yield strength (MPa).

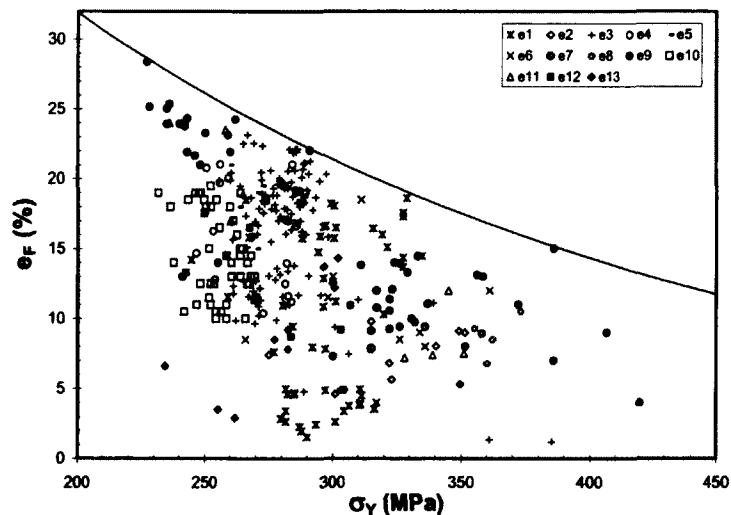


Figure 2.17: Yield strength-elongation relationship in 206 casting alloy. The highest point follows a curvilinear trend. There is a linear relationship between the maximum uniform elongation values and yield strength [70]. The datasets shown in Fig. 2.17 are listed in Table 2.8.

**Table 2.8:** The datasets used for yield strength-elongation relationship [71]:

Dataset	Number of samples	Alloy	Notes
e1	53	A206	Ingot, some HIPed
e2	8	A206	Permanent mold castings
e3	192	B206	Permanent mold castings
e4	20	B206	Permanent mold castings
e5	6	A206	Sand castings
e6	10	A206	Chilled plaster mold
e7	38	A206	Sand castings
e8	4	A206	Investment castings
e9	16	206, A206	Permanent mold
e10	58	A206	Sand castings
e11	7	A206	Premium castings
e12	6	206	Sand cast test bars
e13	13	A206	Premium castings

### Quality index of B206 alloy

Sigworth and Major [1] reported the quality index of B206 alloy using the formulations proposed by Caceres. According to the theory by Caceres, they used the following quality index relationship for the B206 alloy [1]:

$$Q = UTS + 270 \log E \quad 2.13$$

where Q is the quality index (MPa), UTS is the Ultimate Tensile Strength (MPa), and E is the elongation to fracture in the tensile specimen. They found that Mg, Mn, Si and Fe reduce the quality in the T7 temper. For maximizing elongation, these elements have to be kept low. In the T4 temper, Fe and Mn will decrease the quality. The effect of Si was insignificant for the T4 temper [1].

## CHAPTER 3: EXPERIMENTAL DETAILS

### 3.1 Tensile test bar casting

The ASTM B108 tensile test bar casting was performed at the Stahl Specialty Company in Kingsville, MO. Fig.3.1 shows the casting for the tensile test bar. The dashed lines point out the locations (regions 1,2,3,4) where the samples were extracted for the heat treatments. The “bulb” end located at the bottom of the as-cast tensile test bar (gripping end) shows a homogeneous and higher integrity structure. Increased microporosity and copper segregation is expected in parts of the casting, especially at locations just underneath the risers (region 5).



Figure 3.1: B206 tensile test bar.

#### 3.1.1 Chemical composition of B206 alloy specimens

The chemical composition of the cast alloy is given in Table 3.1:

**Table 3.1:** Chemical Composition of B206 alloy specimens

%Cu	%Mg	%Mn	%Fe	%Si	%Zn	%Ni	%Sn	%Ti
4.783	0.303	0.437	0.028	0.072	0.009	<0.001	0.0015	0.014

### 3.2 UMSA platform

The Universal Metallurgical Simulator and Analyzer (UMSA) Technology Platform (US Patent No. 7,354,491) was mainly used to optimize the Solution Treatment (ST) parameters for the B206 alloy. The heating and cooling curves obtained from the UMSA platform gives information about the undissolved Al-Cu phases during solution treatment. Dissolving these Al-Cu phases will improve B206 alloy performance.

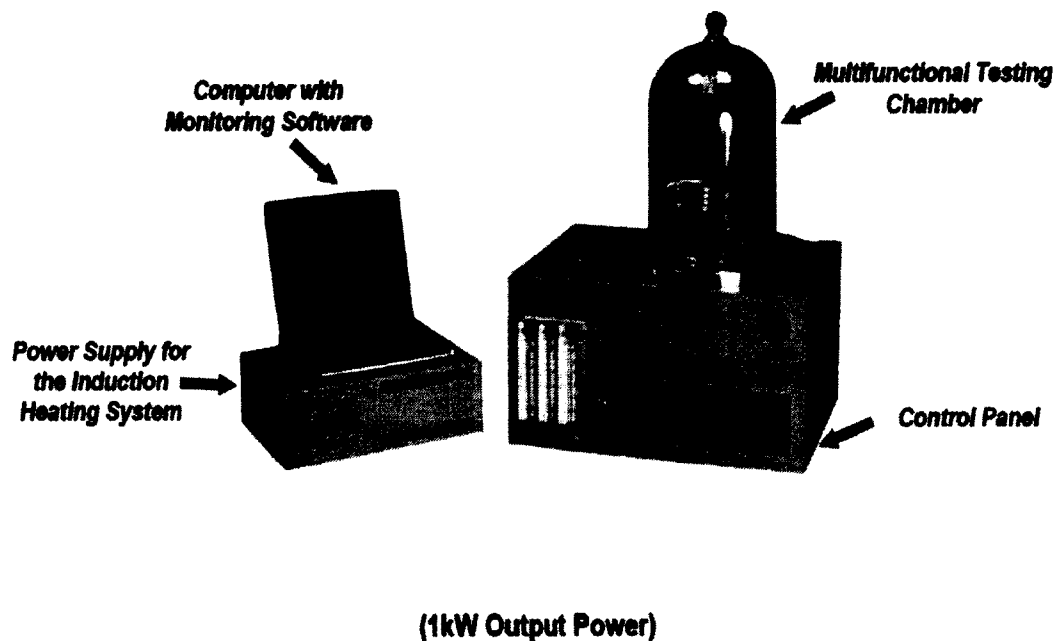


Figure 3.2: UMSA Platform at the University of Windsor.

Figure 3.3 shows the heating and cooling cycles for the B206 alloy. The first derivative of heating and cooling curves, Fig. 3.4, details the beginning and end of a phase's melting and solidifying process.

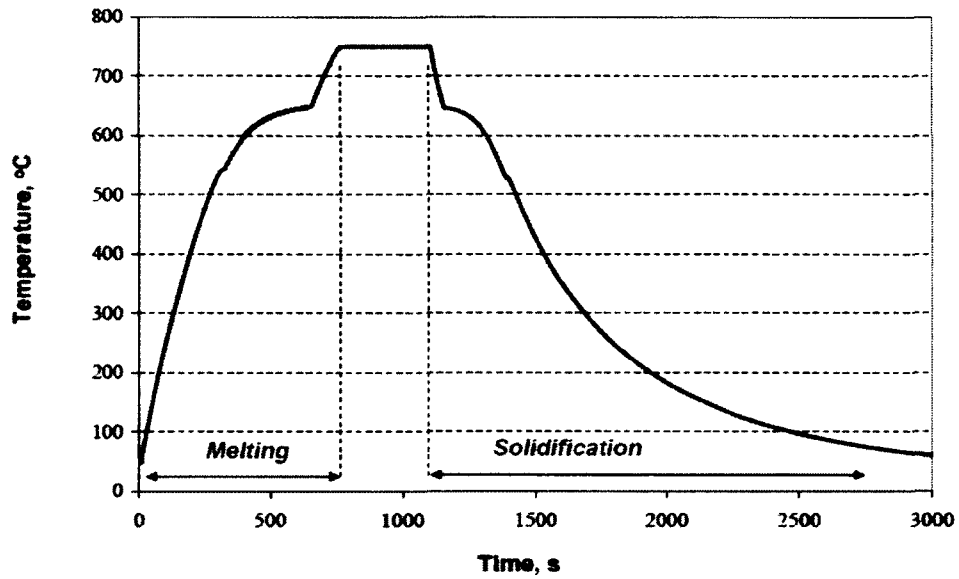


Figure 3.3: Temperature vs. Time curve of the UMSA Melting and Solidification Cycles for the B206 alloy.

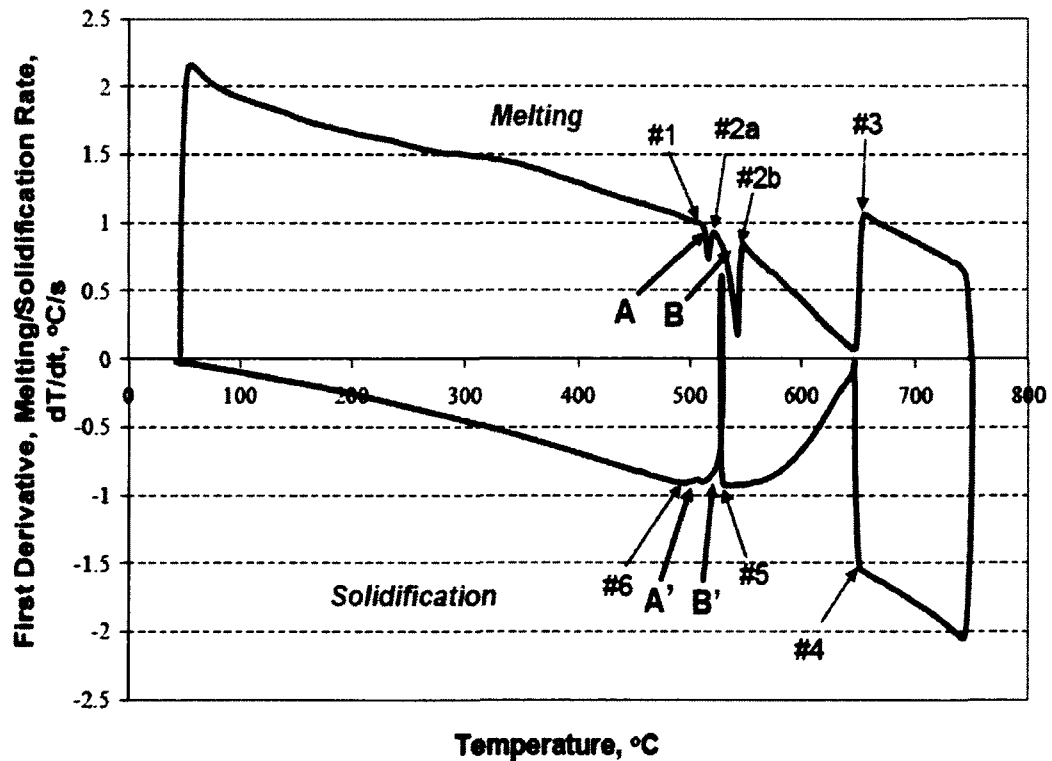


Figure 3.4: First derivative of the heating (melting) and cooling (solidification) curves vs. temperature for the B206 alloy.

The melting of phase A ranges from 513-524°C and the melting of phase B ranges from 524-549°C. These phases must be dissolved during Solution Treatment (ST) in order to



maximize the B206 alloy's performance. Thus, the ST temperature can be held in these phases' melting range for a particular time to dissolve them.

**Table 3.2:** Heating cycle of the B206 alloy.

Locations marked in Fig. 3.4	Thermal Characteristics	Heating Rate 0.3°C/s
		Temperature °C
1	Start (beginning) of the alloy (phase A) melting process	513.1 ± 1.6
2a	Start (beginning) of the phase B melting process	523.9±1.5
2b	Finish (end) of the phase B melting process	549.0 ± 2.0
3	Finish (end) of the alloy melting process	661.5 ± 2.8

**Table 3.3:** Cooling cycle of the B206 alloy

Locations marked in Fig. 3.4	Thermal Characteristics	Cooling Rate 0.5°C/s
		Temperature °C
4	Liquidus temperature	651.5 ± 0.6
5	Nucleation of phase B	529.8±0.5
6	Finish (end) of the alloy solidification (Solidus temperature)	494.4 ± 5.0
Solidification range		157.1

### 3.3 First series Heat Treatment

#### 3.3.1 2-step Solution Treatment (ST)

The conventional 2-step Solution Treatment (ST) cycle recommended by the American Foundry Society [8] is as follows:

- First step: hold for 2 hrs at a temperature of 493-504°C (920-940°F)
- Second step: gradually increase the temperature to 527-532°C (980-990°F) and hold for 8 hrs

- Water Quench: 66+°C (150+°F)

### **3.3.2 Natural Aging (NA) followed by 1-step Artificial Aging (AA)**

The following aging cycles were performed immediately after the 2-step Solution Treatment:

- NA: 21 and 168 hrs.
- NA: 24 hrs and AA @ 160°C for 5, 10, 24 and 48 hrs.
- NA: 24 hrs and AA @ 180°C for 2.5, 5, 10 and 120 hrs.
- AA @ 150°C for 0.5, 1, 2 and 8 hrs.
- AA @ 200°C for 0.5, 1, 2, 3 and 8 hrs

The above heat treatment combinations involving 2-step Solution Treatment + Natural Aging + Artificial Aging were used to give preliminary mapping of the B206 alloy engineering characteristics. The first series heat treatment is shown schematically in Figure 3.5.

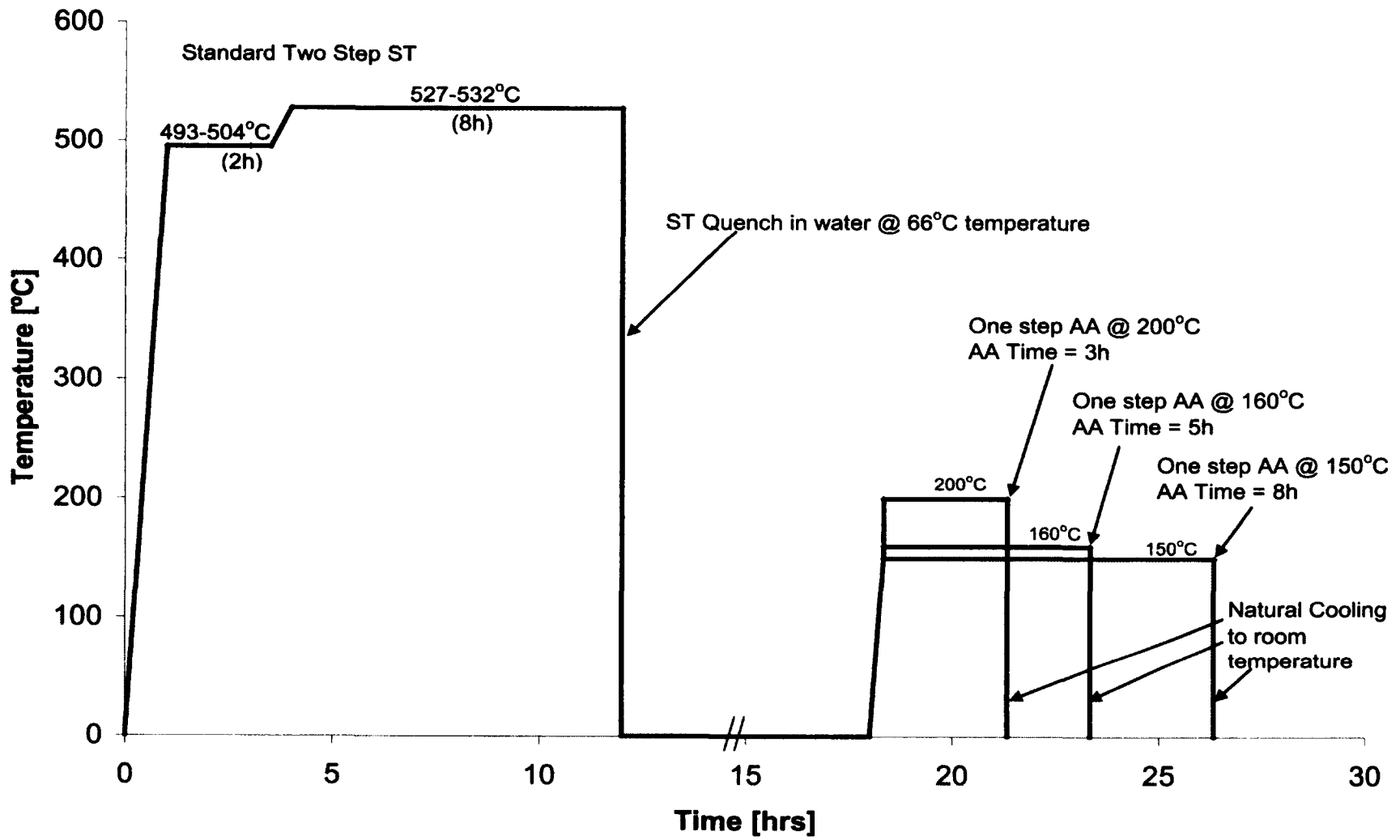


Figure 3.5: Two Step Solution Treatment and One Step Artificial Aging Treatment

### **3.4 Second Series Heat Treatment**

The second series heat treatment was performed using a Lindberg resistance furnace. The temperature/ time profile was recorded by inserting a K-type thermocouple 30 mm down into the centre of riser end of tensile bar for sample temperature monitoring during heat treatment. Tensile test bars were solution treated according to the same 2-step Solution Treatment (ST) procedure detailed in the first series heat treatment. After ST, the tensile test bars were subjected to 3 days of NA before AA. Tensile test bars were then Artificially Aged to one of the following schedules:

- 225°C for 2, 6 hrs.
- 200°C for 1, 2, 3, 4, 8, 24 hrs.
- 175°C for 18, 24, 48 hrs.
- 150°C for 1, 2, 4, 8, 24 hrs.
- 125°C for 1, 2, 4, 8, 24, 48 hrs.
- 100°C for 6, 12, 24, 48, 120 hrs.

### **3.5 Third Series Heat Treatment**

#### **3.5.1 Modified 3-step Solution Treatment**

The two-step Solution Treatment (ST) was replaced by a three-step Solution Treatment (ST) to maximize the dissolution of  $Al_2Cu$  phase. Such a three-stage treatment gives rise to improved homogenization of the alloy as seen from metallographic observations. Heat Treatment was performed using forced air movement capabilities for uniform temperature distribution across the treated batch of test samples. The tensile test bar instrumented with the thermocouple was used for control of the entire heat treatment operation.

In this study, we have adopted a 3-step Solution Treatment (ST) schedule, which is detailed in Table 3.4 and shown schematically in Figure 3.6.

**Table 3.4:** 3-step Solution Treatment (ST) schedule.

Step	Temperature °C /°F	Time		
		Holding hrs	Ramp Up min	Total hrs
1	515/959	3	34	3.56
2	530/986	8	15	8.25
3	535/995	4	11	4.18
Water Quench	66/151	--	--	--

### 3.5.2 Aging (Natural + Artificial)

A combination of Natural (NA) + Artificial Aging (AA) treatments was used with the 3-step Solution Treatment (ST). The AA treatments included both one-step (Table 3.5) and two-step (Table 3.6) processes. The 2-step AA involves an intermediate quench at 50°C, which can promote nucleation of fine precipitates [40]. The mechanical properties can be improved by this interrupted aging process.

**Table 3.5:** Natural Aging (NA) (0 and 24 hrs) followed by one step Artificial Aging (AA) performed at 175°C for 12 hrs

Sample ID	NA hrs	AA Temp °C/°F	AA Time		
			Holding hrs	Ramp up min	Total hrs
0-F-8	0	175/347	12	15	12.25
24-F-8	24				

In all sample ID, the first number '0 or 24' represents 0 or 24 hrs of Natural Aging (NA) and B, C, D, E & F represents different heat treatment levels. The number '8' indicates the 8<sup>th</sup> heat treatment batch.

**Table 3.6:** Summary of Natural Aging (NA) and Artificial Aging (AA) parameters for machined samples: Natural Aging (NA) (0 hrs and 24 hrs) followed by a two step Artificial Aging (AA) treatment.

Levels	Sample ID	NA, hrs	AA Step	AA Temp, °C/°F	AA Time		
					Holding, hrs	Ramp up, min	Total, hrs
Level 1	0-B-8	0	1 - 2 -	190/374 130/266	1. 0.5	18 to 20	21.13
Level 2	0-C-8				2. 20		31.13
Level 3	0-D-8				1. 0.5		24.63
Level 4	0-E-8				2. 30		34.63
Level 5	24-B-8	24			1. 4		21.13
Level 6	24-C-8				2. 20		31.13
Level 7	24-D-8				1. 0.5		24.63
Level 8	24-E-8				2. 30		34.63

Note: Intermediate quenching at 50°C/122°F for 1 hr was carried out between the two Artificial Aging (AA) steps.

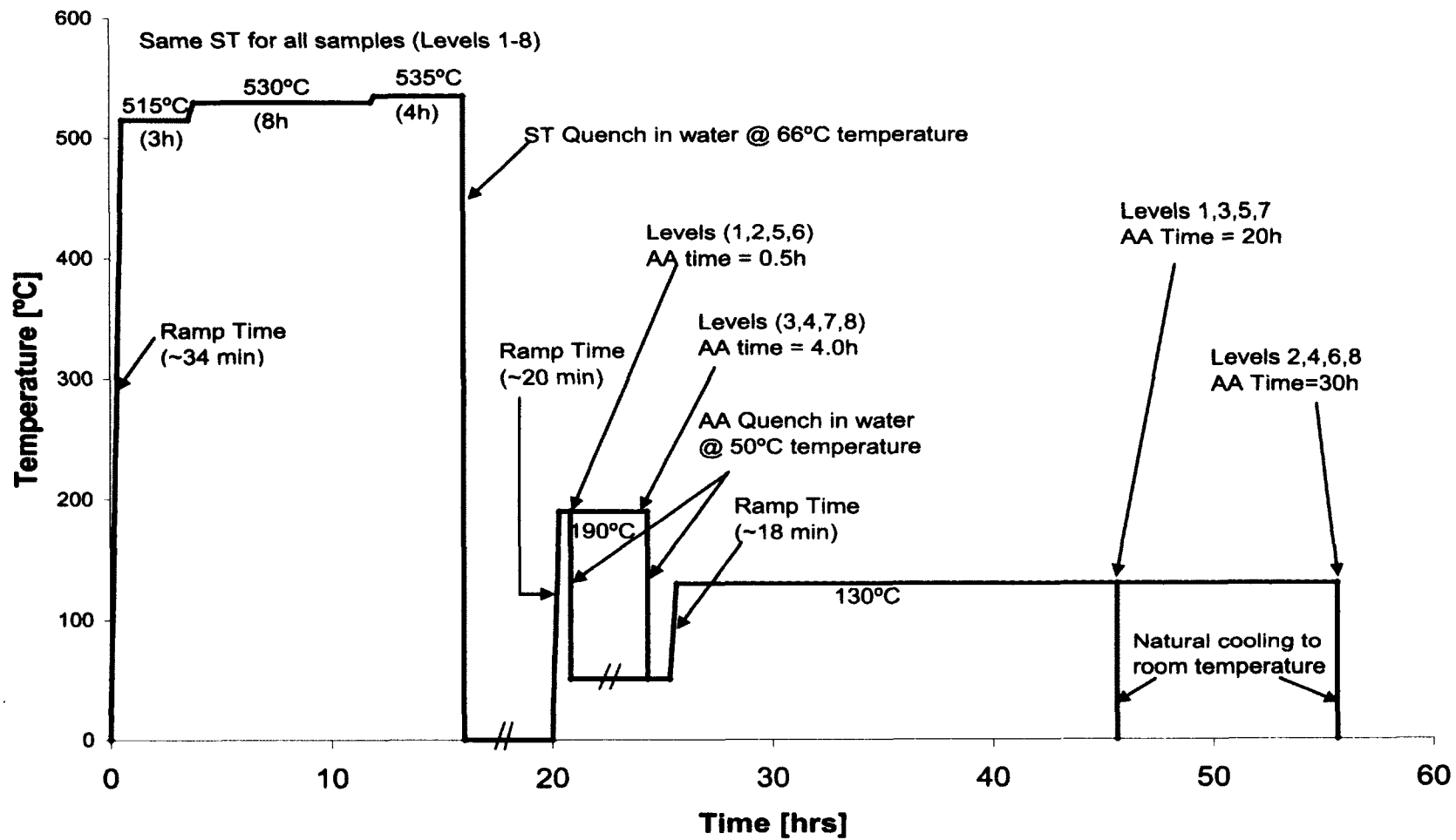


Figure 3.6: Three Step Solution Treatment (ST) and Two Step Artificial Aging

### 3.6 Corrosion Test Sample Preparation

The sample dimensions are 18mm diameter and 29mm height.

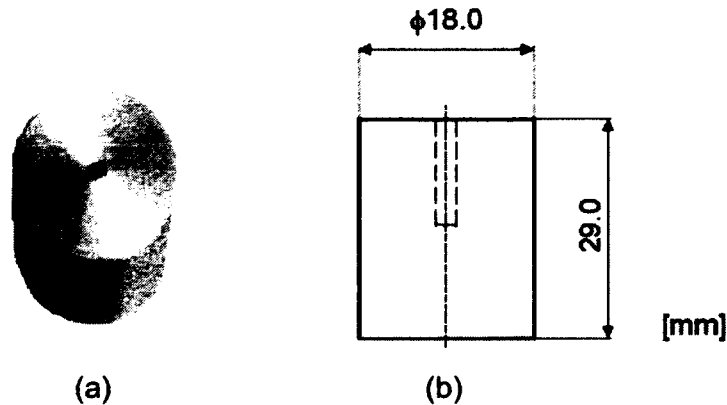


Figure 3.7: (a) Overall view of the corrosion test sample, (b) profile drawing of the corrosion test sample.

### 3.7 Corrosion Testing Methods

#### 3.7.1 Immersion corrosion testing

The bulb end of the tensile test bars were used for the immersion corrosion tests. Tests were conducted according to the ASTM G 110-92 procedure [73], namely:

- Before testing, the passive layer was removed using concentrated nitric acid.
- Test specimens were immersed in a corrosive solution containing 57 g of sodium chloride, 10 ml of 30% hydrogen peroxide in 1 litre of distilled water.
- Ambient air temperature: 30°C (86°F).
- Corrosion test duration: 6 hrs.

Standard metallographic grinding and polishing techniques using semi-automatic equipment were used for the corrosion test sample sections. In order to keep excellent edge retention for subsurface microscopic observations after corrosion testing, the test samples were mounted in a hard resin. Figure 3.8 shows (a) a sample immersed in corrosive solution and (b) a corroded specimen.



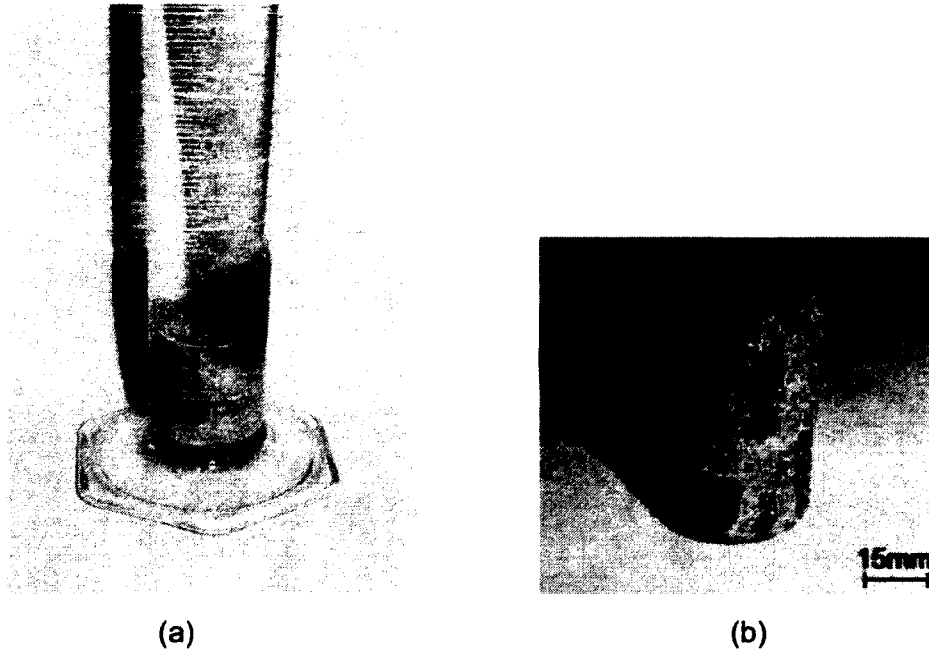


Figure 3.8: (a) specimen immersed in the corrosive solution, (b) corroded specimen.

### 3.7.2 Potentiodynamic testing

The bulb end of the tensile test bars were used for the potentiodynamic tests. Potentiodynamic testing using a Solarton 1285 Potentiostat, Fig. 3.9, with CorrWare for Windows was performed to analyze the corrosion resistance of the heat treated B206 alloy. The reference electrode (saturated calomel) was connected to the cell using a solution bridge, while a platinum wire served as the counter electrode. Once the specimen surface was polished to 600 grit, the working electrode (test specimen) was introduced into the cell and exposed to the test solution which comprised an aqueous solution containing 57g of NaCl+10ml of 30% H<sub>2</sub>O<sub>2</sub> per litre. The scan rate employed was 1mV.s<sup>-1</sup>.

The polarization resistance was calculated using the following equation

$$R_p = \frac{\beta_a \beta_c}{2.3i_{corr} (\beta_a + \beta_c)} \quad 3.1$$

where  $\beta_a$ ,  $\beta_c$ ,  $i_{corr}$ , and  $R_p$  are the Tafel slopes of the anodic and cathodic reactions, the corrosion current density and polarization resistance, respectively [74].

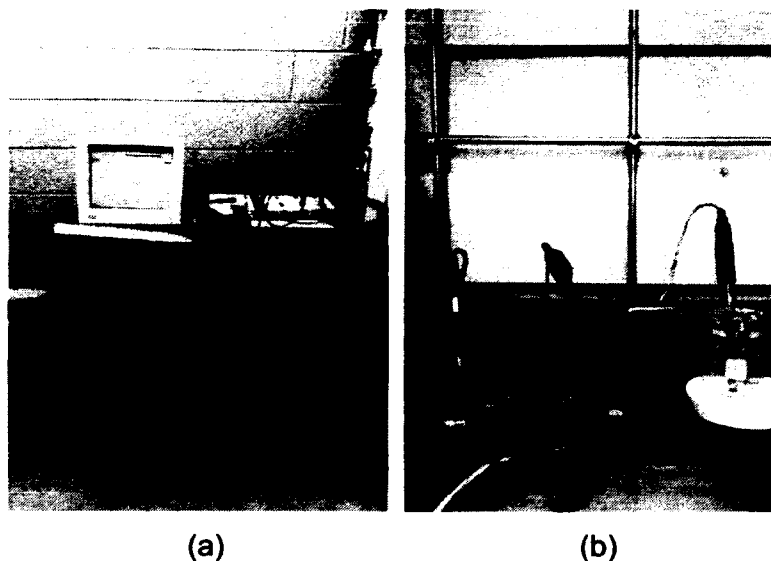


Figure 3.9: (a) Solarton 1285 potentiostat (b) 3-electrode setup.

### 3.7.3 Tribocorrosion tests

Test samples 0-C-8, 24-F-8 and 0-D-8 (having poor and good corrosion resistance in the immersion test method) were selected for the tribocorrosion tests, Fig. 3.10. Tribocorrosion tests were performed using a three electrode set-up including the working electrode (B206 test samples), the reference electrode (saturated calomel electrode) and the counter electrode (platinum coil). The sample dimensions used for tribocorrosion tests had a diameter = 18mm and a height = 5mm. The three electrodes were connected to a galvanostat/ potentiostat, which is an electronic device that maintains the selected potential between working and reference electrodes by passing an appropriate current between working and counter electrodes. The potential was measured at a fixed current as a function of the time to follow the evolution of the electrochemical kinetics of the involved reactions. The rubbing test was performed for 1800 cycles against a 5mm alumina ball under a load of 0.9 kg (2 pounds). Rubbing corresponds to a decrease in potential due to the accelerated corrosion of the bare aluminum alloy exposed to the solution after abrasion of the passive film. When rubbing stops, the potential increases again to the value before rubbing, since the alloy passivates again. 3.5 % NaCl solution was used as the corrosive medium. It was interesting to note that the potential measured during rubbing flows mainly through the wear track area, an area much smaller (in the present experimental configuration) than the overall metal area exposed to the solution. The open circuit potential (OCP) was also recorded during and after tribocorrosion tests.

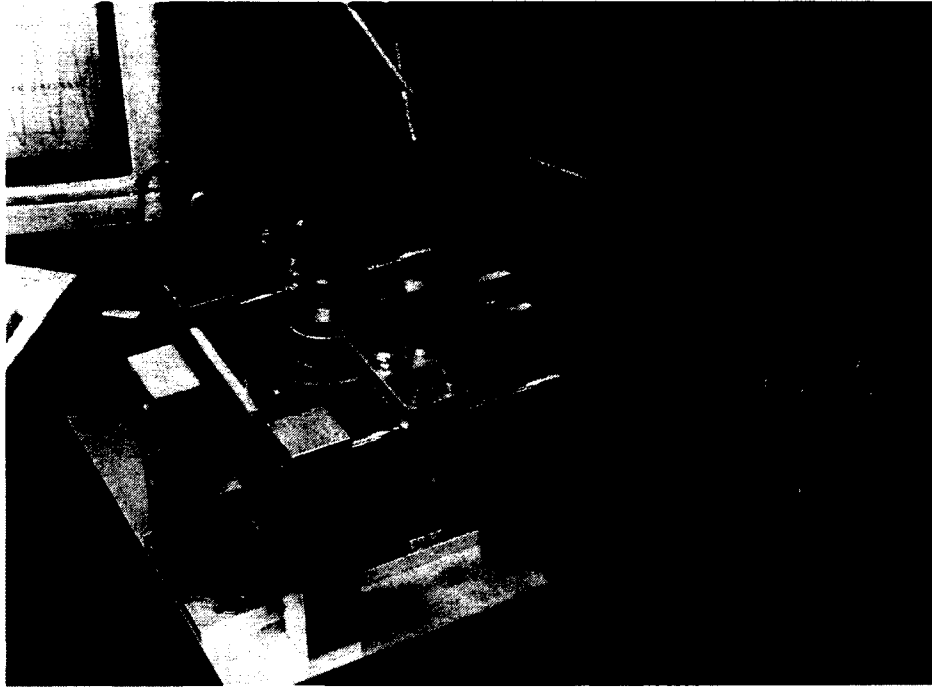


Figure 3.10: Tribocorrosion apparatus at McGill University [75].

Figure 3.11 shows the overview of the heat treatments, mechanical properties and corrosion testing.

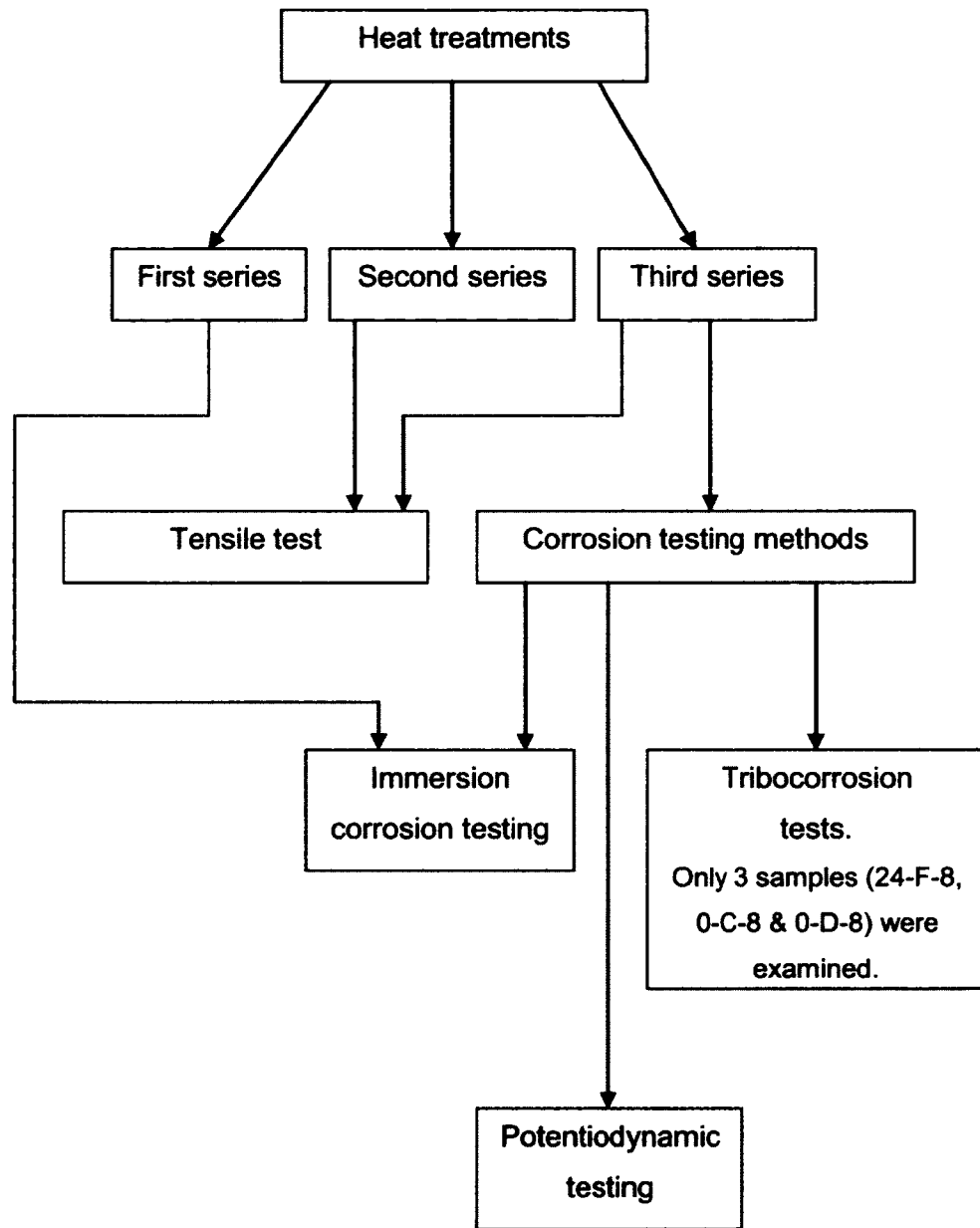


Figure 3.11: Overview of the heat treatments and its corresponding testing methods.

## CHAPTER 4: RESULTS AND DISCUSSIONS

### 4.1 As-cast Structure analysis before the immersion corrosion test

The as-cast microstructure was characterized before the immersion corrosion testing was conducted. A heterogeneous distribution of the Al-Cu phases was found to exist throughout the as-cast structure.

Figure 4.1a shows the overall as-cast microstructure with constituents located on the grain boundaries. Two different shades of Al-Cu phases were found in Fig. 4.1c and 4.1d. Higher magnification (up to 5000X) examination revealed that some of Al<sub>2</sub>Cu constituents (containing up to 60wt% Cu) most likely nucleated during the solidification process as a result of the pre-existing Fe, Mn, Al and Si rich particles (refer to Fig. 4.2). The chemical composition of the metal matrix is inhomogeneous.

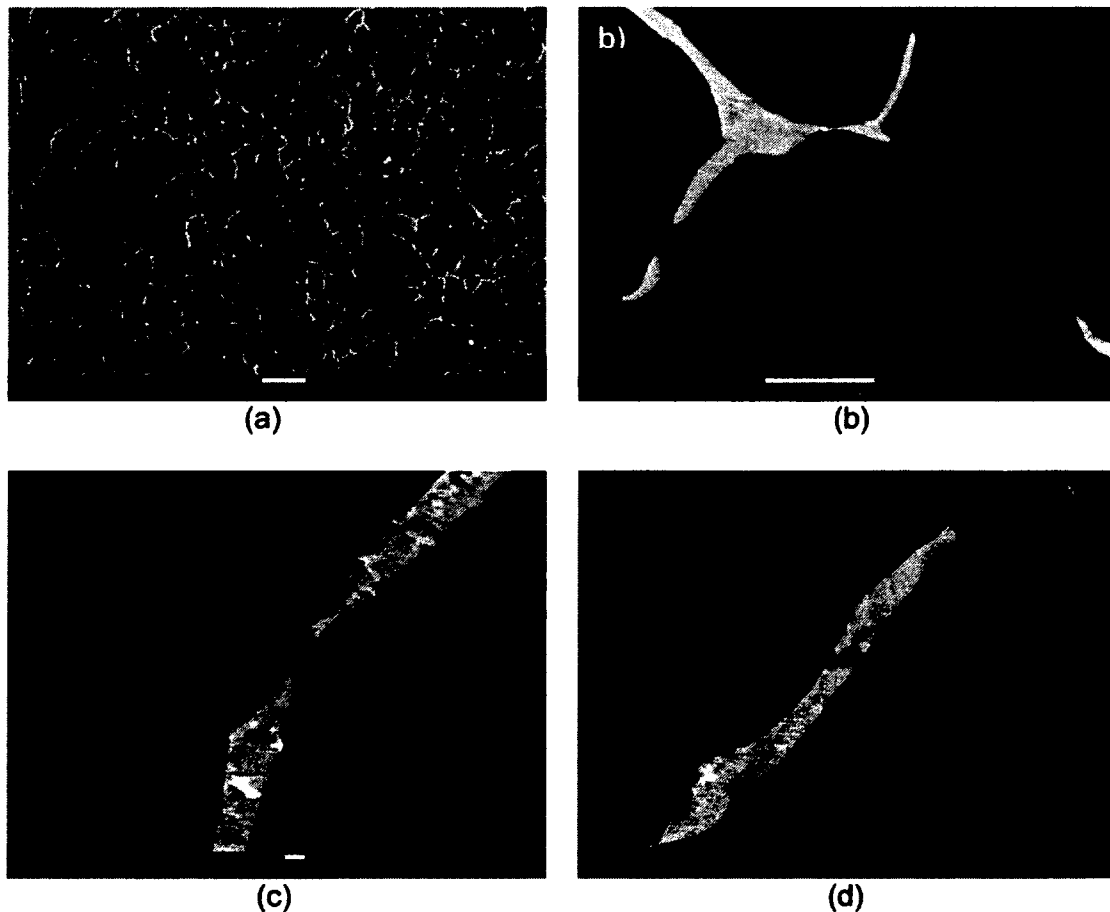


Figure 4.1: (a), (b), (c) & (d) SEM micrographs of the as-cast B206 test sample before the immersion corrosion test.

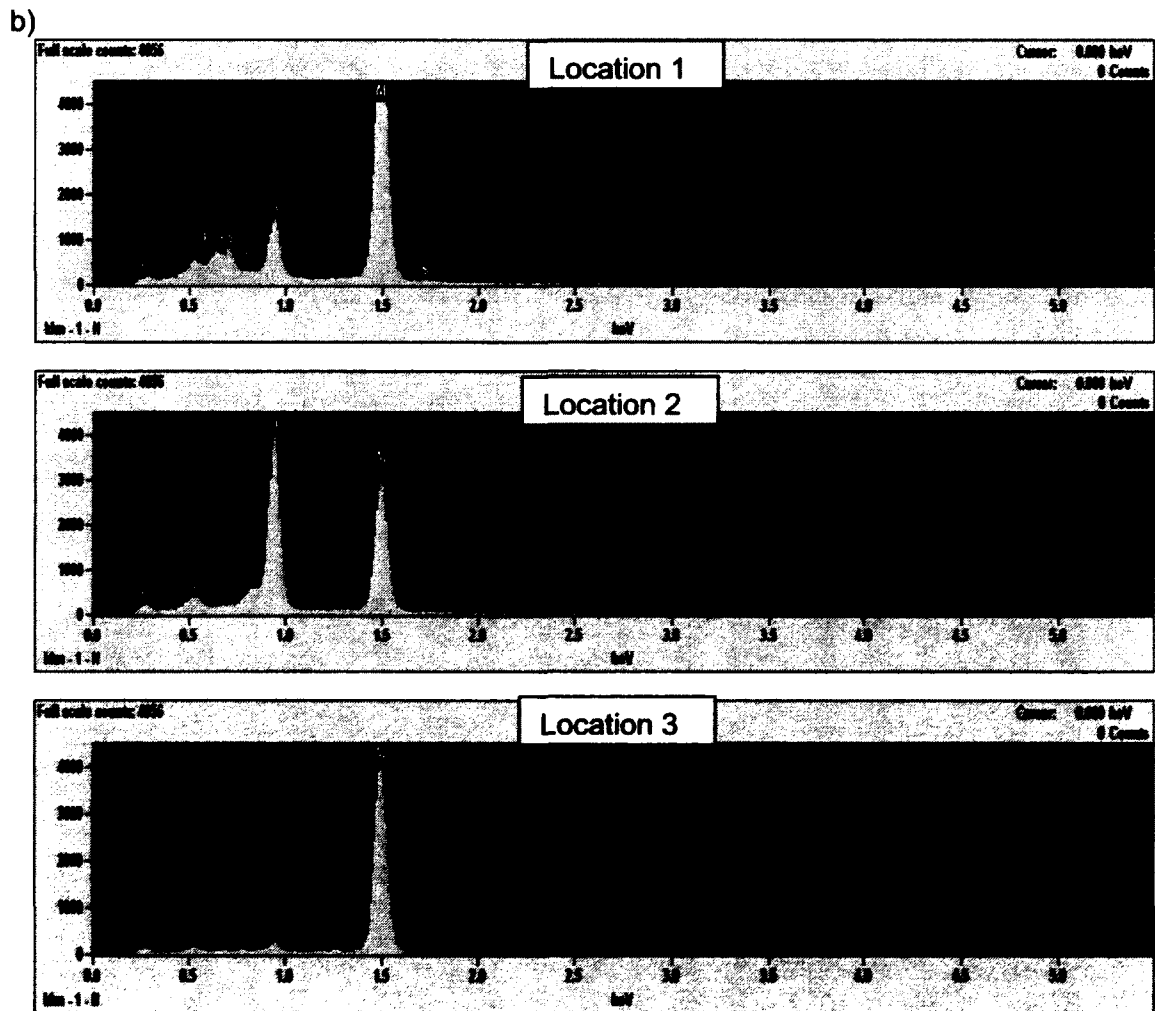
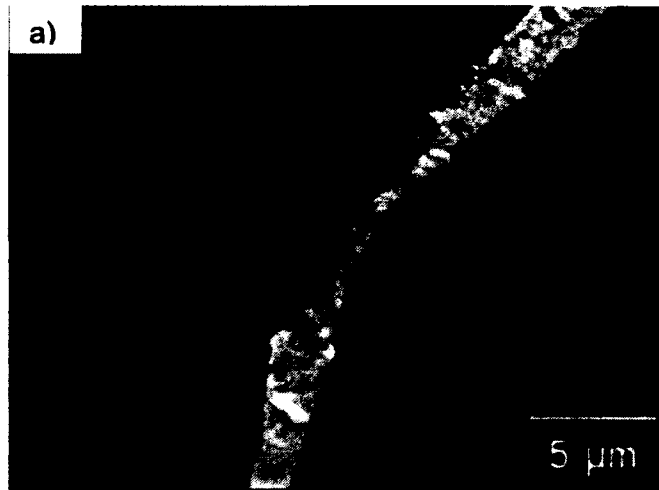


Figure 4.2: a) SEM micrograph of the as-cast B206 test sample before the immersion corrosion test b) X-Ray microanalysis spectrum.

The X-ray microanalysis data for Fig. 4.2 is summarized in Table 4.1. Analysis (Figure 4.2 & 4.3) performed on and near the Al<sub>2</sub>Cu phases of as-cast sample show Cu content varied in the range of 1.4 – 60 wt%. Point 1 in Figure 4.2 has 57 wt% Al, 19 wt% Cu, 19 wt% Fe, 0.46 wt% Si whereas point 2 has 60 wt% Cu, 34 wt% Al. Depending on the wt% of the elements, two different shades of Al-Cu phases are visible in Figure 4.2.

**Table 4.1:** Quantitative X-ray microanalysis data for Fig. 4.2

Locations marked in Fig. 4.2	Weight %					
	C	O	Al	Si	Fe	Cu
1	3.08	1.68	56.67	0.47	19.00	19.14
2	4.24	2.40	33.70			59.66
3	7.50	1.66	84.85			5.99

Another region in the as-cast sample (Figure 4.3) show the presence of Mn (0.31 – 0.63 wt%) along with Cu near the Al<sub>2</sub>Cu phase regions. In Fig. 4.3, nine different locations were selected near the Al<sub>2</sub>Cu phase and their corresponding wt % of Cu, Al & Mn was obtained. The Cu content varied in the range of 1.40 – 4.58 wt% in the grain matrix: see Table 4.2.

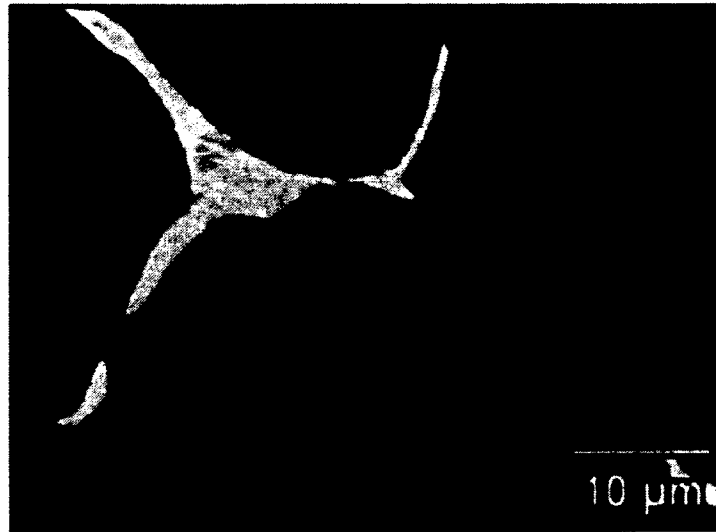


Figure 4.3: SEM micrograph of the as-cast B206 test sample before the immersion corrosion test.

Table 4.2: Quantitative X-ray microanalysis data for Fig. 4.3

Locations marked in Fig. 4.3	Weight %		
	Al	Mn	Cu
1	98.21	0.39	1.40
2	97.81	0.46	1.73
3	96.38	0.54	3.07
4	94.78	0.63	4.58
5	95.54	0.43	4.03
6	95.32	0.62	4.07
7	95.73	0.57	3.71
8	96.23	0.50	3.26
9	96.57	0.31	3.13



#### 4.2 As-cast Structure analysis after the immersion corrosion test

As-cast sample was subjected to immersion corrosion test. SEM micrographs in Figure 4.4 show the corrosion attacked regions of the as-cast sample. Generally, corrosion penetrates along the  $Al_2Cu$  phase regions in the grain boundaries. These undissolved  $Al_2Cu$  phase regions initiates the intergranular corrosion attack of the B206 alloy. The micrographs show clear distinction between the surface and subsurface attack. Going toward the center of the sample, it can be seen that there are much finer corrosion "paths" which also follow the network of the  $Al_2Cu$  constituents. A relatively small amount of uncorroded and/or partially corroded  $Al_2Cu$  constituents are visible in the corroded regions.

EDS microanalysis of the corrosion products revealed that the network of  $Al_2Cu$  constituents is preferentially corroded. Figure 4.4 (a) – (f) shows the penetration of corrosion attack along the Al-Cu phases in the grain boundaries.

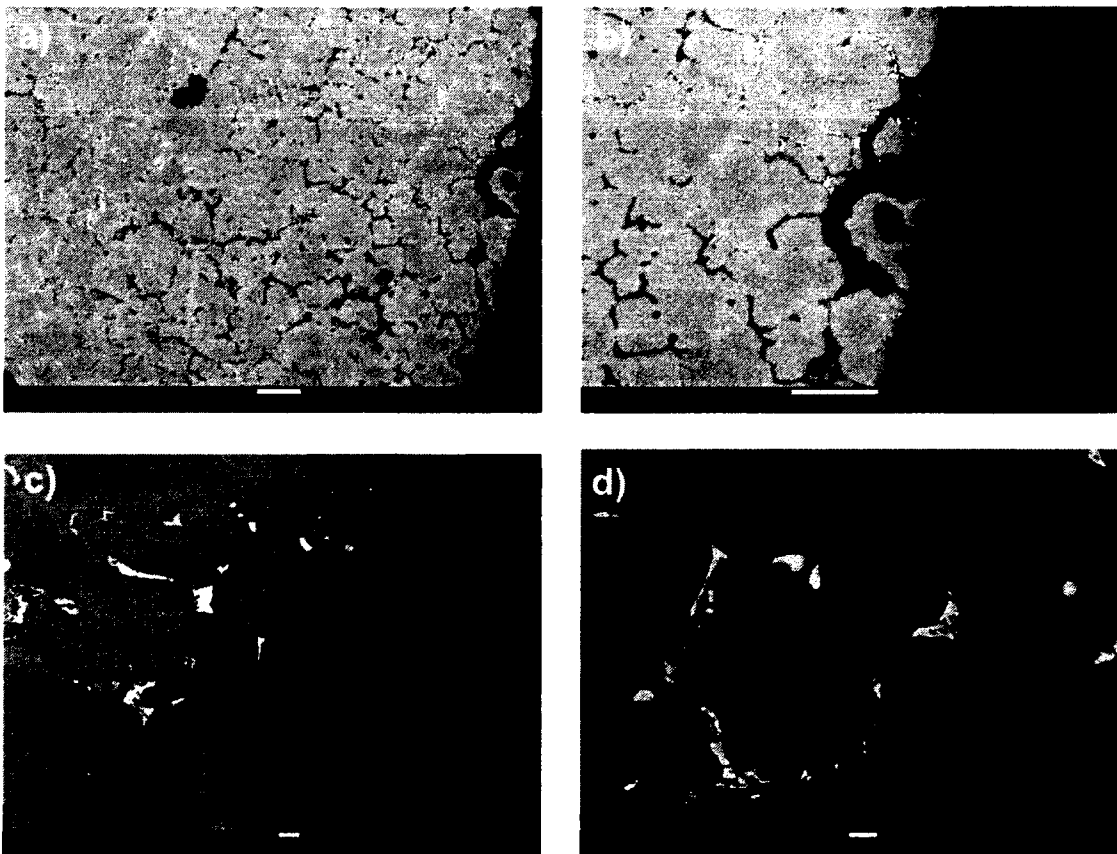


Figure 4.4: SEM micrographs of the as-cast B206 test sample after the immersion corrosion test.



Figure 4.4: e) & f) SEM micrographs of the as-cast B206 test sample after the immersion corrosion test.

The corrosion path can be very wide: Figs. 4.4c) and e). Analysis performed on the grain boundary regions of the as-cast sample show different wt% of Cu, Mn and Mg. Point 1 in Figure 4.5 has 4 wt% Cu, 0.77 wt% Mn and 0.17wt% Mg. Point 2 has no copper, Mn and Mg: see Table 4.3.



Figure 4.5: a) SEM micrograph of the as-cast B206 test sample after the immersion corrosion test

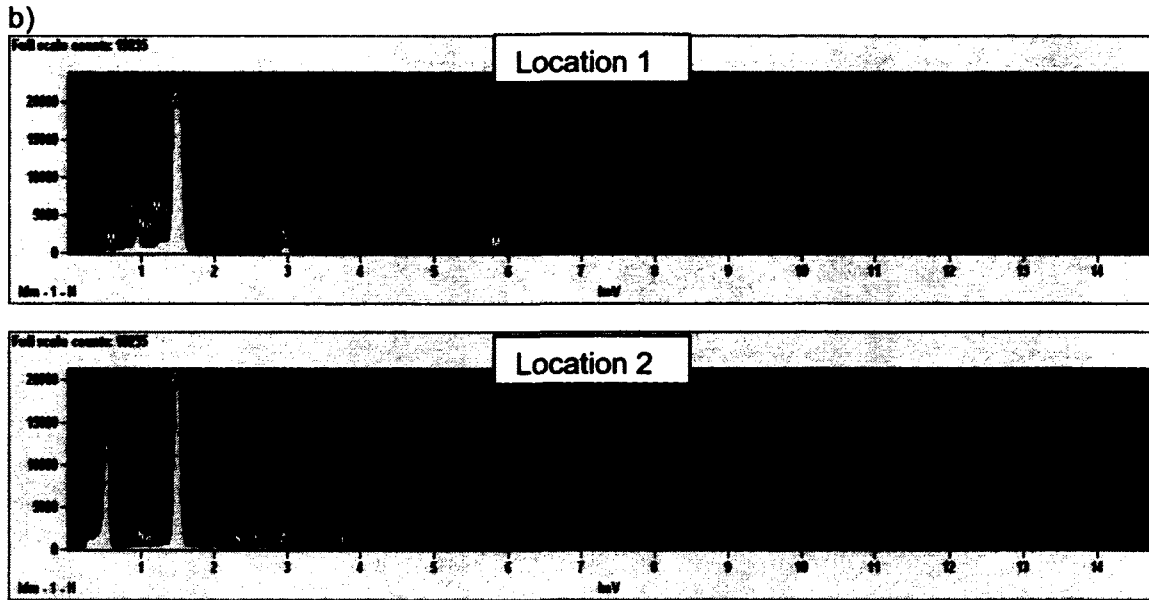


Figure 4.5: b) X-ray microanalysis spectrum

Table 4.3: X-ray microanalysis quantitative data for Fig. 4.5a).

Locations marked in Fig. 4.5a)	Weight %									
	O	Na	Mg	Al	P	S	Cl	Ca	Mn	Cu
1	1.41	0.00	0.17	93.65					0.77	4.0
2	53.1	0.23		45.33	0.49	0.10	0.54	0.18		

The fine structured corrosion products have substantially different chemical compositions (including O, Al, Cl, Ca, P, S, Na, Mg and Mn) in comparison with the coarse and cracked corrosion products (Fig. 4.5).

### 4.3 Metallographic Analysis of Corrosion Mode and Severity for the First Series Heat Treatments

Microscopic observations of B206 alloy test samples (subjected to 2-step ST followed by NA and 1-step AA) revealed a highly non-uniform intergranular corrosion along the perimeter of the samples. The severity of corrosion was calculated by measuring the maximum intergranular corrosion depth for all samples in as-cast and heat treated conditions. In the present study, one metallographic transverse section per corrosion test sample was utilized and the "maximum corrosion depth" is reported. LOM micrographs are given in Figures 4.6 - 4.10.

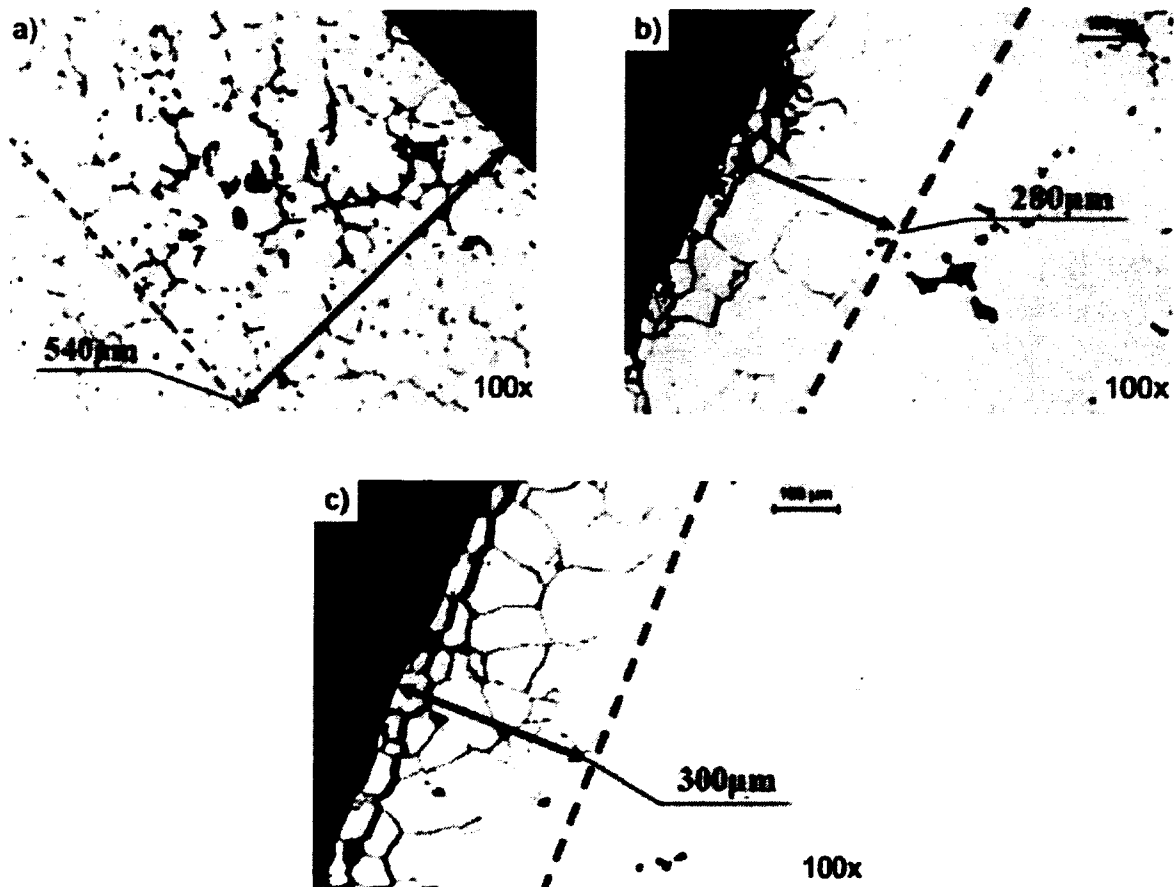


Figure 4.6: LOM Micrographs of cross-sections of immersion corrosion test samples:

a) As-cast condition

b) 2-step ST (493-504°C/2h, 527-532°C/8h, water quenching (66°C)) and NA 24 hrs

c) 2-step ST (493-504°C/2h, 527-532°C/8h, water quenching (66°C)) and NA 168 hrs.

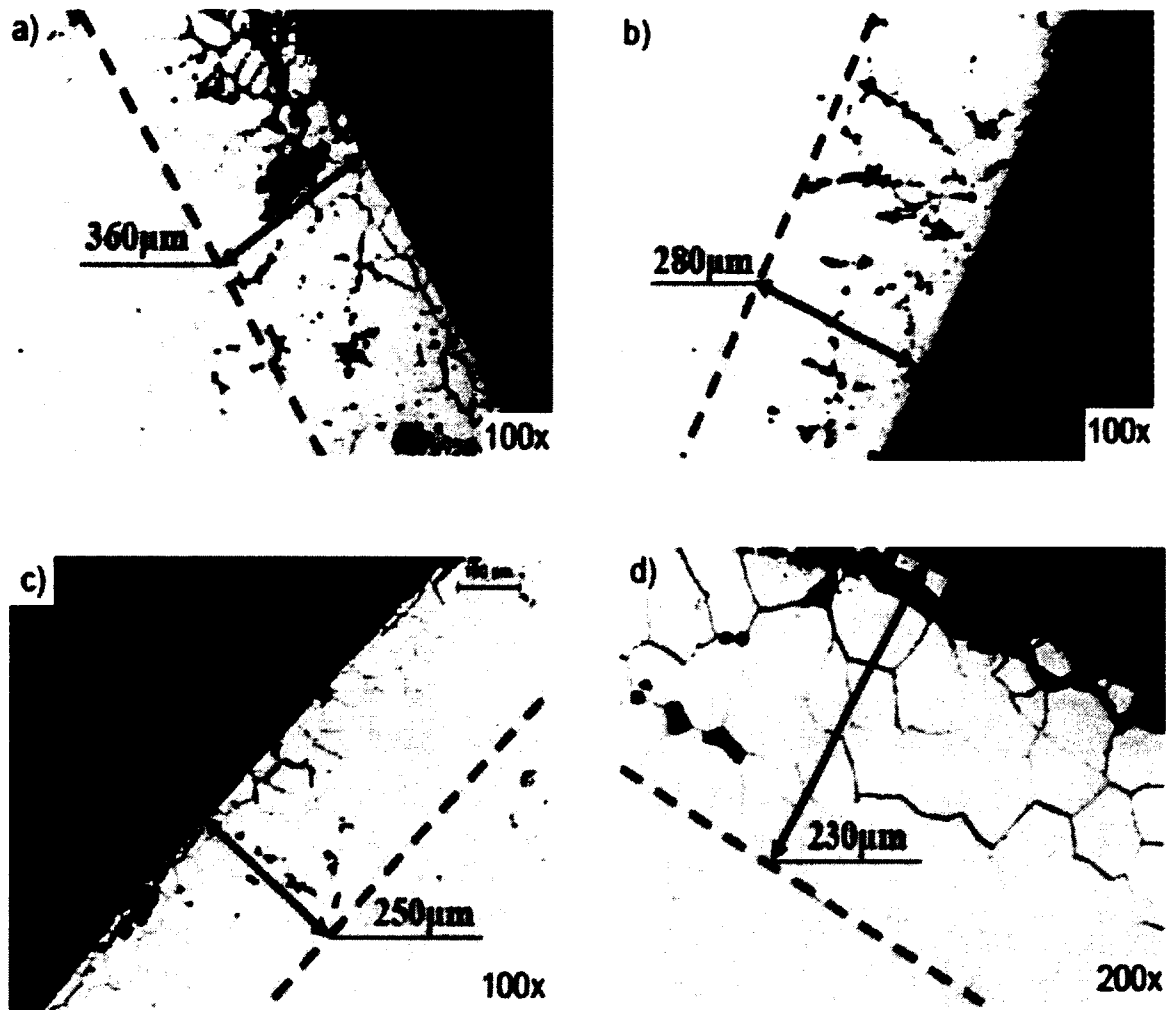


Figure 4.7: LOM Micrographs of cross-sections of immersion corrosion test samples:

- a) 2-step ST(493-504°C/2h, 527-532°C/8h, water quenching (66°C)) and AA @ 150°C/0.5h.
- b) 2-step ST (493-504°C/2h, 527-532°C/8h, water quenching (66°C)) and AA @ 150°C/1h.
- c) 2-step ST (493-504°C/2h, 527-532°C/8h, water quenching (66°C)) and AA @ 150°C/2h.
- d) 2-step ST (493-504°C/2h, 527-532°C/8h, water quenching (66°C)) and AA @ 150°C/8h.

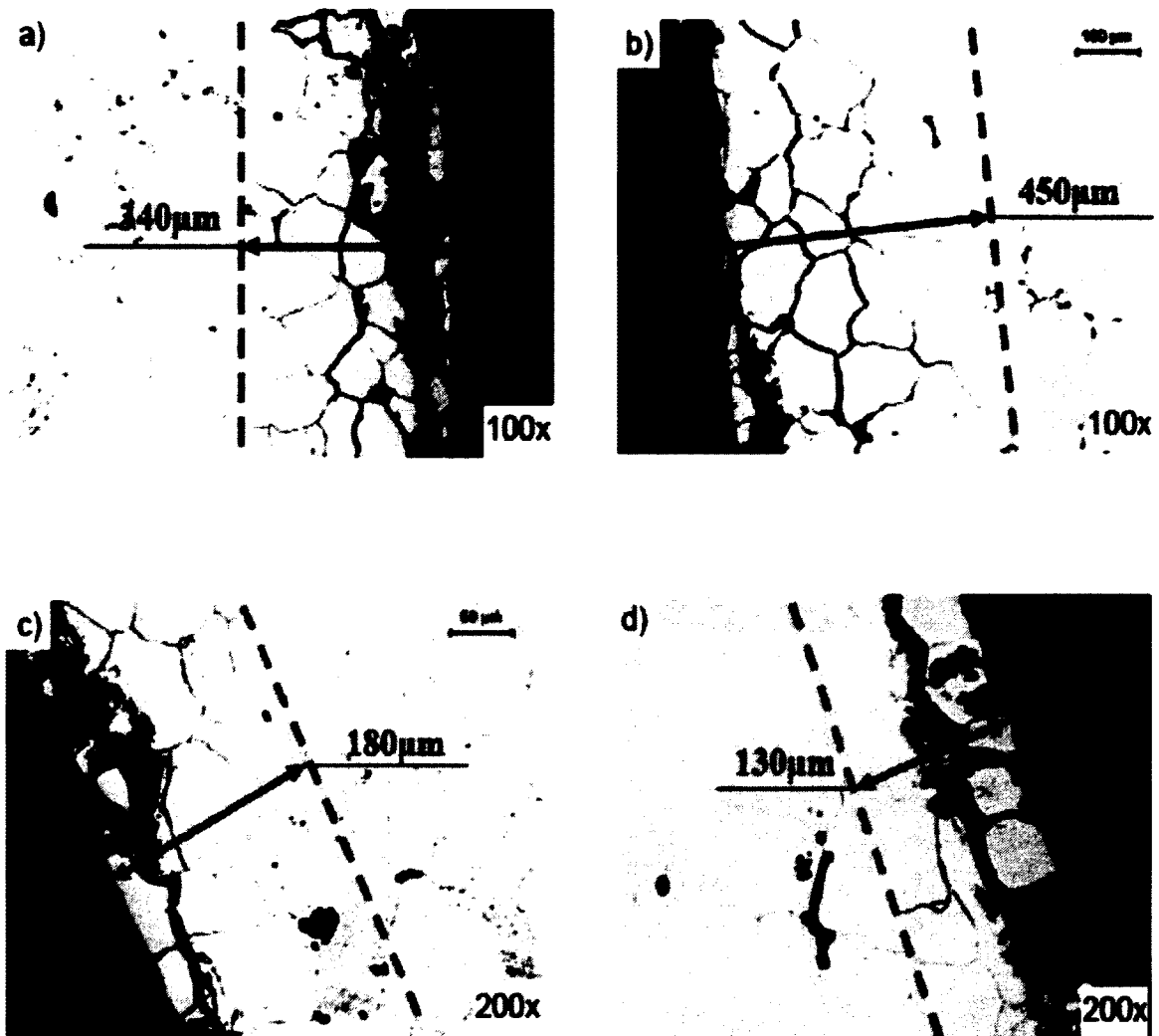


Figure 4.8: LOM Micrographs of cross-sections of immersion corrosion test samples:

a) 2-step ST (493-504°C/2h, 527-532°C/8h, water quenching (66°C)), NA 24h and AA @ 160°C/5h.

b) 2-step ST (493-504°C/2h, 527-532°C/8h, water quenching (66°C)), NA 24h and AA @ 160°C/10h.

c) 2-step ST (493-504°C/2h, 527-532°C/8h, water quenching (66°C)), NA 24h and AA @ 160°C/24h.

d) 2-step ST (493-504°C/2h, 527-532°C/8h, water quenching (66°C)), NA 24h and AA @ 160°C/48h.

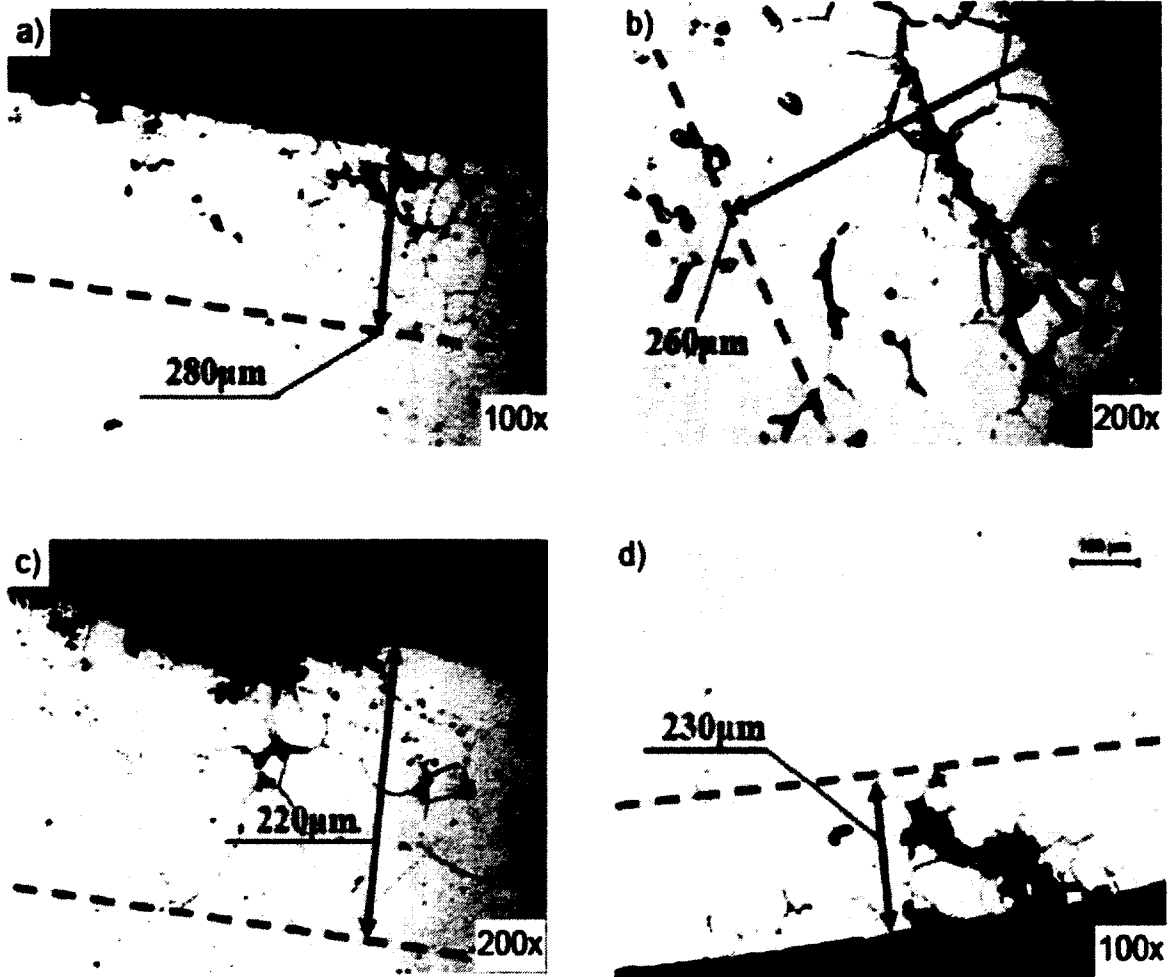


Figure 4.9: LOM Micrographs of cross-sections of immersion corrosion test samples:

- a) 2-step ST (493-504°C/2h, 527-532°C/8h, water quenching (66°C)), NA 24h and AA @ 180°C/2.5h.
- b) 2-step ST (493-504°C/2h, 527-532°C/8h, water quenching (66°C)), NA 24h and AA @ 180°C/5h.
- c) 2-step ST (493-504°C/2h, 527-532°C/8h, water quenching (66°C)), NA 24h and AA @ 180°C/10h.
- d) 2-step ST (493-504°C/2h, 527-532°C/8h, water quenching (66°C)), NA 24h and AA @ 180°C/120h.

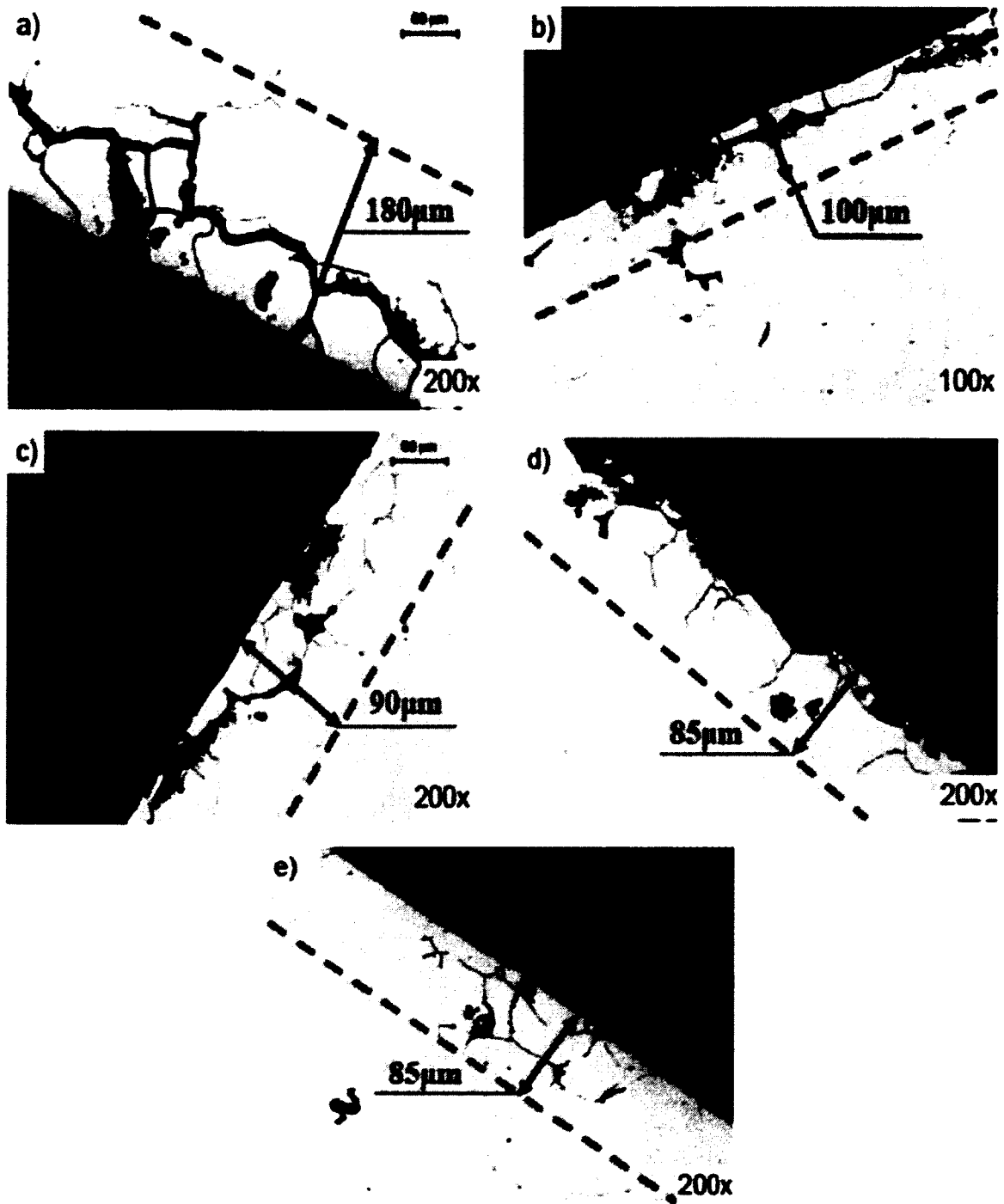


Figure 4.10: LOM Micrographs of cross-sections of immersion corrosion test samples:  
 a) 2-step ST (493-504°C/2h, 527-532°C/8h, water quenching (66°C)), AA @ 200°C/0.5h.  
 b) 2-step ST (493-504°C/2h, 527-532°C/8h, water quenching (66°C)), AA @ 200°C/1h.  
 c) 2-step ST (493-504°C/2h, 527-532°C/8h, water quenching (66°C)), AA @ 200°C/2h.  
 d) 2-step ST (493-504°C/2h, 527-532°C/8h, water quenching (66°C)), AA @ 200°C/3h.  
 e) 2-step ST (493-504°C/2h, 527-532°C/8h, water quenching (66°C)), AA @ 200°C/8h.



Test samples subjected to 2-step ST (493-504°C/2h, 527-532°C/8h, water quenching (66°C)) and AA @ 200°C for different aging times 2h, 3h, & 8h) exhibits highest corrosion resistance in the first series heat treatment experiments (see Table 4.4).

**Table 4.4:** Corrosion results for the first series heat treatments.

<b>Sample ID</b>	<b>Heat treatment</b>	<b>Maximum Intergranular corrosion depth, <math>\mu\text{m}</math></b>	<b>Maximum Pitting corrosion depth, <math>\mu\text{m}</math></b>
AC	As-cast	540	0
NA24	NA 24 hrs	280	0
NA168	NA 168 hrs	300	0
150-0.5	AA @ 150°C/0.5h	360	0
150-1	AA @ 150°C/1h	280	0
150-2	AA @ 150°C/2h	250	0
150-8	AA @ 150°C/8h	230	0
160-5	NA 24h, AA @ 160°C/5h	340	0
160-10	NA 24h, AA @ 160°C/10h	450	0
160-24	NA 24h, AA @ 160°C/24h	180	0
160-48	NA 24h, AA @ 160°C/48h	130	50
180-2.5	NA 24h, AA @ 180°C/2.5h	280	30
180-5	NA 24h, AA @ 180°C/5h	260	70
180-10	NA 24h, AA @ 180°C/10h	220	50
180-120	NA 24h, AA @ 180°C/120h	230	200
200-0.5	AA @ 200°C/0.5h	180	80
200-1	AA @ 200°C/1h	100	30
200-2	AA @ 200°C/2h	90	25
200-3	AA @ 200°C/3h	85	60
200-8	AA @ 200°C/8h	85	70

The sample showing the highest corrosion resistance (2-step ST (493-504°C/2h, 527-532°C/8h, water quenching (66°C)) and AA @ 200°C/3h) was analysed before the immersion corrosion test (Fig. 4.11). Large precipitates, that are not interconnected, are present on the grain boundaries. Precipitate free zones are present inside the grains and along the boundaries.

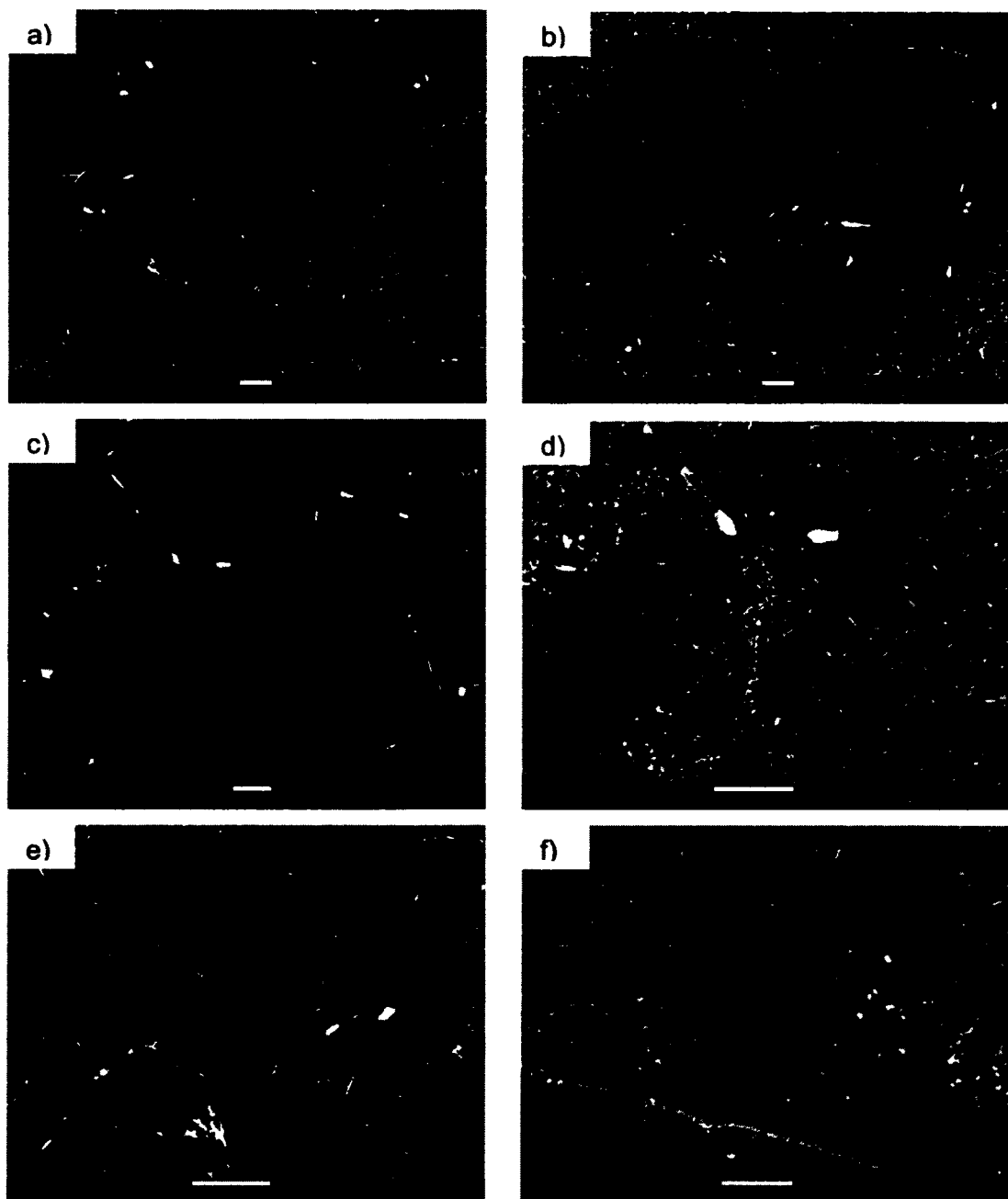


Figure 4.11: a), b), c), d), e) & f) SEM micrographs before immersion corrosion test.

Figure 4.12 show heterogeneous distribution of the precipitates (some that are needle-like in the grains and grain boundaries. These precipitates are rich in Al, Cu, Mn and Si. The spot 1 refers to the needle-like precipitate having 88.75wt%Al, 0.24wt%Si, 3.29wt%Mn and 7.72wt%Cu. The spot 2 refers to the precipitate on the grain boundary having 70.65wt%Al, 0.58wt%Si, 14.85wt%Mn, 1.46wt%Fe and 12.46wt%Cu. X-ray microanalysis data for Fig. 4.12a) are detailed in Table 4.5.

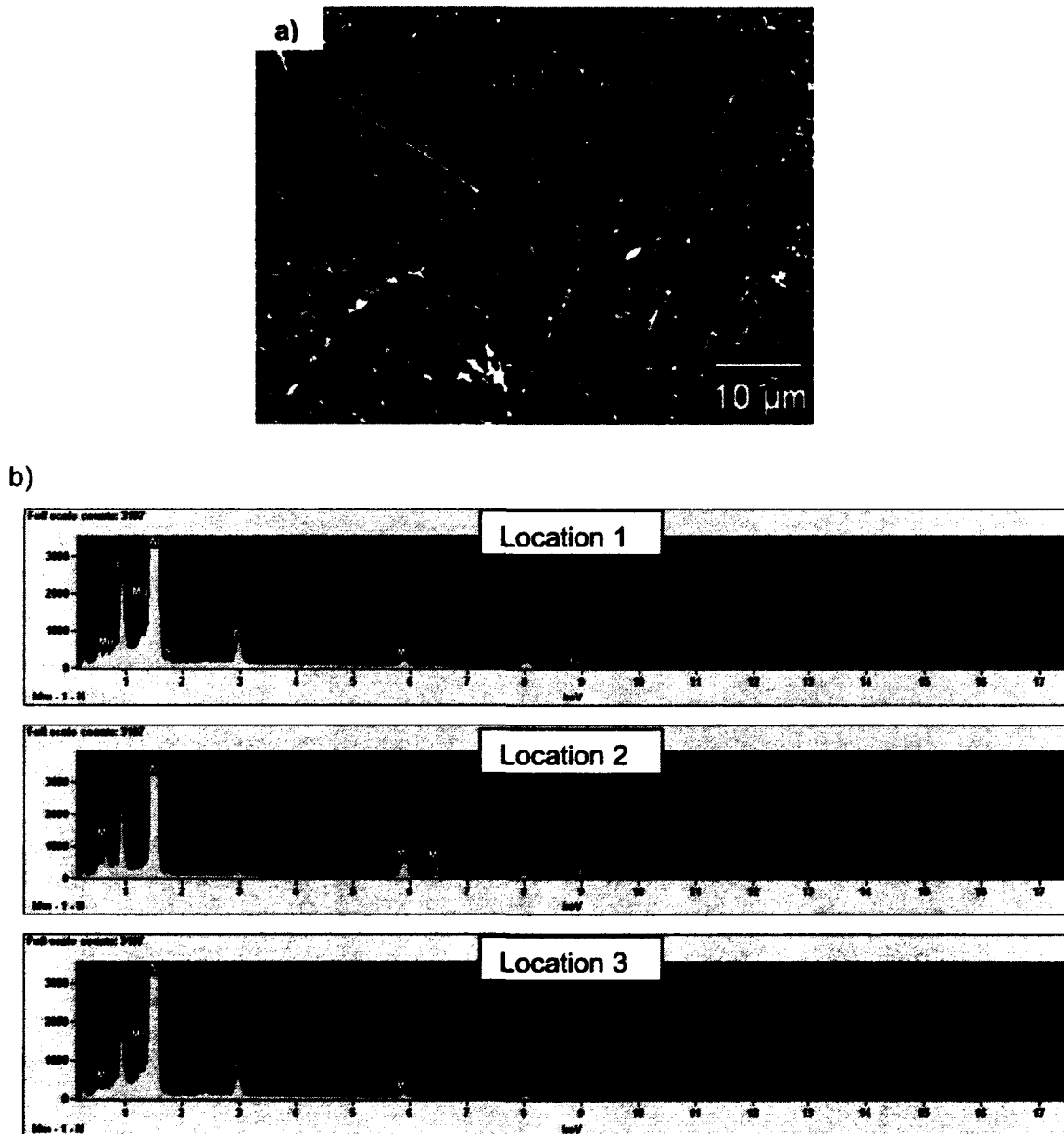
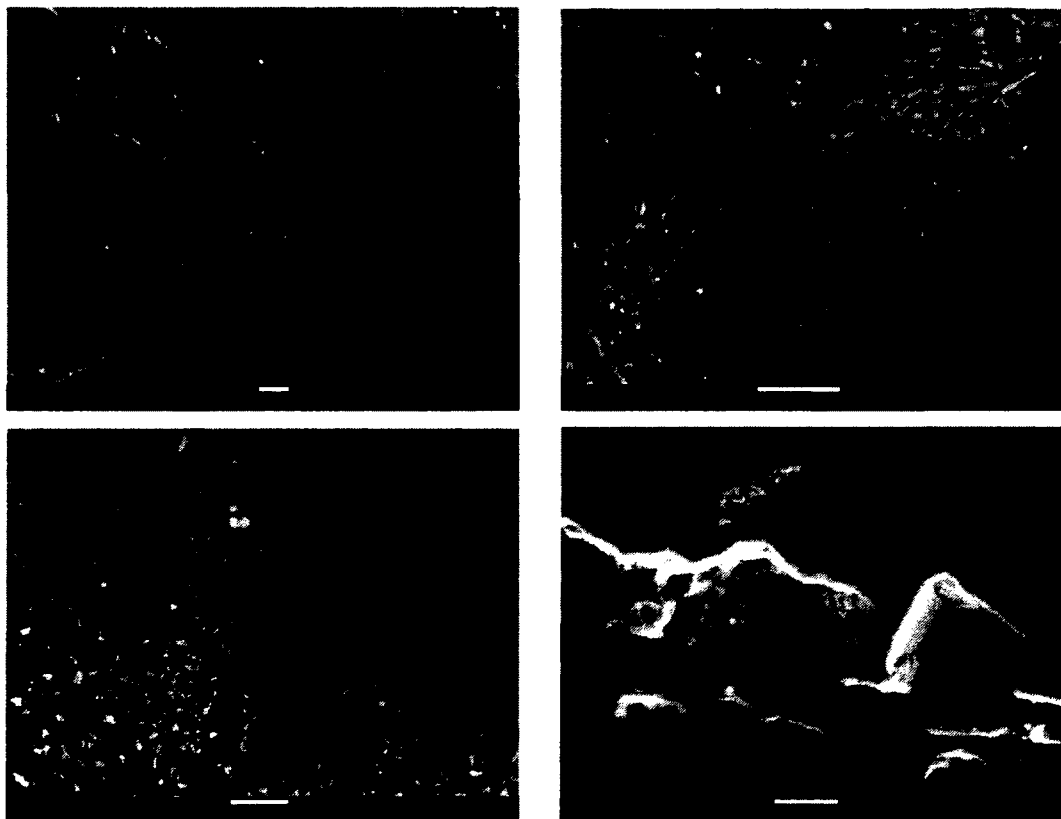


Figure 4.12: a) SEM micrograph of the test sample (subjected to 2-step ST (493-504°C/2h, 527-532°C/8h, water quenching (66°C)) and AA @ 200°C/3h) before immersion corrosion test b) X-ray microanalysis spectrum.

**Table 4.5:** X-ray microanalysis quantitative data for Fig. 4.12a)

Locations marked in Fig. 4.12a)	Weight %					
	Mg	Al	Si	Mn	Fe	Cu
1	0.00	88.75	0.24	3.29		7.72
2		70.65	0.58	14.85	1.46	12.46
3	0.00	91.11		2.64		6.26

Figure 4.13 shows the corroded regions of the 200-3 sample. Corrosion attack is not uniform along the sample circumference. In some areas, localized corrosion of the entire first layer of grains had taken place.



**Figure 4.13:** SEM micrographs of the test sample (subjected to 2-step ST (493-504°C/2h, 527-532°C/8h, water quenching (66°C)) and AA @ 200°C/3h) after immersion corrosion test.

Analysis performed near the grain boundary regions of the test sample (subjected to 2-step ST (493-504°C/2h, 527-532°C/8h, water quenching (66°C)) and AA @ 200°C/3h) show different wt% of Mn, Si and Cu. Wt% of Mg is very low near the grain boundaries and in the grains: see Table 4.6.

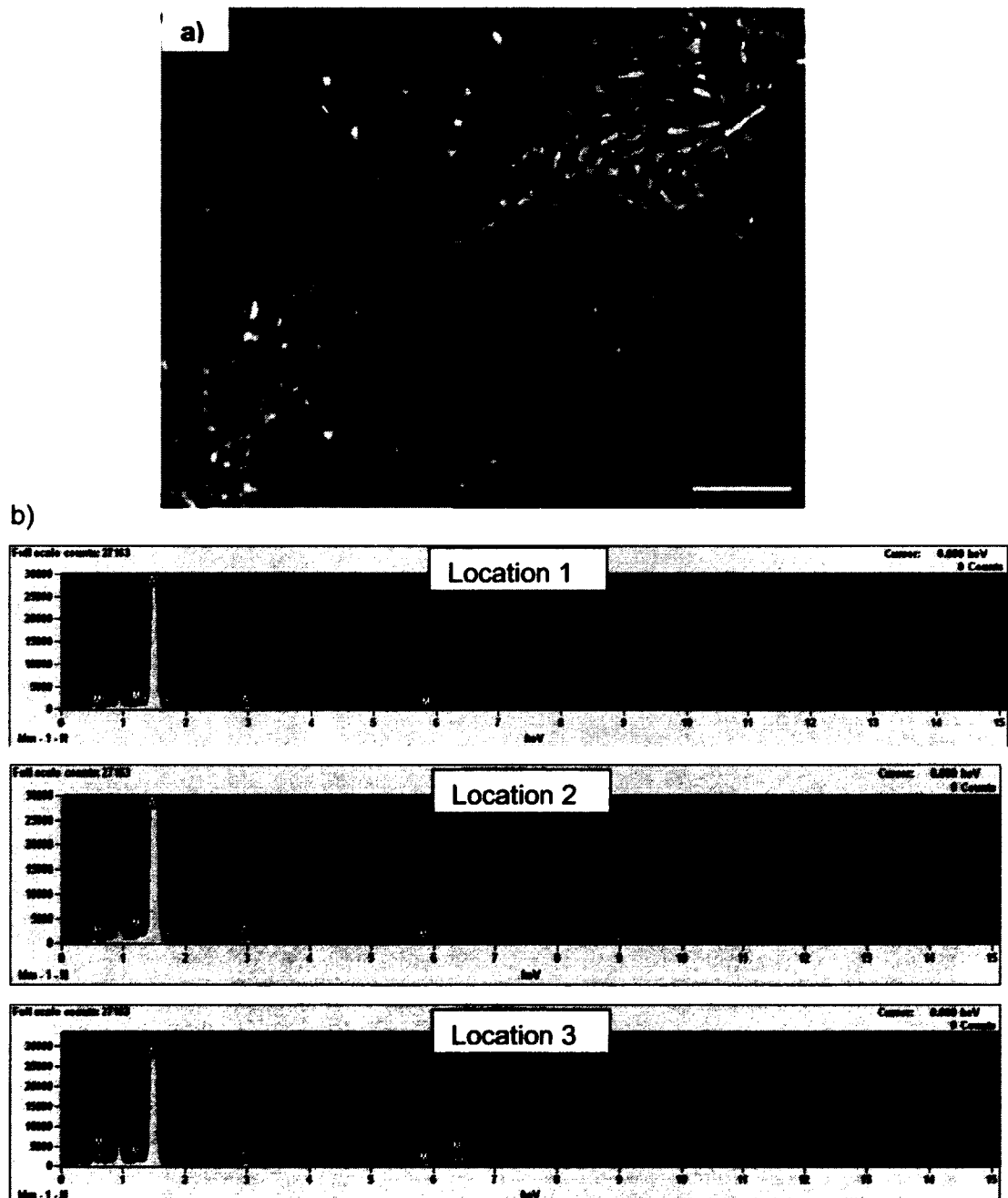


Figure 4.14: a) SEM micrograph of the test sample (subjected to 2-step ST (493-504°C/2h, 527-532°C/8h, water quenching (66°C)) and AA @ 200°C/3h) after the immersion corrosion test b) X-ray microanalysis spectrum.

**Table 4.6:** X-ray microanalysis quantitative data for Fig. 4.14a).

Locations marked in Fig. 4.14	Weight %							
	Mg	Al	Si	S	Cl	Mn	Fe	Cu
1	0.03	92.35	0.13			0.97		6.52
2	0.00	93.21	0.13			0.30		6.36
3	0.00	82.81	0.31			5.69	0.63	10.57
4	0.10	75.48		1.40	0.53	1.32		21.16

#### 4.4 Mechanical Properties analysis for second series heat treatments

Tensile test bars subjected to second series heat treatments were mechanically tested at the Nemak Engineering Centre (NEC), Windsor. The results are summarized in Figure 4.15 for UTS, Figure 4.16 for YS and Figure 4.17 for % elongation.

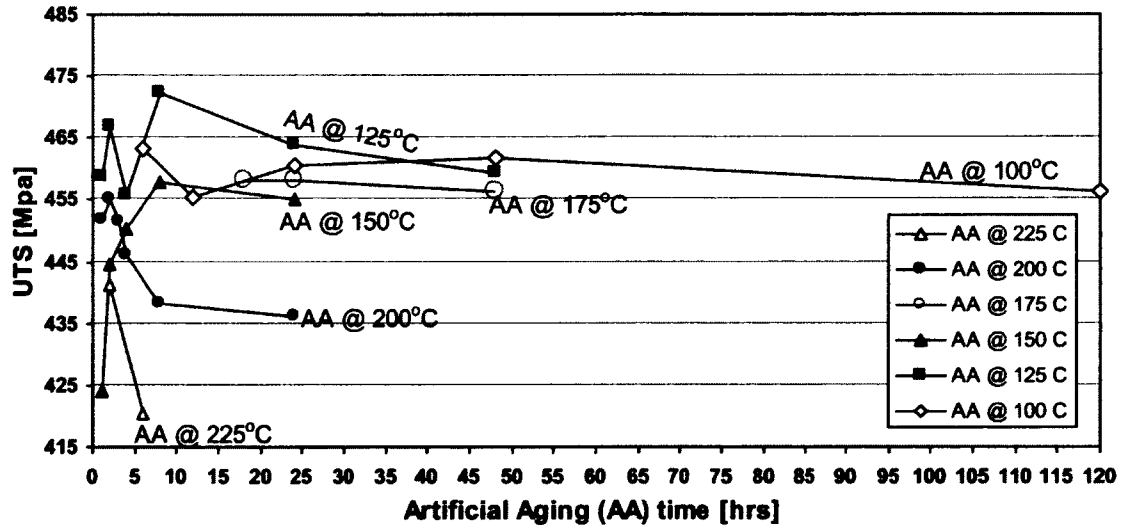


**Figure 4.15:** Effect of Artificial Aging time on the Ultimate Tensile Strength (UTS) for the second series heat treatments involving 2-step ST, NA (3 days), and 1-step AA.

It is interesting to see that the maximum UTS for all the 1-step AA treatments occur at AA time of 0 - 10 hrs. An increase in the AA temperature decreases the UTS value of B206 alloy for the second series heat treatments. UTS show no significant variation after

longer aging times. Therefore, longer AA times are not required for attaining the maximum UTS.

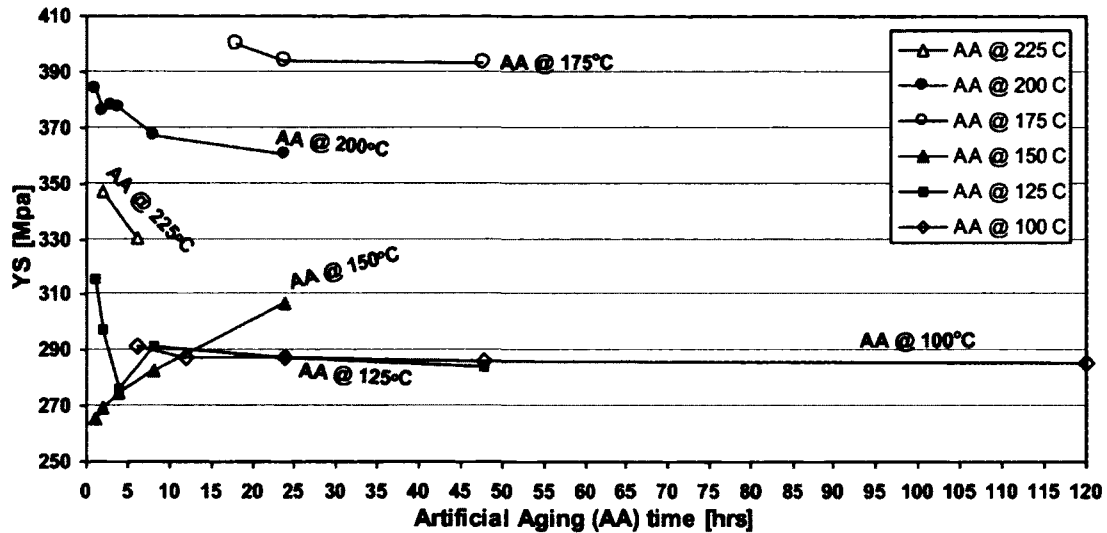


Figure 4.16: Effect of Artificial Aging time on the Yield Strength (YS) for the second series heat treatments involving 2-step ST, NA (3 days), and 1-step AA.

An increase in AA temperature from 175°C to 225°C decreases the YS from 394 MPa to 330 MPa: Fig. 4.16. Heat treatment involving 2-step ST (493-504°C/2h, 527-532°C/8h, water quenching (66°C)) and AA @ 125°C has a drop in YS till 4 hrs and then gradually becomes stable for longer aging times.

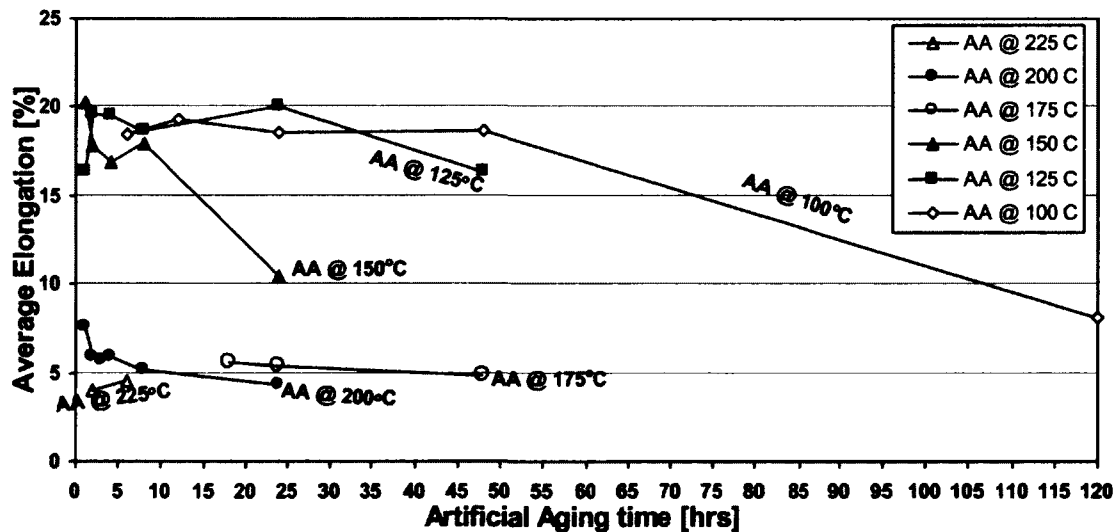


Figure 4.17: Effect of Artificial Aging time on the elongation for the second series heat treatments involving 2-step ST, NA (3 days), and 1-step AA.

As shown in Fig. 4.17, the elongation tends to decrease with longer AA times. Increase in AA temperature decreases the elongation for shorter AA times. The highest elongation was obtained for heat treatments involving 2-step (493-504°C/2h, 527-532°C/8h, water quenching (66°C)) & 1-step AA @ 125°C and 2-step (493-504°C/2h, 527-532°C/8h, water quenching (66°C)) & 1-step AA @ 150°C.

#### **4.5 Metallographic analysis for third series heat treatments**

##### **4.5.1 Heat Treatment and corrosion test data for the machined samples**

After immersion testing, machined samples subjected to 3-step Solution treatment, Natural Aging and 2-step Artificial Aging (AA) were metallographically analysed for the intergranular and pitting type corrosion. Preferential corrosion attack occurred on all test samples. The size & distribution of Cu containing intermetallic precipitates on the grain boundaries and precipitate free zones along the boundaries, castings of non-uniform chemical composition could be the reason for this preferential attack.

From Figures 4.18a and 4.18b, it can be seen that test samples 0-B-8 & 0-C-8 subjected to shorter first step AA time (0.5 hr) were susceptible to severe intergranular corrosion. Test samples (0-D-8 & 0-E-8) subjected to longer first step AA time (4 hrs) had no intergranular attack but exhibited pitting corrosion: see Figs. 4.18c and 4.18d. The natural aged samples (24-B-8, 24-C-8, 24-D-8 and 24-E-8) had both intergranular and pitting corrosion, see Fig. 4.19. In 24-C-8, the intergranular attack penetrated to the shrinkage porosity regions (Fig. 4.19b). The micrographs of the 1-step Artificially Aged samples are shown in Fig. 4.20. Table 4.7 shows the corrosion results for the machined samples.



**Table 4.7:** Summary of immersion corrosion data for the machined B206 samples:

Sample ID	Heat Treatment Conditions	Intergranular corrosion, $\mu\text{m}$		Pitting corrosion, $\mu\text{m}$	
		Approx. Max.		Approx. Max.	
		Depth	Width	Depth	Width
24-F-8	3-step ST,NA(24 hrs), AA(175°C for 12 hrs)	250	650	125	490
0-F-8	3-step ST,NA(0 hrs), AA(175°C for 12 hrs)	--	--	250	550
0-B-8	3-step ST,NA(0 hrs), AA(190°C for 0.5 hr, (water) 50°C for 1 hr, 130°C for 20 hrs)	300	750	100	100
0-C-8	3-step ST,NA(0 hrs), AA(190°C for 0.5 hr, (water) 50°C for 1 hr, 130°C for 30 hrs)	500	820	50	450
0-D-8	3-step ST,NA(0 hrs), AA(190°C for 4 hrs, (water) 50°C for 1 hr, 130°C for 20 hrs)	--	--	120	880
0-E-8	3-step ST,NA(0 hrs), AA(190°C for 4 hrs, (water) 50°C for 1 hr, 130°C for 30 hrs)	--	--	220	720
24-B-8	3-step ST,NA(24 hrs), AA(190°C for 0.5 hr, (water) 50°C for 1 hr, 130°C for 20 hrs)	375	700	125	120
24-C-8	3-step ST,NA(24 hrs), AA(190°C for 0.5 hr, (water) 50°C for 1 hr, 130°C for 30 hrs)	400	700	125	120
24-D-8	3-step ST,NA(24 hrs), AA(190°C for 4 hrs, (water) 50°C for 1 hr, 130°C for 20 hrs)	250	520	200	220
24-E-8	3-step ST,NA(24 hrs), AA(190°C for 4 hrs, (water) 50°C for 1 hr, 130°C for 30 hrs)	220	400	100	300

Note: Symbol "--" indicates the absence of intergranular and/or pitting corrosion.

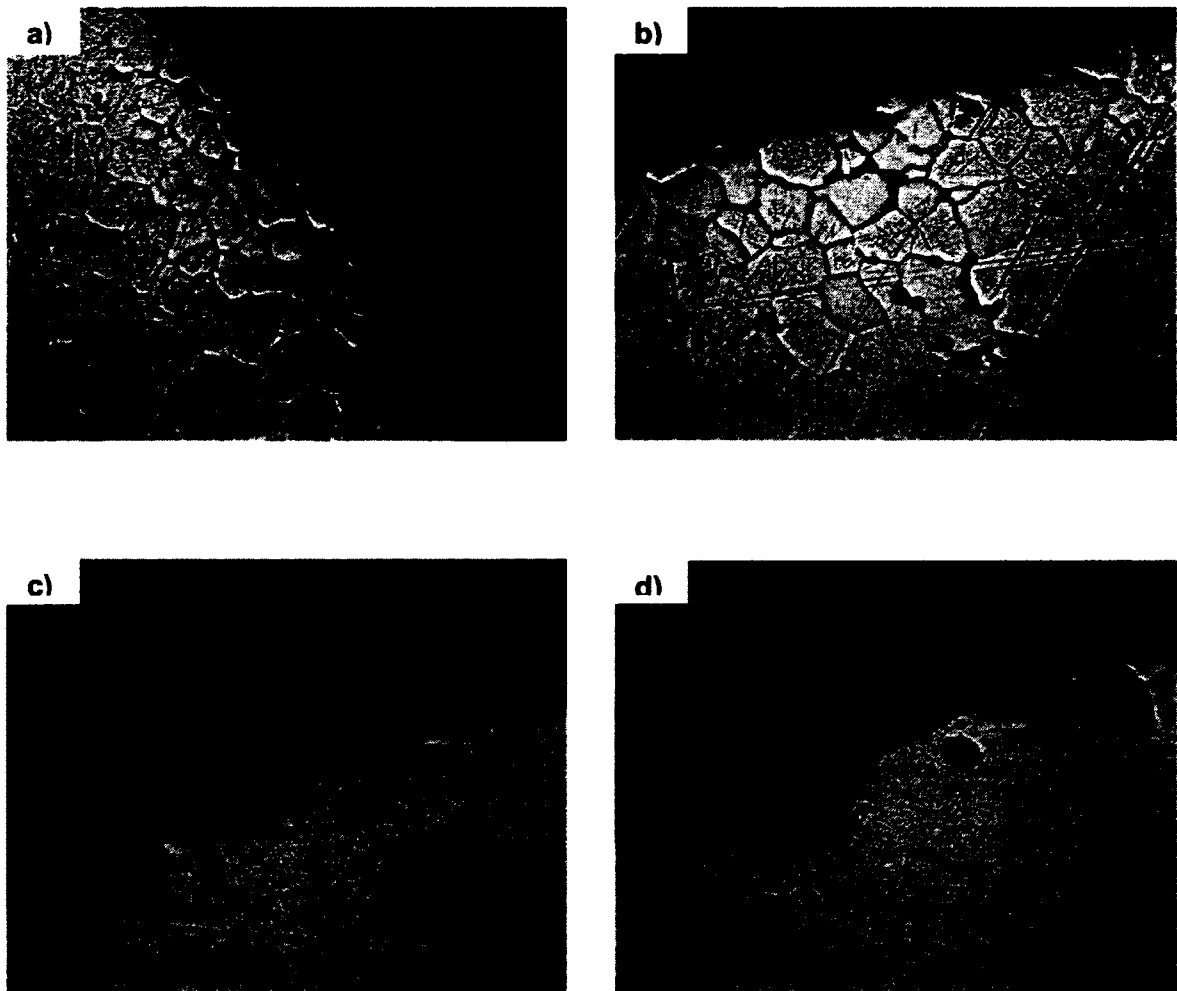


Figure 4.18: LOM Micrographs:

- a) 0-B-8: 3-step ST(515°C/3h,530°C/8h, 535°C/4h, water quenching (66°C)), 2-step AA @ (190°C/0.5h, 50°C/1h (water quenching), 130°C/20h).
- b) 0-C-8: 3-step ST(515°C/3h,530°C/8h, 535°C/4h, water quenching (66°C)), 2-step AA @ (190°C/0.5h, 50°C/1h (water quenching), 130°C/30h).
- c) 0-D-8: 3-step ST(515°C/3h,530°C/8h, 535°C/4h, water quenching (66°C)), 2-step AA @ (190°C/4h, 50°C/1h (water quenching), 130°C/20h).
- d) 0-E-8: 3-step ST(515°C/3h,530°C/8h, 535°C/4h, water quenching (66°C)), 2-step AA @ (190°C/4h, 50°C/1h (water quenching), 130°C/30h).

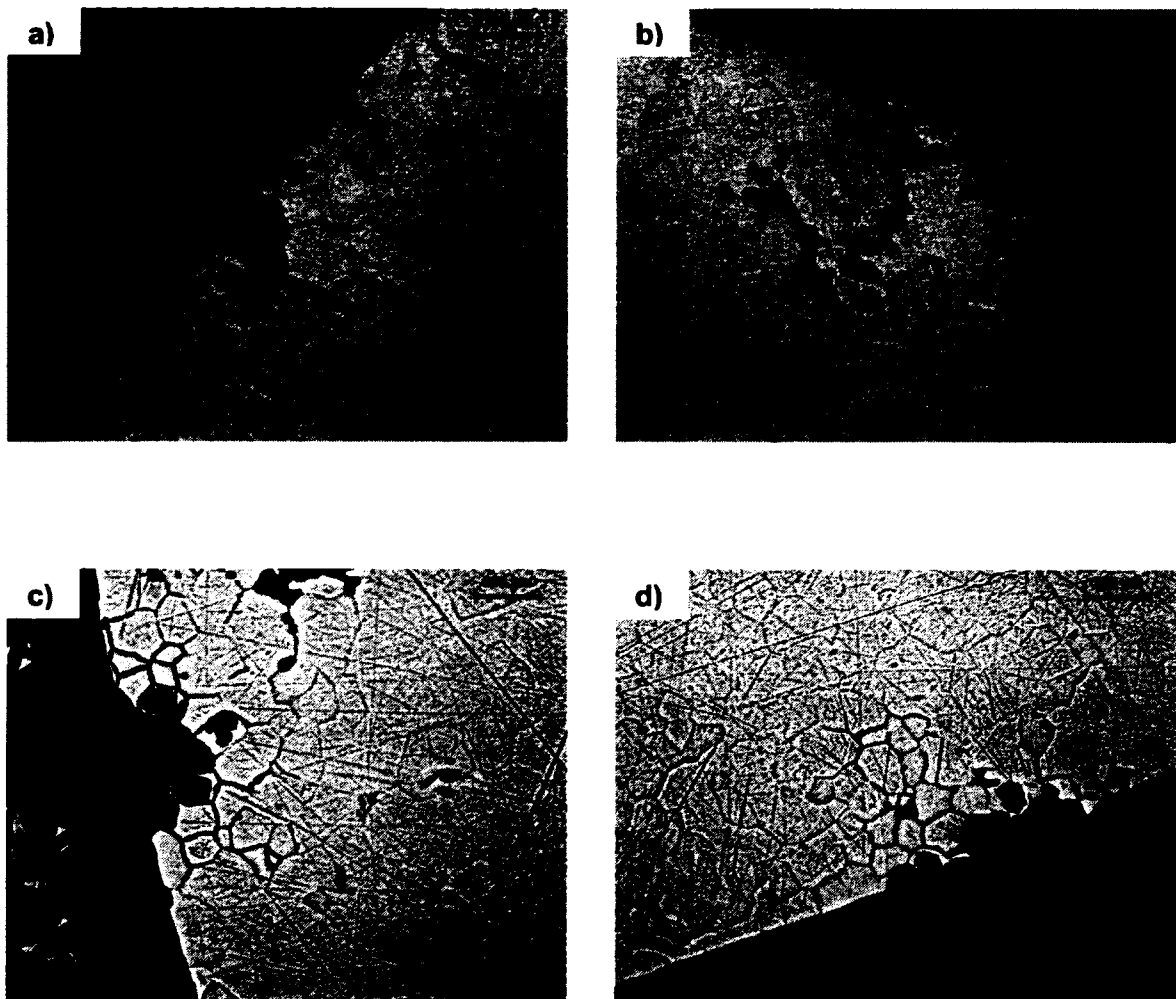


Figure 4.19: LOM Micrographs:

a) 24-B-8 : 3-step ST(515°C/3h,530°C/8h, 535°C/4h, water quenching (66°C)), 24h NA, 2-step AA @ (190°C/0.5h, 50°C/1h (water quenching), 130°C/20h).

b) 24-C-8 : 3-step ST(515°C/3h,530°C/8h, 535°C/4h, water quenching (66°C)), 24h NA, 2-step AA @ (190°C/0.5h, 50°C/1h (water quenching), 130°C/30h).

c) 24-D-8 : 3-step ST(515°C/3h,530°C/8h, 535°C/4h, water quenching (66°C)), 24h NA, 2-step AA @ (190°C/4h, 50°C/1h (water quenching), 130°C/20h).

d) 24-E-8 : 3-step ST(515°C/3h,530°C/8h, 535°C/4h, water quenching (66°C)), 24h NA, 2-step AA @ (190°C/4h, 50°C/1h (water quenching), 130°C/30h).

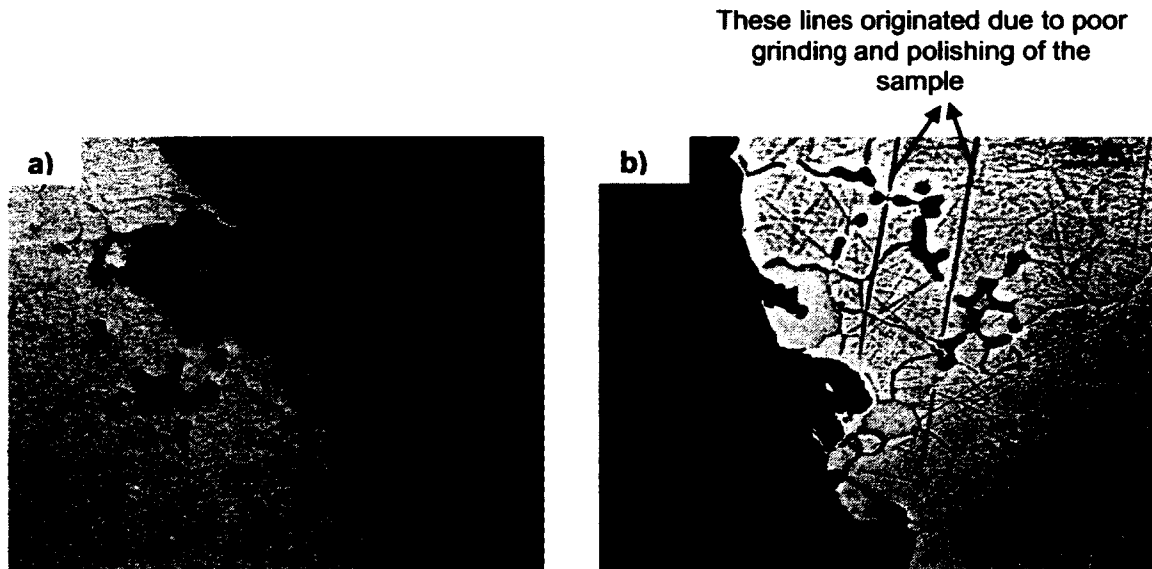


Figure 4.20: LOM Micrographs:

- a) 0-F-8: 3-step ST (515°C/3h, 530°C/8h, 535°C/4h, water quenching (66°C)), 1-step AA @ (175°C/12h).
- b) 24-F-8: 3-step ST (515°C/3h, 530°C/8h, 535°C/4h, water quenching (66°C)), 24h NA, 1-step AA @ (175°C/12h)

#### 4.5.2 Heat Treatment and corrosion test data for the non machined samples

All the non machined samples were also subjected to the same third series heat treatment conditions (section 3.5, 3-step ST & 2-step AA) as the machined samples. Therefore, the sample ID for non machined samples are marked with \* (for ex. 24-F-8\* instead of 24-F-8).

Intergranular and pitting corrosion depths and widths were metallographically determined for the non machined samples. Table 4.8 summarizes the corrosion data for non machined samples.

**Table 4.8:** Summary of corrosion data for the non machined B206 samples:

Sample ID	Heat Treatment Conditions	Intergranular corrosion, $\mu\text{m}$		Pitting corrosion, $\mu\text{m}$	
		Approx. Max.		Approx. Max.	
		Depth	Width	Depth	Width
24-F-8*	3-step ST,NA(24 hrs), AA(175°C for 12 hrs)	380	700	130	350
0-F-8*	3-step ST,NA(0 hrs), AA(175°C for 12 hrs)	--	--	200	300
0-B-8*	3-step ST,NA(0 hrs), AA(190°C for 0.5 hr, (water) 50°C for 1 hr, 130°C for 20 hrs)	230	700	90	100
0-C-8*	3-step ST,NA(0 hrs), AA(190°C for 0.5 hr, (water) 50°C for 1 hr, 130°C for 30 hrs)	400	750	130	200
0-D-8*	3-step ST,NA(0 hrs), AA(190°C for 4 hrs, (water) 50°C for 1 hr, 130°C for 20 hrs)	--	--	170	330
0-E-8*	3-step ST,NA(0 hrs), AA(190°C for 4 hrs, (water) 50°C for 1 hr, 130°C for 30 hrs)	--	--	360	700
24-B-8*	3-step ST,NA(24 hrs), AA(190°C for 0.5 hr, (water) 50°C for 1 hr, 130°C for 20 hrs)	300	850	70	300
24-C-8*	3-step ST,NA(24 hrs), AA(190°C for 0.5 hr, (water) 50°C for 1 hr, 130°C for 30 hrs)	300	450	--	--
24-D-8*	3-step ST,NA(24 hrs), AA(190°C for 4 hrs, (water) 50°C for 1 hr, 130°C for 20 hrs)	250	300	100	200
24-E-8*	3-step ST,NA(24 hrs), AA(190°C for 4 hrs, (water) 50°C for 1 hr, 130°C for 30 hrs)	350	450	200	650

Note: Symbol "--" means the absence of intergranular and/or pitting corrosion.

Intergranular corrosion was more detrimental in test samples 24-F-8\*, 24-E-8\*, 24-B-8\*, 24-C-8\*. Test samples 0-D-8\*, 0-E-8\* and 0-F-8\* show the absence of intergranular corrosion. Heat treatments involving 2-step AA without NA renders better corrosion resistance compared to 2-step AA with NA. The pitting/intergranular corrosion depth is

very sensitive to both NA time & AA time. Test samples 0-B-8\* and 0-C-8\* (refer Fig. 4.21a) and Fig. 4.21b)) indicate an increase in the maximum intergranular corrosion depth when the second step AA time is increased from 20 to 30 hrs without changing the first step AA time (0.5 hrs). Similarly, test samples 0-D-8\* and 0-E-8\*, Figs. 4.22a) and 4.22b) show an increase in maximum pitting corrosion depth when the second step AA time is increased from 20 to 30 hrs without changing the first step AA time (4 hrs).

Longer second step aging time (30 hrs) in 24-E-8\* results in increased pitting attack compared to sample 24-D-8\* (Fig. 4.23a) and 4.23b)). Sample 24-F-8\* has both pitting and intergranular corrosion while sample 0-F-8\* has pitting corrosion only (Figs. 4.23c) and 4.23d)). There is no NA treatment in 0-F-8\* resulting in the absence of intergranular corrosion.

The type and nature of corrosion attack obtained from the non machined test samples are similar to the machined test samples. Shorter first step AA time (0.5 hr) results in severe intergranular corrosion for both machined and non machined test samples. Machined samples 0-D-8, 0-E-8, 0-F-8 and non machined samples 0-D-8\*, 0-E-8\*, 0-F-8\* had pitting corrosion only.

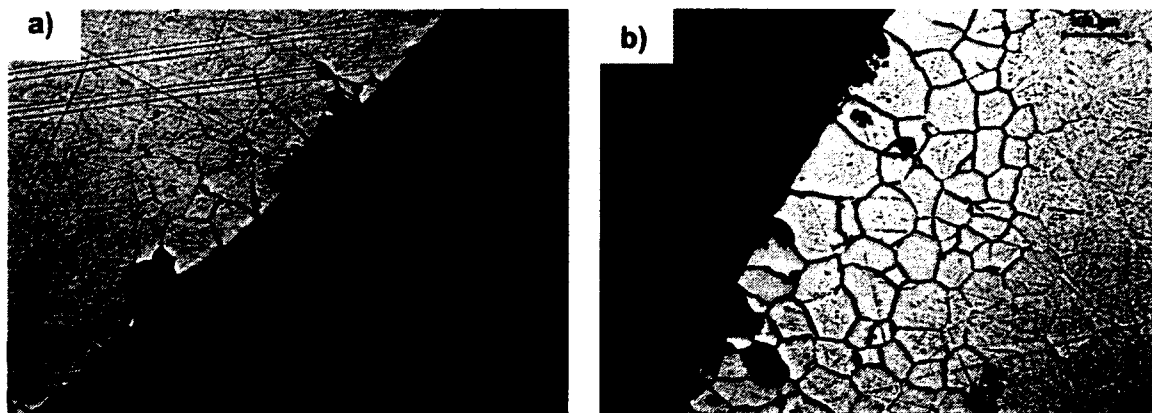


Figure 4.21: LOM Micrographs:

a) 0-B-8\*: 3-step ST (515°C/3h, 530°C/8, 535°C/4h, water quenching (66°C)), 2-step AA @ (190°C/0.5h, 50°C/1h (water quenching), 130°C/20h).

b) 0-C-8\*: 3-step ST (515°C/3h, 530°C/8, 535°C/4h, water quenching (66°C)), 2-step AA @ (190°C/0.5h, 50°C/1h (water quenching), 130°C/30h).

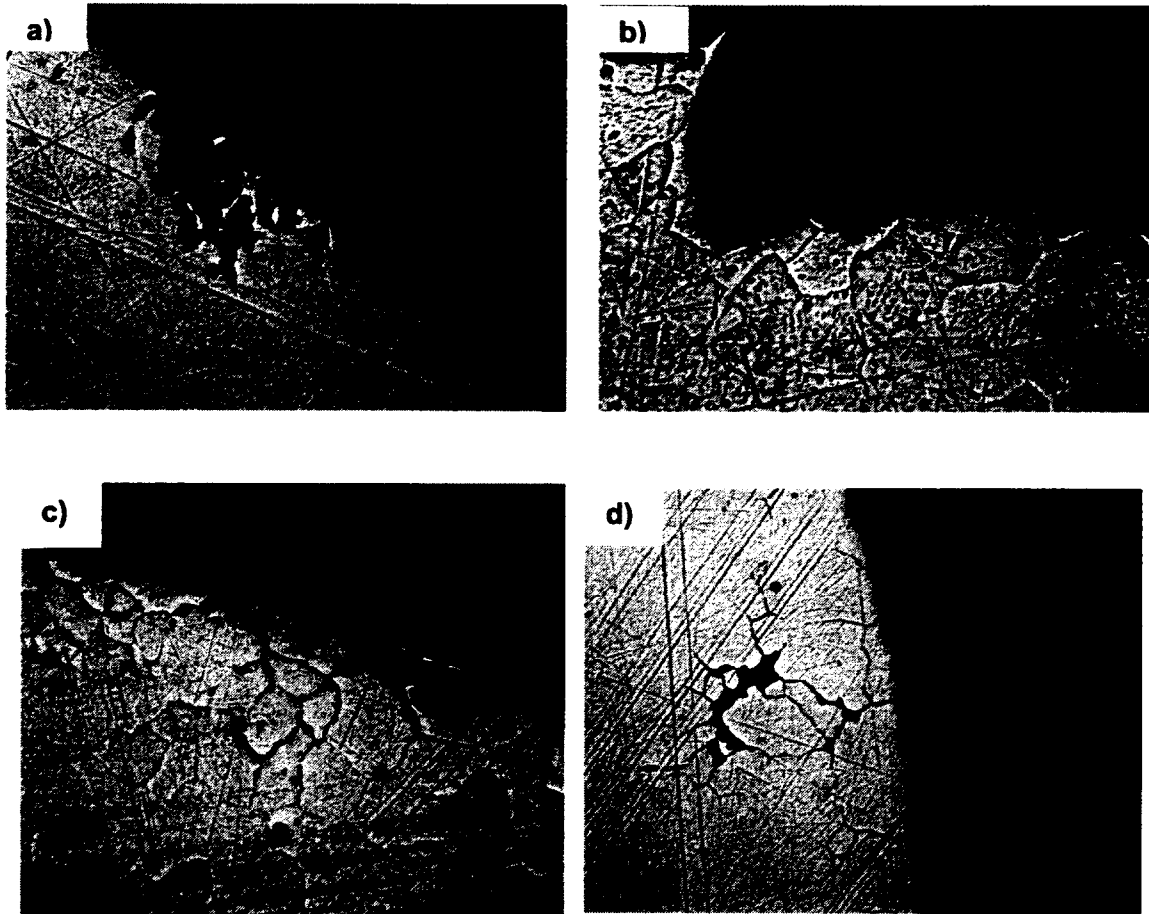


Figure 4.22: LOM Micrographs:

a) 0-D-8\*: 3-step ST (515°C/3h, 530°C/8, 535°C/4h, water quenching (66°C)), 2-step AA @ (190°C/4h, 50°C/1h (water quenching), 130°C/20h).

b) 0-E-8\*: 3-step ST (515°C/3h, 530°C/8, 535°C/4h, water quenching (66°C)), 2-step AA @ (190°C/4h, 50°C/1h (water quenching), 130°C/30h).

c) 24-B-8\*: 3-step ST (515°C/3h, 530°C/8h, 535°C/4h, water quenching (66°C)), 24h NA, 2-step AA @ (190°C/0.5h, 50°C/1h (water quenching), 130°C/20h).

d) 24-C-8\*: 3-step ST (515°C/3h, 530°C/8h, 535°C/4h, water quenching (66°C)), 24h NA, 2-step AA @ (190°C/0.5h, 50°C/1h (water quenching), 130°C/30h).

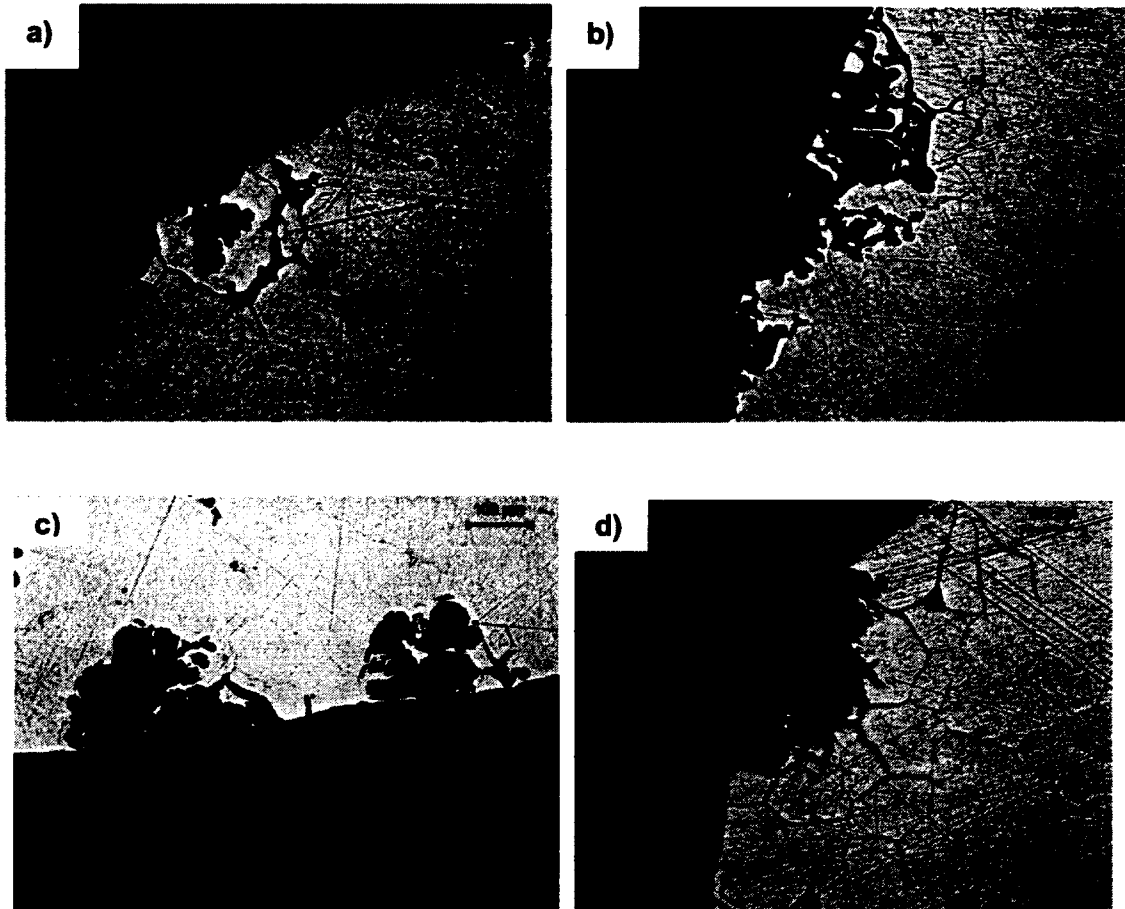


Figure 4.23: LOM Micrographs:

a) 24-D-8\*: 3-step ST (515°C/3h, 530°C/8h, 535°C/4h, water quenching (66°C)), 24h NA, 2-step AA @ (190°C/4h, 50°C/1h (water quenching), 130°C/20h).

b) 24-E-8\*: 3-step ST (515°C/3h, 530°C/8h, 535°C/4h, water quenching (66°C)), 24h NA, 2-step AA @ (190°C/4h, 50°C/1h (water quenching), 130°C/30h).

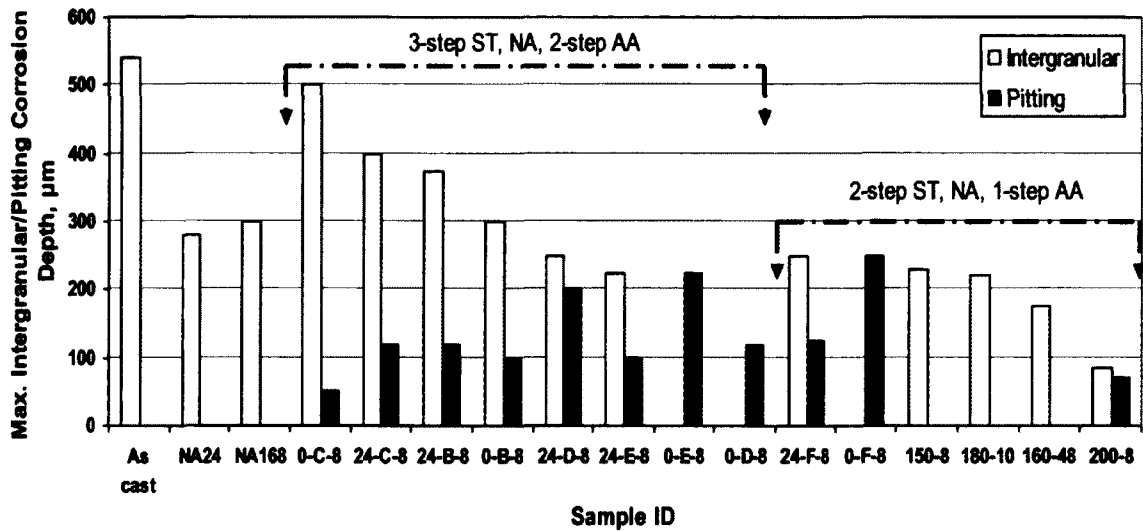
c) 0-F-8\*: 3-step ST (515°C/3h, 530°C/8h, 535°C/4h, water quenching (66°C)), 1-step AA @ (175°C/12h).

d) 24-F-8\*: 3-step ST (515°C/3h, 530°C/8h, 535°C/4h, water quenching (66°C)), 24h NA, 1-step AA @ (175°C/12h).



#### 4.6 Comparison of immersion corrosion behaviour of heat treated samples subjected to 2 vs. 3-step ST and 1 vs. 2-step AA with and without NA

Figure 4.24 presents corrosion data for the 2 vs. 3-step ST, NA (0 & 24 hrs) and one vs. two step Artificially Aged machined samples.



NA24: Two step ST, Natural Aging for 24 hrs

NA168: Two step ST, Natural Aging for 168 hrs

0-C-8: Three Step ST, AA (190°C for 0.5 hr, (water) 50°C for 1 hr, 130°C for 30 hrs)

24-C-8: Three Step ST, NA (24 hrs), AA (190°C for 0.5 hr, (water) 50°C for 1 hr, 130°C for 30 hrs)

24-B-8: Three Step ST, NA (24 hrs), AA (190°C for 0.5 hr, (water) 50°C for 1 hr, 130°C for 20 hrs)

0-B-8: Three Step ST, AA (190°C for 0.5 hr, (water) 50°C for 1 hr, 130°C for 20 hrs)

24-D-8: Three Step ST, NA (24 hrs), AA (190°C for 4 hrs, (water) 50°C for 1 hr, 130°C for 20 hrs)

24-E-8: Three Step ST, NA (24 hrs), AA (190°C for 4 hrs, (water) 50°C for 1 hr, 130°C for 30 hrs)

0-E-8: Three Step ST, AA (190°C for 4 hrs, (water) 50°C for 1 hr, 130°C for 30 hrs)

0-D-8: Three Step ST, AA (190°C for 4 hrs, (water) 50°C for 1 hr, 130°C for 20 hrs)

24-F-8: Three Step ST, NA (24 hrs), AA (175°C for 12 hrs)

0-F-8: Three Step ST, AA (175°C for 12 hrs)

150-8: Two Step ST, AA (150°C for 8 hrs)

180-10: Two Step ST, NA (24 hrs), AA (180°C for 10 hrs)

160-24: Two Step ST, NA (24 hrs), AA (160°C for 24 hrs)

200-8: Two Step ST, AA (200°C for 8 hrs)

Figure 4.24: Corrosion Depth for the machined samples heat treated using ST (2-step & 3-step), NA (0 & 24 hrs) and AA (1-step & 2-step) conditions.

Test samples 0-D-8, 0-E-8 and 0-F-8 clearly show that third series heat treatments eliminate intergranular corrosion. Test samples subjected to 3-step ST and NA prior to one step & two step AA has poor intergranular corrosion resistance. Samples 150-8, 160-24, 180-10 and 200-8 come from the first series heat treatments. Sample 200-8

subjected to 2-step ST (493-504°C/2h, 527-532°C/8h, water quenching (66°C)) & AA @ 200°C/8h exhibit good corrosion resistance in the first series heat treatment experiments.

#### 4.7 Analysis of mechanical properties for third series heat treatments

B206 tensile test bars subjected to third series heat treatments (section 3.5, 3-step ST and 2-step AA conditions) were mechanically tested. The number of mechanical test samples for each heat treatment batch was 7. Table 4.9 summarizes the mechanical properties (Ultimate Tensile Strength (UTS), Yield Strength (YS), and Elongation (%)).

**Table 4.9:** Summary of mechanical properties for third series heat treated B206 alloy.

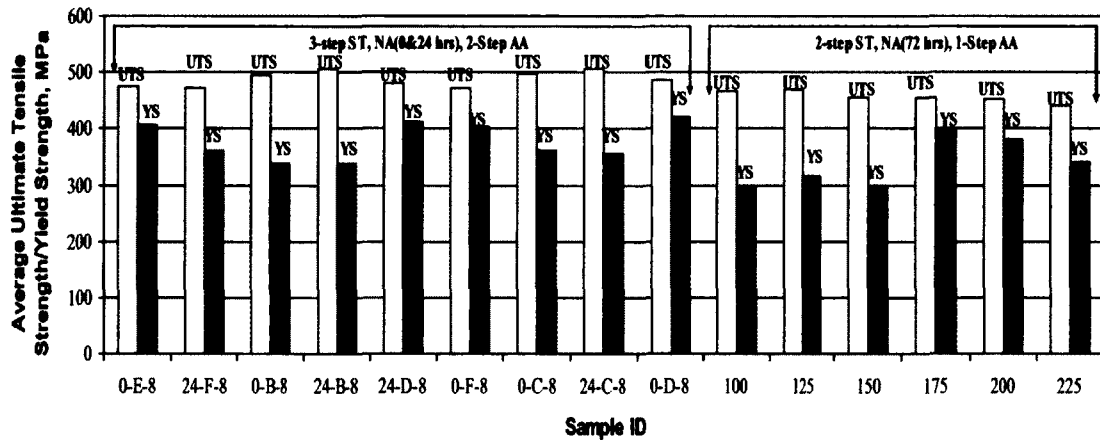
Sample ID	Average Ultimate Tensile Strength (UTS), MPa	Average Yield Strength (YS), MPa	Average Elongation (%)	Standard Deviation for UTS, MPa	Standard Deviation for YS, MPa	Standard Deviation for Elongation (%)
24-F-8	473.04	360.28	7.28	10.38	90.64	2.77
0-F-8	472.37	402.57	6.45	4.47	3.04	1.09
0-B-8	493.66	339.21	12.05	3.91	9.37	3.22
0-C-8	496.66	361.75	9.59	9.05	5.67	1.78
0-D-8	487.18	421.27	6.19	7.26	7.03	1.68
0-E-8	473.97	407.91	6.64	18.14	14.7	2.35
24-B-8#	506.9#	338.87#	14.28#	--	--	--
24-C-8	505.78	356.5	13.19	8.81	9.23	1.76
24-D-8	481.43	411.8	7.33	7.72	5.84	1.82

Note: The symbol “#” indicates that only one sample was tested.

24-B-8 and 24-C-8 exhibit the highest UTS of the samples. Sample 0-D-8 has the highest YS and lowest elongation in the third series heat treatments. Samples 0-B-8, 0-C-8, 24-B-8 & 24-C-8 met the ( $\geq 10\%$ ) elongation requirements. Samples subjected to NA + AA exhibit higher elongations than samples with only AA.

#### 4.7.1 Comparison of UTS, YS for 3-step ST, NA (0 & 24 hrs), 2-step AA and 2-step ST, NA (72 hrs), 1-step AA

Figure 4.25 presents the average Ultimate Tensile Strength (UTS) and Yield Strength (YS) data for both the 3-step ST & 2-step AA and 2-step ST & 1-step AA heat treatments.



- 0-E-8: Three step ST, AA (190°C for 4 hrs, (water) 50°C for 1 hr, 130°C for 30 hrs)
- 24-F-8: Three step ST, NA (24 hrs), AA (175°C for 12 hrs)
- 0-B-8: Three step ST, AA (190°C for 0.5 hr, (water) 50°C for 1 hr, 130°C for 20 hrs)
- 24-B-8: Three step ST, NA (24 hrs), AA (190°C for 0.5 hr, (water) 50°C for 1 hr, 130°C for 20 hrs)
- 24-D-8: Three step ST, NA (24 hrs), AA (190°C for 4 hrs, (water) 50°C for 1 hr, 130°C for 20 hrs)
- 0-F-8: Three step ST, AA (175°C for 12 hrs)
- 0-C-8: Three step ST, AA (190°C for 0.5 hr, (water) 50°C for 1 hr, 130°C for 30 hrs)
- 24-C-8: Three step ST, NA (24 hrs), AA (190°C for 0.5 hr, (water) 50°C for 1 hr, 130°C for 30 hrs)
- 0-D-8: Three step ST, AA (190°C for 4 hrs, (water) 50°C for 1 hr, 130°C for 20 hrs)
- 100: Two step ST, NA (72 hrs), AA at (100°C for 48 hrs)
- 125: Two step ST, NA (72 hrs), AA (125°C for 48 hrs)
- 150: Two step ST, NA (72 hrs), AA (150°C for 8 hrs)
- 175: Two step ST, NA (72 hrs), AA (175°C for 24 hrs)
- 200: Two step ST, NA (72 hrs), AA (200°C for 1 hr)
- 225: Two step ST, NA (72 hrs), AA (225°C for 2 hrs)

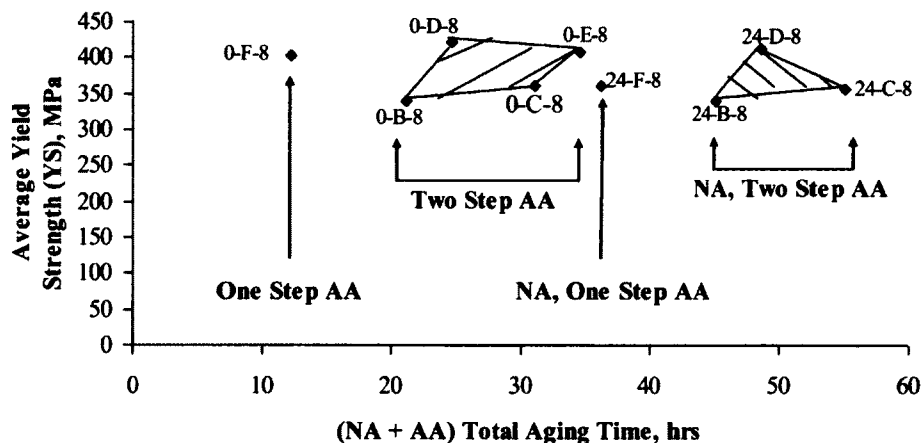
Figure 4.25: Comparison of the average UTS and YS for 3-step ST, NA (0 & 24 hrs), two step AA conditions and 2-step ST, NA (72 hrs), one step AA conditions.

Improvement in UTS and YS can be observed in the samples subjected to a 3-step ST and 2-step AA (Figure 4.25). The increase in tensile properties is attributed to aging at an elevated temperature followed by low temperature water quench (50°C/1 hr) and then aging again at an elevated temperature [76]. Some of the second series heat treatments are as good as the third series heat treatments. UTS and YS obtained under the 2-step

ST and one step AA conditions were in the range of 420 to 470 MPa and 250 to 400 MPa respectively. UTS and YS obtained under the 3-step ST and 2-step AA conditions were in the range of 472 to 506 MPa and 338 to 421 MPa.

#### 4.7.2 Effect of total aging (NA and AA) time on YS and elongation for third series heat treatments

Figure 4.26 illustrates the effect of total (NA & AA) aging time on the YS for 3-step ST, NA (0 & 24 hrs) + one and two step AA. Test samples 0-D-8 and 0-E-8 subjected to a longer first step AA time (4 hrs) have higher YS compared to test samples 0-B-8 and 0-C-8. Similarly, test sample 24-D-8 subjected to a longer first step AA time (4 hrs) had higher YS compared to test samples 24-B-8 and 24-C-8.



0-F-8: Three step ST, AA (175°C for 12 hrs)

0-B-8: Three step ST, AA (190°C for 0.5 hr, (water) 50°C for 1 hr, 130°C for 20 hrs)

0-C-8: Three step ST, AA (190°C for 0.5 hr, (water) 50°C for 1 hr, 130°C for 30 hrs)

0-D-8: Three step ST, AA (190°C for 4 hrs, (water) 50°C for 1 hr, 130°C for 20 hrs)

0-E-8: Three step ST, AA (190°C for 4 hrs, (water) 50°C for 1 hr, 130°C for 30 hrs)

24-F-8: Three step ST, NA (24 hrs), AA (175°C for 12 hrs)

24-B-8: Three step ST, NA (24 hrs), AA (190°C for 0.5 hr, (water) 50°C for 1 hr, 130°C for 20 hrs)

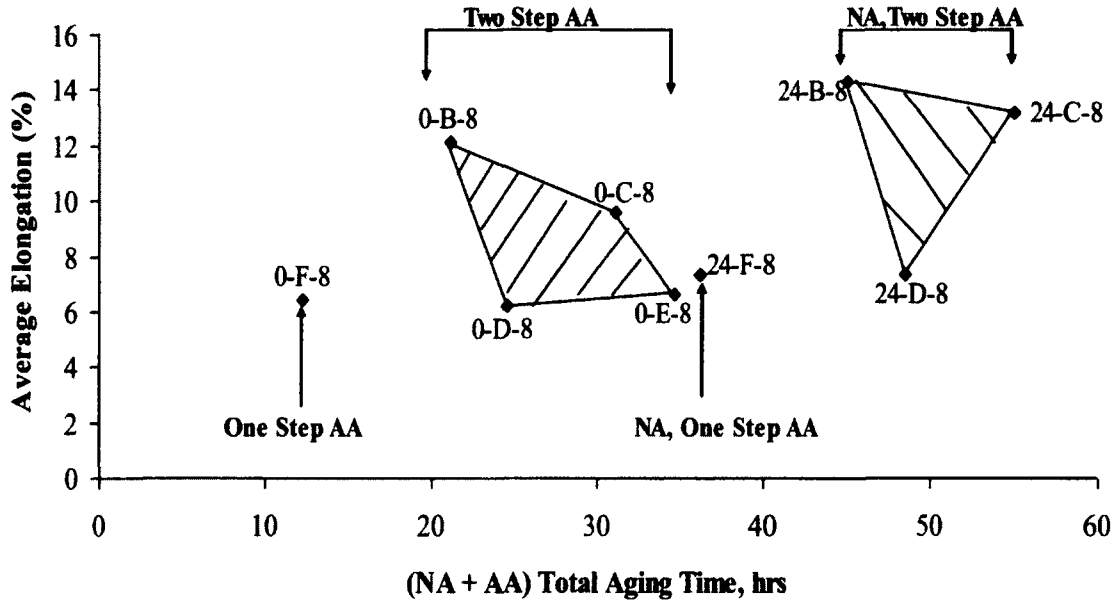
24-D-8: Three step ST, NA (24 hrs), AA (190°C for 4 hrs, (water) 50°C for 1 hr, 130°C for 20 hrs)

24-C-8: Three step ST, NA (24 hrs), AA (190°C for 0.5 hr, (water) 50°C for 1 hr, 130°C for 30 hrs)

Figure 4.26: Average Yield Strength (YS), MPa vs. (NA & AA) Total Aging Time, hrs for third series heat treatments.

Figure 4.27 illustrates the effect of total (NA & AA) aging time on elongation for 3-step ST, NA (0 & 24 hrs) + one and two step AA. Test samples 0-B-8 and 0-C-8 show a higher elongation (Figure 4.27) than test samples 0-D-8 and 0-E-8. This could be due to

the shorter first step AA time (0.5 hr) in 0-B-8 and 0-C-8. Test samples subjected to NA prior to 2-step AA exhibited higher elongation values. Test samples 24-B-8 and 24-C-8 show a higher elongation compared to test sample 24-D-8.



0-F-8: Three step ST, AA (175°C for 12 hrs)

0-B-8: Three step ST, AA (190°C for 0.5 hr, (water) 50°C for 1 hr, 130°C for 20 hrs)

0-C-8: Three step ST, AA (190°C for 0.5 hr, (water) 50°C for 1 hr, 130°C for 30 hrs)

0-D-8: Three step ST, AA (190°C for 4 hrs, (water) 50°C for 1 hr, 130°C for 20 hrs)

0-E-8: Three step ST, AA (190°C for 4 hrs, (water) 50°C for 1 hr, 130°C for 30 hrs)

24-F-8: Three step ST, NA (24 hrs), AA (175°C for 12 hrs)

24-B-8: Three step ST, NA (24 hrs), AA (190°C for 0.5 hr, (water) 50°C for 1 hr, 130°C for 20 hrs)

24-D-8: Three step ST, NA (24 hrs), AA (190°C for 4 hrs, (water) 50°C for 1 hr, 130°C for 20 hrs)

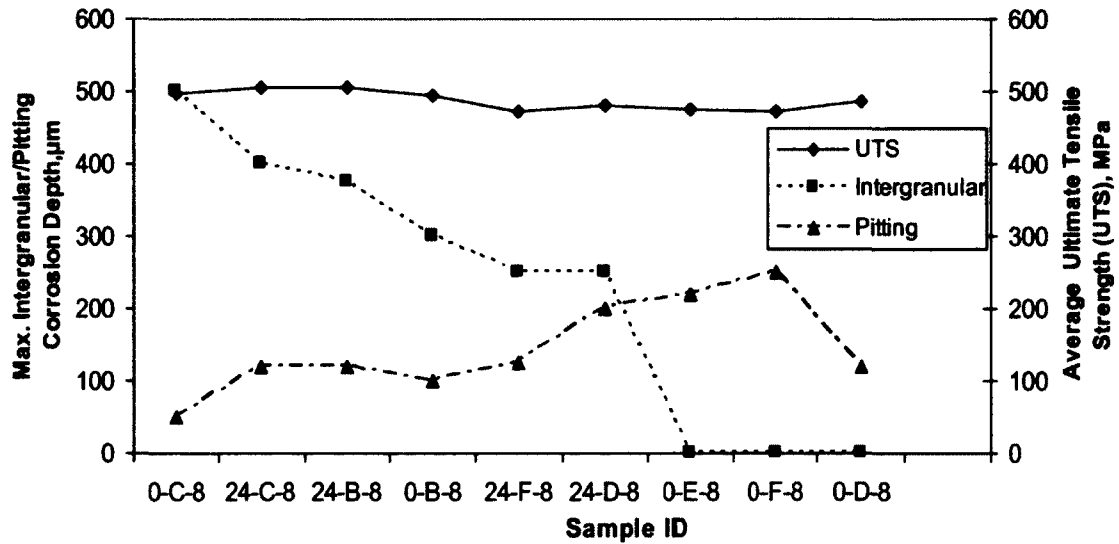
24-C-8: Three step ST, NA (24 hrs), AA (190°C for 0.5 hr, (water) 50°C for 1 hr, 130°C for 30 hrs)

Figure 4.27: Average Elongation vs. (NA & AA) Total Aging Time, hrs for one and two step AA.

#### 4.7.3 Comparison of mechanical properties and corrosion resistance for the Third Series Heat Treatment Experiments

Figure 4.28 compares the average UTS with the data for max. intergranular and pitting corrosion depths obtained in the immersion corrosion tests. The Ultimate Tensile

Strength (UTS) remains almost same for the third series heat treatments. There is no relationship between the Ultimate Tensile Strength (UTS) and the corrosion results, at least as expressed by the depths of intergranular or pitting corrosion.



**0-E-8:** Three step ST, AA (190°C for 4 hrs, (water) 50°C for 1 hr, 130°C for 30 hrs)

**24-F-8:** Three step ST, NA (24 hrs), AA (175°C for 12 hrs)

**0-B-8:** Three step ST, AA (190°C for 0.5 hr, (water) 50°C for 1 hr, 130°C for 20 hrs)

**24-B-8:** Three step ST, NA (24 hrs), AA (190°C for 0.5 hr, (water) 50°C for 1 hr, 130°C for 20 hrs)

**24-D-8:** Three step ST, NA (24 hrs), AA (190°C for 4 hrs, (water) 50°C for 1 hr, 130°C for 20 hrs)

**0-F-8:** Three step ST, AA (175°C for 12 hrs)

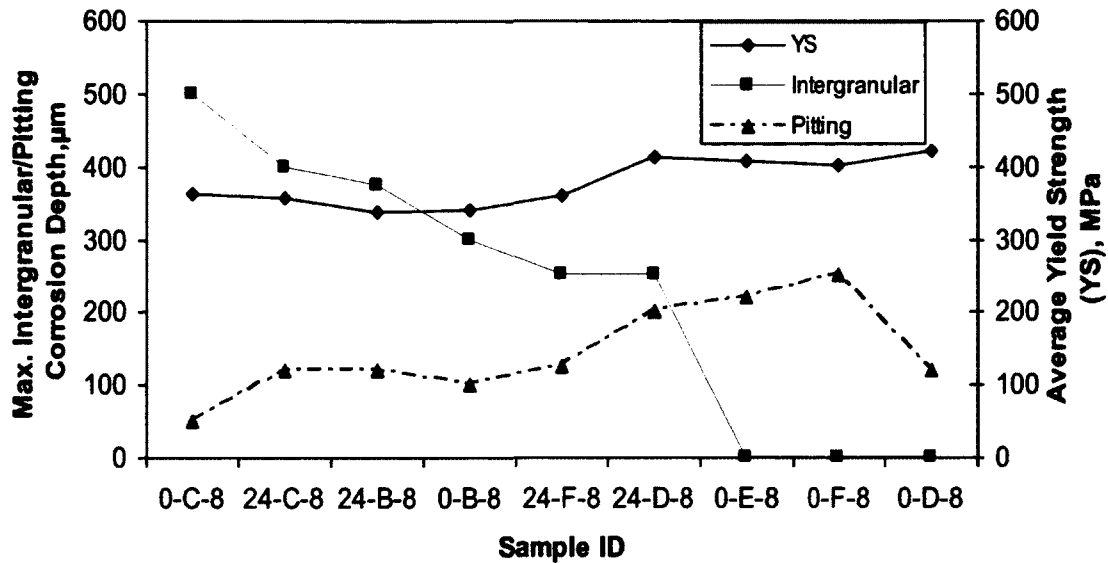
**0-C-8:** Three step ST, AA (190°C for 0.5 hr, (water) 50°C for 1 hr, 130°C for 30 hrs)

**24-C-8:** Three step ST, NA (24 hrs), AA (190°C for 0.5 hr, (water) 50°C for 1 hr, 130°C for 30 hrs)

**0-D-8:** Three step ST, AA (190°C for 4 hrs, (water) 50°C for 1 hr, 130°C for 20 hrs)

Figure 4.28: Average UTS and maximum corrosion depths for third series heat treatments.

Figure 4.29 compares the average YS and the data for maximum corrosion depths (intergranular & pitting).



0-E-8: Three step ST, AA (190°C for 4 hrs, (water) 50°C for 1 hr, 130°C for 30 hrs)

24-F-8: Three step ST, NA (24 hrs), AA (175°C for 12 hrs)

0-B-8: Three step ST, AA (190°C for 0.5 hr, (water) 50°C for 1 hr, 130°C for 20 hrs)

24-B-8: Three step ST, NA (24 hrs), AA (190°C for 0.5 hr, (water) 50°C for 1 hr, 130°C for 20 hrs)

24-D-8: Three step ST, NA (24 hrs), AA (190°C for 4 hrs, (water) 50°C for 1 hr, 130°C for 20 hrs)

0-F-8: Three step ST, AA (175°C for 12 hrs)

0-C-8: Three step ST, AA (190°C for 0.5 hr, (water) 50°C for 1 hr, 130°C for 30 hrs)

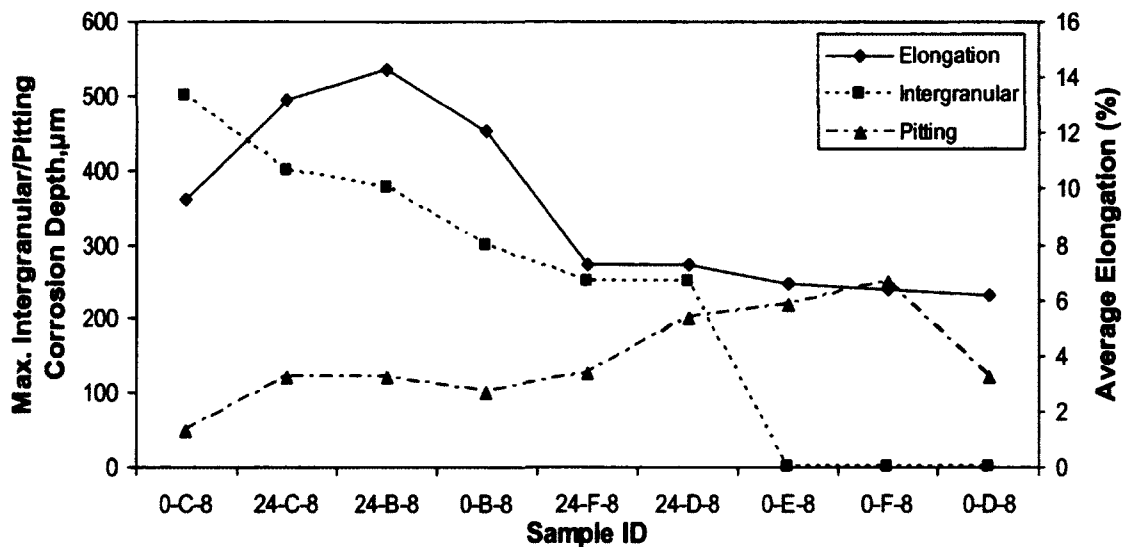
24-C-8: Three step ST, NA (24 hrs), AA (190°C for 0.5 hr, (water) 50°C for 1 hr, 130°C for 30 hrs)

0-D-8: Three step ST, AA (190°C for 4 hrs, (water) 50°C for 1 hr, 130°C for 20 hrs)

Figure 4.29: Average YS and maximum corrosion depths for third series heat treatments.

Specimens subjected to the tensile testing are not used for its corrosion testing. The average YS for the third series heat treatments vary from 338 to 421 MPa. Test sample 0-D-8 with the best corrosion resistance (no intergranular corrosion and one of the lowest depths of pitting corrosion) had the highest average YS of 421 MPa. Test sample 0-C-8 with the lowest intergranular corrosion resistance had average YS of only 361.75 MPa.

Figure 4.30 compares the average elongation and the data for maximum corrosion depths (intergranular & pitting).



24-B-8: Three step ST, NA (24 hrs), AA (190°C for 0.5 hr, (water) 50°C for 1 hr, 130°C for 20 hrs)

24-C-8: Three step ST, NA (24 hrs), AA (190°C for 0.5 hr, (water) 50°C for 1 hr, 130°C for 30 hrs)

0-B-8: Three step ST, AA (190°C for 0.5 hr, (water) 50°C for 1 hr, 130°C for 20 hrs)

0-C-8: Three step ST, AA (190°C for 0.5 hr, (water) 50°C for 1 hr, 130°C for 30 hrs)

24-D-8: Three step ST, NA (24 hrs), AA (190°C for 4 hrs, (water) 50°C for 1 hr, 130°C for 20 hrs)

24-F-8: Three step ST, NA (24 hrs), AA (175°C for 12 hrs)

0-E-8: Three step ST, AA (190°C for 4 hrs, (water) 50°C for 1 hr, 130°C for 30 hrs)

0-F-8: Three step ST, AA (175°C for 12 hrs)

0-D-8: Three step ST, AA (190°C for 4 hrs, (water) 50°C for 1 hr, 130°C for 20 hrs)

Figure 4.30: Average elongation and the maximum corrosion depths for third series heat treatments.

As can be seen from Figure 4.30, sample 0-D-8 with the best intergranular corrosion resistance and lower levels of pitting has an average elongation of 6.2% and test sample 0-C-8 exhibiting the highest intergranular corrosion depth of 500µm had an average elongation of 9.6%. Sample 0-C-8 has larger, interconnected intermetallic precipitates on the grain boundaries than sample 0-D-8 (see Fig. 4.54). Thus, the size and distribution of intermetallic precipitates may affect the elongation. Test samples 24-B-8 and 24-C-8 with the highest elongation values (>10%) were highly susceptible to intergranular corrosion.



#### 4.8 SEM fracture analysis of the tensile test bars subjected to 3-step ST and 2-step AA conditions (with and without NA)

Test sample 24-C-8 which was subjected to 3-step ST and 24 hrs NA followed by 2-step AA (190°C for 0.5 hr followed by water quenching at 50°C for 1 hr, 130°C for 30 hrs) exhibited 15.5% elongation in spite of some isolated shrinkage macroporosity cavities having a diameter of up to 180µm. These can be seen in the fracture surface shown in Fig. 4.31.



Figure 4.31: a) SEM Micrograph of fractured sample 24-C-8.

The SEM micrograph, Fig. 4.32, shows the localized secondary cracks and a combination of dimple rupture and brittle fracture micro regions. Most of the regions in sample 0-C-8 are covered with dimple ruptures.



Figure 4.32: b) SEM Micrograph of fractured sample 24-C-8.

Figure 4.33 shows the ductile fracture of tensile test sample 24-C-8. Higher magnification micrographs (Fig. 4.33 and Fig. 4.34) of the ductile regions revealed larger dimples having a diameter of up to  $10\mu\text{m}$  and smaller dimples having a diameter of up to  $2\mu\text{m}$ .



Figure 4.33: SEM Micrograph of fractured sample 24-C-8.

In Figure 4.34, constituents or second-phase particles having a diameter of up to  $3\mu\text{m}$  can be seen at the bottom of elongated dimples. Sample 0-C-8 and 0-B-8 with shorter first step AA time have smaller dimples ( $10\text{-}15\mu\text{m}$  diameter).

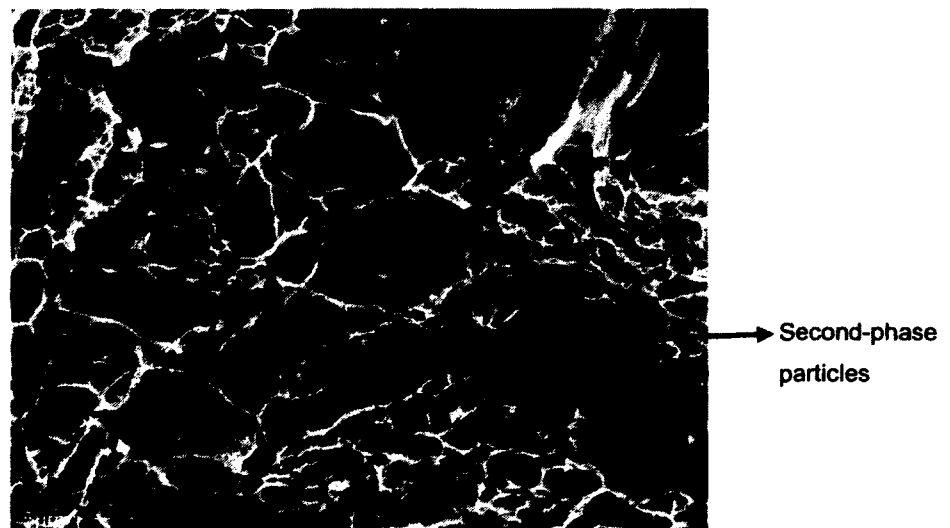


Figure 4.34: SEM Micrograph of fractured sample 24-C-8.

Test sample 0-B-8 was subjected to 3-step ST followed by 2-step AA (190°C for 0.5 hr, water quenching at 50°C for 1 hr, 130°C for 20 hrs). Low magnification micrograph, Fig. 4.35, shows the intergranular fracture mode. Shrinkage porosity cavities having a diameter of up to 125µm can be seen at the bottom left corner of the micrograph.

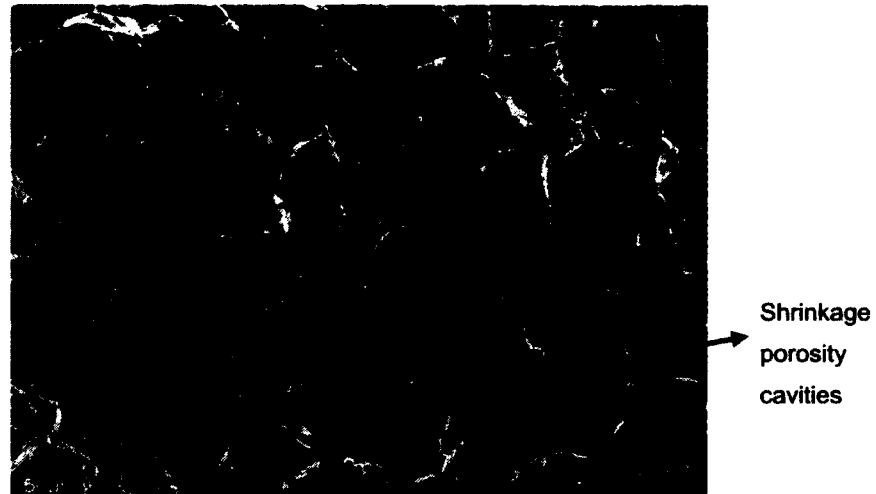


Figure 4.35: a) SEM Micrograph of fractured sample 0-B-8.

Fractured sample 0-B-8 exhibits 16.9% elongation. At higher magnification, predominant dimple ruptures and localized brittle fracture micro regions can be seen (Fig. 4.36). Brittle fracture in samples 24-C-8 and 0-B-8 is lower than sample 0-D-8. An increase in first step AA time from 0.5 to 4 hrs decrease the dimple ruptures and increase the brittle fracture. This may be the reason for higher elongation in samples 24-C-8 and 0-B-8 compared to 0-D-8.

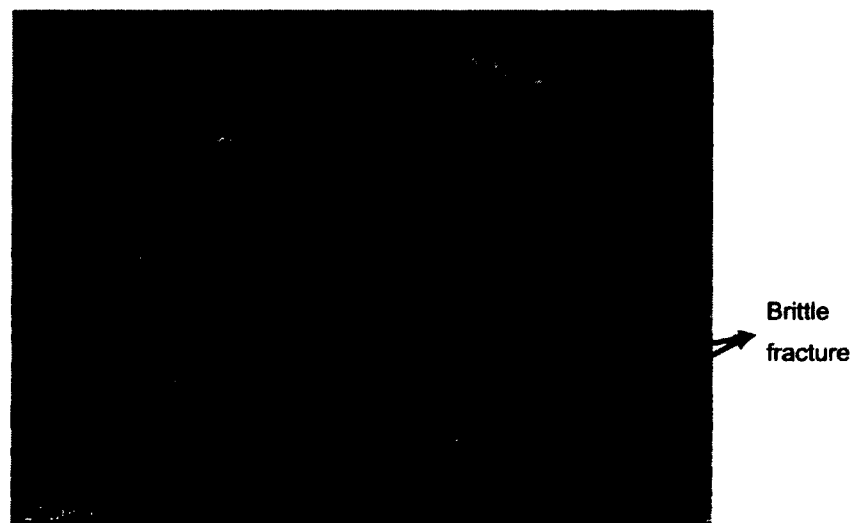


Figure 4.36: b) SEM Micrograph of fractured sample 0-B-8.

Figure 4.37 shows the fracture surface of test sample 0-B-8. Higher magnification of ductile regions (in Fig. 4.37) revealed larger dimples having a diameter of up to  $15\mu\text{m}$  and smaller dimples having a diameter of up to  $2\mu\text{m}$ . Localized secondary cracking is predominant on the right side of the micrograph in Fig. 4.37.



Figure 4.37: SEM Micrograph of fractured sample 0-B-8.

Test sample 0-D-8 was subjected to 3-step ST followed by two step AA (190°C for 4 hrs followed by water quenching at 50°C for 1 hr, 130°C for 20 hrs). Fractured sample 0-D-8 exhibits 7.4% elongation. Interconnected shrinkage porosity cavities having a diameter of up to 215µm can be seen on the micrograph: Fig. 4.38.

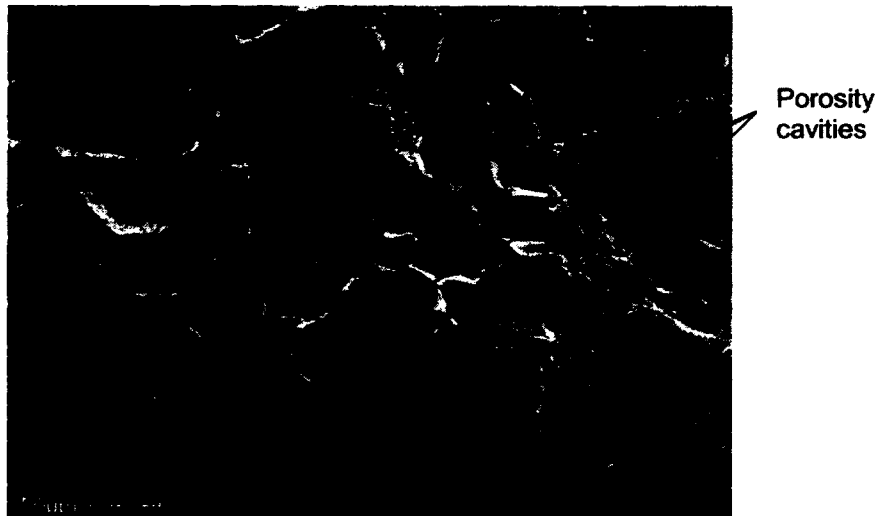


Figure 4.38: SEM Micrograph of fractured sample 0-D-8.

In Figure 4.39, brittle fracture micro regions are found at the center and on the left side of the micrograph. Ductile features and micro porosity cavities can be seen on the fracture surface.



Figure 4.39: SEM Micrograph of fractured sample 0-D-8.

In Figure 4.40, the localized brittle fracture mode can be seen at the center and right side of the micrograph. Higher magnification revealed large dimples having a diameter of  $25\mu\text{m}$  and small dimples having a diameter of  $3\mu\text{m}$ .

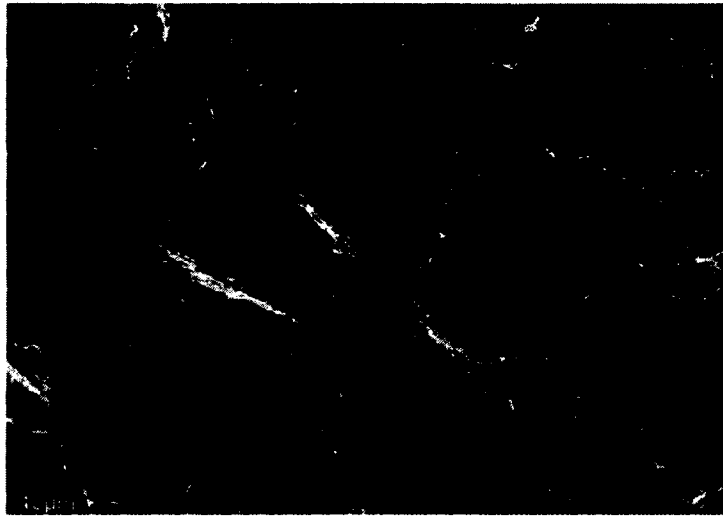


Figure 4.40: SEM Micrograph of fractured sample 0-D-8.

In Figure 4.41, constituents or second phase particles having a diameter of up to  $2\mu\text{m}$  can be seen at the bottom of the dimples. Fractured sample 0-D-8 having larger dimples of up to  $25\mu\text{m}$  render poor elongation. Most of the regions are having the brittle fracture: Fig. 4.40 and Fig. 4.41

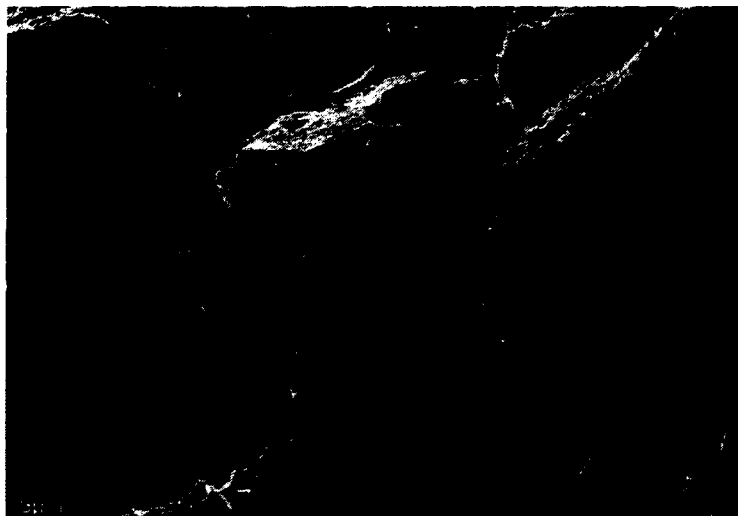


Figure 4.41: SEM Micrograph of fractured sample 0-D-8.

An increase in first step AA holding time increases the dimple size and brittle fracture. Longer first step AA time also decreases the dimple ruptures. The type and nature of the fracture will strongly depend on the first step AA time than the second step AA time. Thus, sample 0-D-8 with longer first step AA time has low elongation compared to samples 24-C-8 and 0-B-8 with shorter first step AA time.

#### **4.9 Quality Index of the B206 alloy subjected to 3-step ST, NA (0&24h), and 2-step AA**

The quality index of the B206 alloy was calculated based on Caceres analytical model [68].

Iso-Q lines are calculated by the following empirical relationship

$$Q = UTS + d \log (s_f) \quad (4.1)$$

where Q is the quality index, UTS is the high tensile strength and  $s_f$  is the elongation to fracture.

The value of d can be obtained by differentiating Eq. (2.7) at  $q = 1$ ,

$$d \cong 0.4 K \quad (4.2)$$

Substituting Eq. 2.5, 2.6 and 4.2 in Eq. 4.1,

$$Q = K [(qn)^n e^{-qn} + 0.4 \log (100qn)] \quad (4.3)$$

##### **4.9.1 True stress-strain curves**

True stress-strain curves were generated for the third series heat treatments (see Figs. 4.42-4.49). N is the number of samples. Each curve represents a different specimen. The 0-B series and 0-C series samples have high true fracture strain (Figs. 4.42 and

4.43) compared to 0-D series and 0-E series (Figs. 4.44 and 4.45). An increase in first step AA time from 0.5 to 4 hrs decreases the true fracture strain.

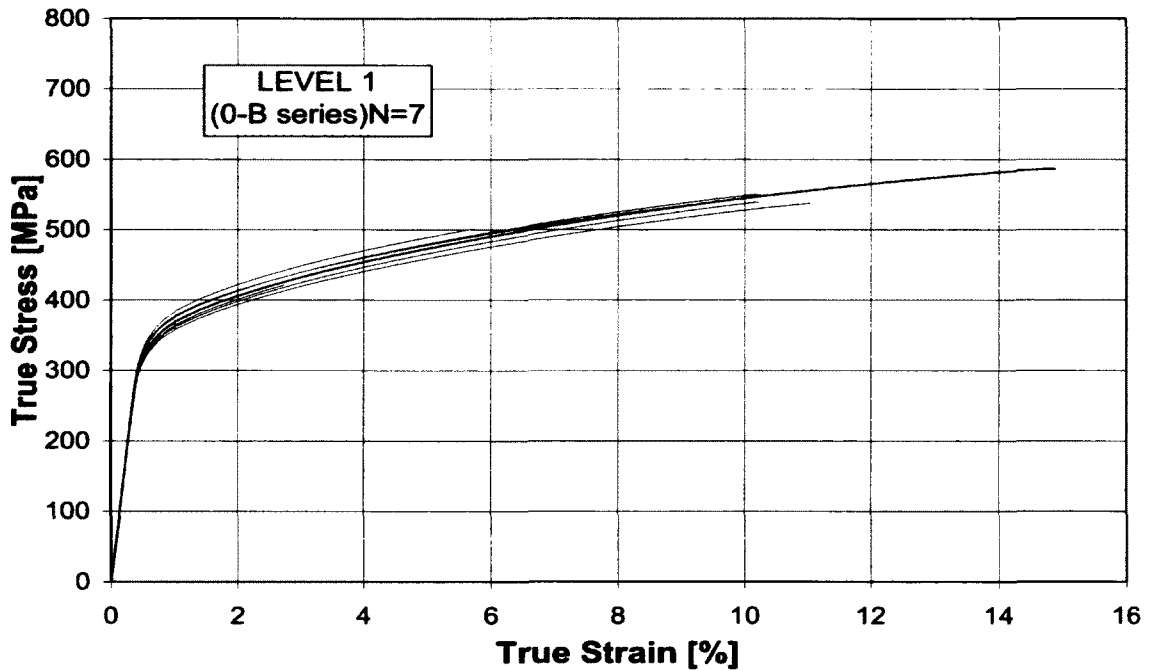


Figure 4.42: Flow curves of 0-B series: 3-step ST (515°C/3h, 530°C/8, 535°C/4h), 2-step AA @ (190°C/0.5h, 50°C/1h (water quenching), 130°C/20h).

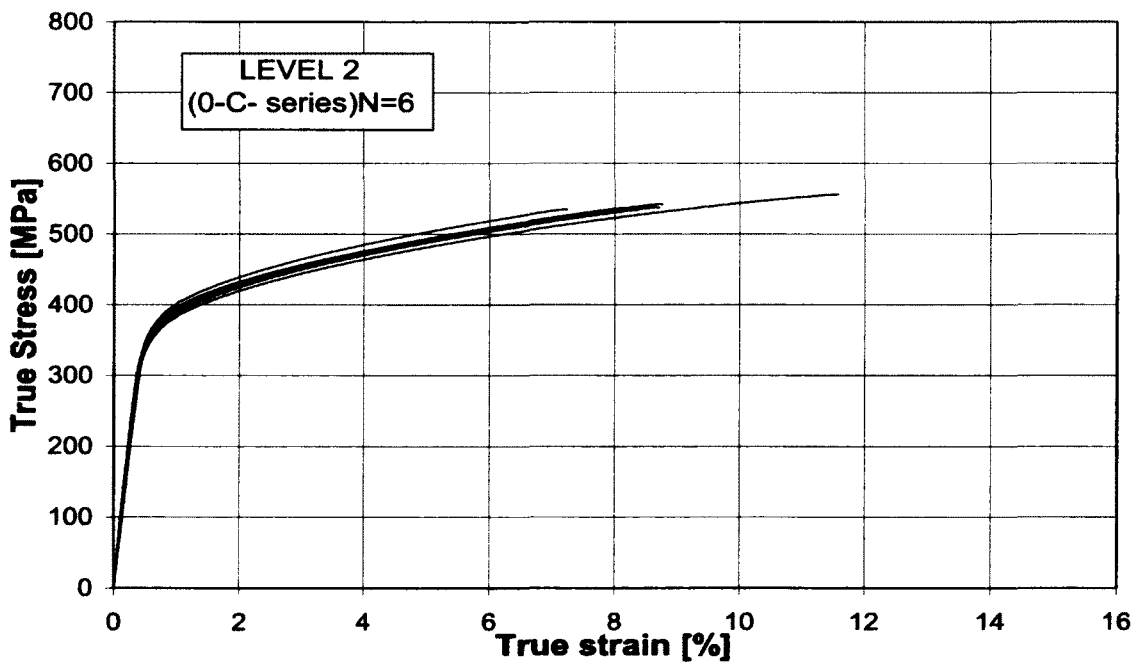


Figure 4.43: Flow curves of 0-C series: 3-step ST (515°C/3h, 530°C/8, 535°C/4h), 2-step AA @ (190°C/0.5h, 50°C/1h (water quenching), 130°C/30h).



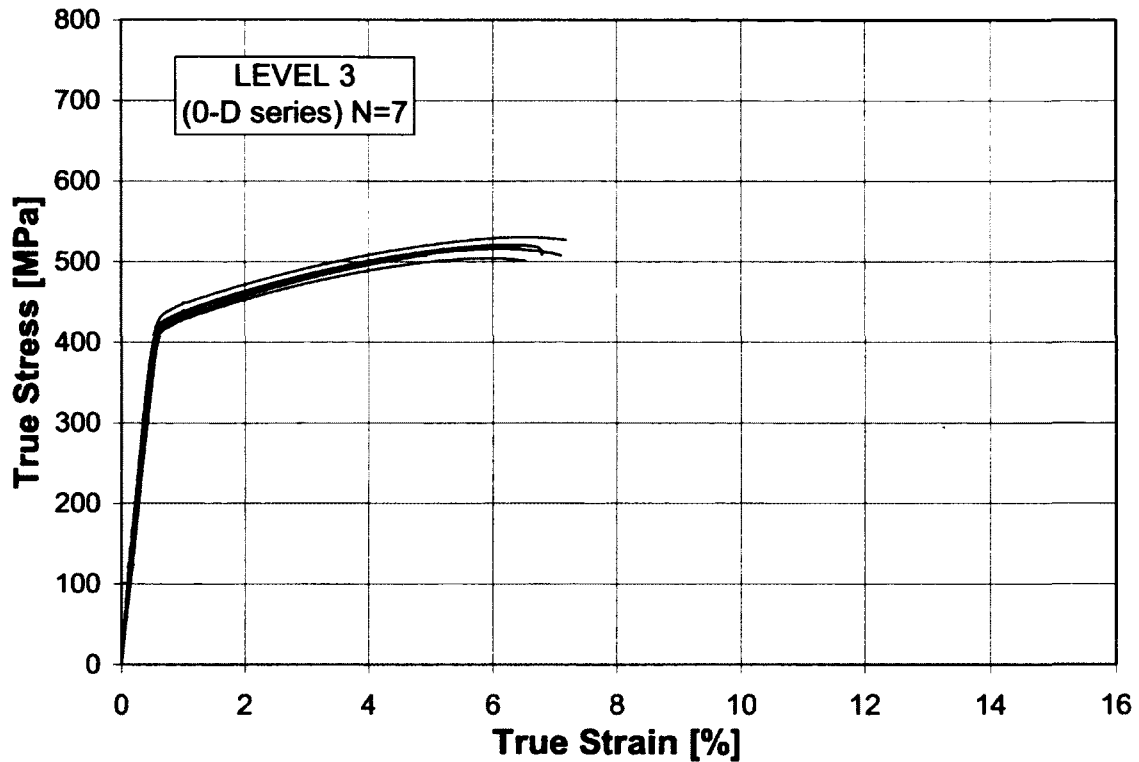


Figure 4.44: Flow curves of 0-D series: 3-step ST (515°C/3h, 530°C/8, 535°C/4h), 2-step AA @ (190°C/4h, 50°C/1h (water quenching), 130°C/20h).

0-D series and 0-E series samples withstand high stress and their Yield Strengths (YS) (refer Fig. 4.44 and 4.45) were higher than the 0-B series and 0-C series test samples. From the tensile data of the third series heat treatment experiments, it is clear that samples having longer first step AA time (4 hrs) exhibits high YS and low fracture strain (< 10%). Samples having shorter first step AA time (0.5 hrs).exhibits high fracture strain ( $\geq 10\%$ ).

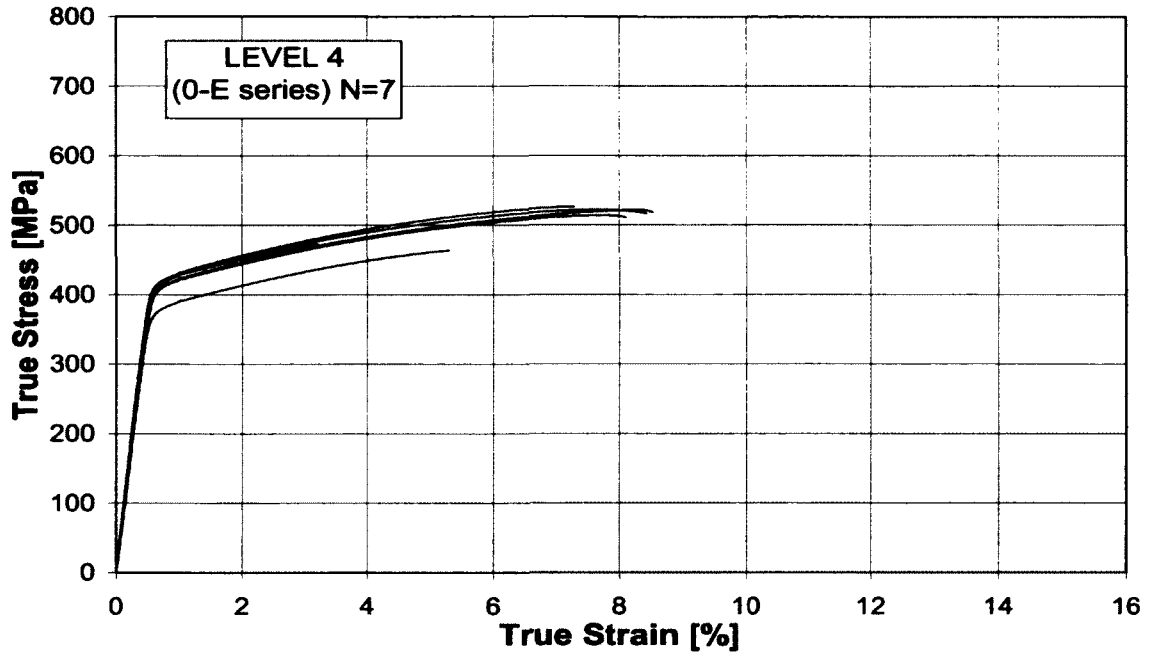


Figure 4.45: Flow curves of 0-E series: 3-step ST (515°C/3h, 530°C/8, 535°C/4h), 2-step AA @ (190°C/4h, 50°C/1h (water quenching), 130°C/30h).

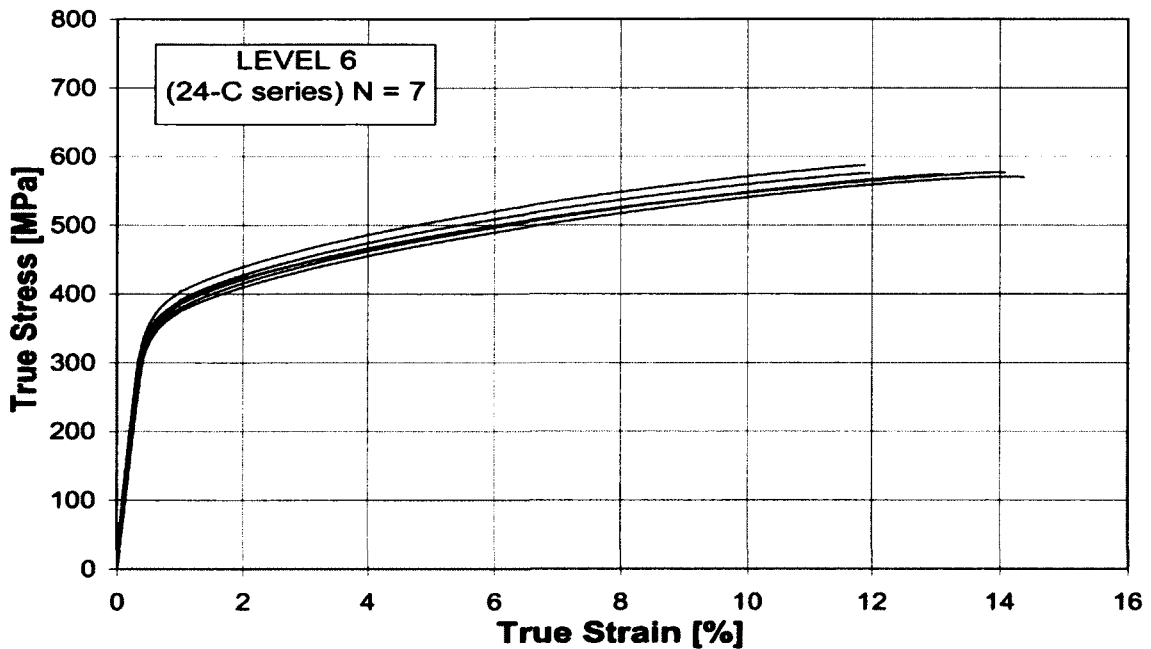


Figure 4.46: Flow curves of 24-C series: 3-step ST (515°C/3h, 530°C/8h, 535°C/4h), 24h NA, 2-step AA @ (190°C/0.5h, 50°C/1h (water quenching), 130°C/30h).

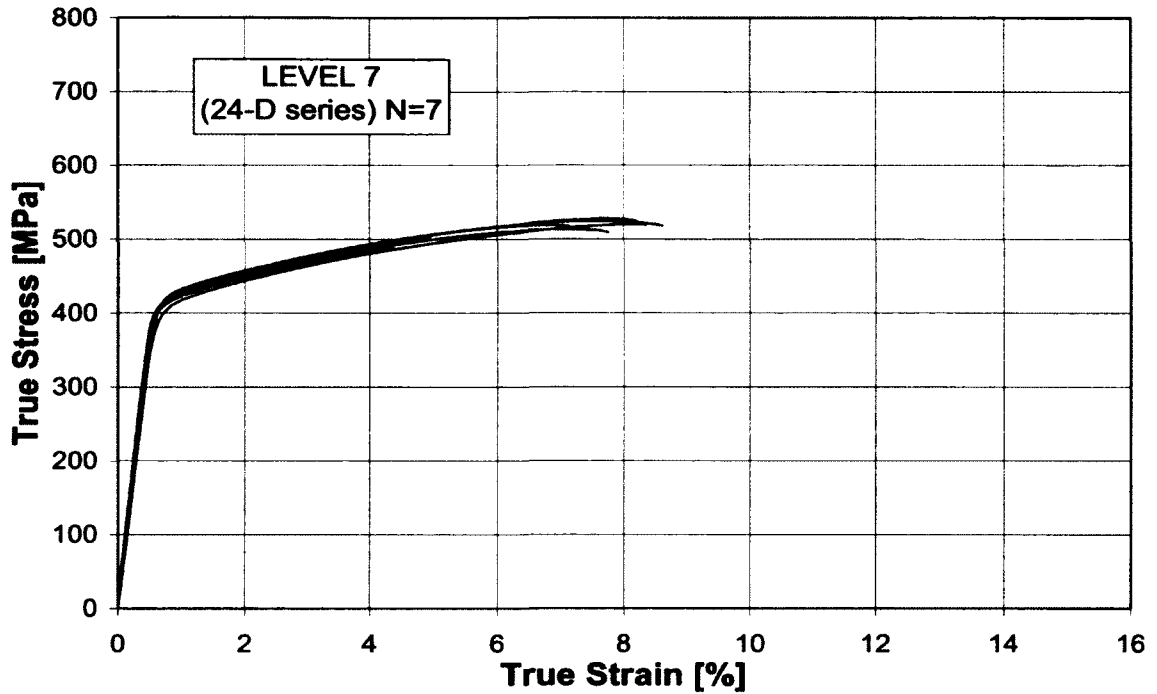


Figure 4.47: Flow curves of 24-D series: 3-step ST (515°C/3h, 530°C/8h, 535°C/4h), 24h NA, 2-step AA @ (190°C/4h, 50°C/1h (water quenching), 130°C/20h).

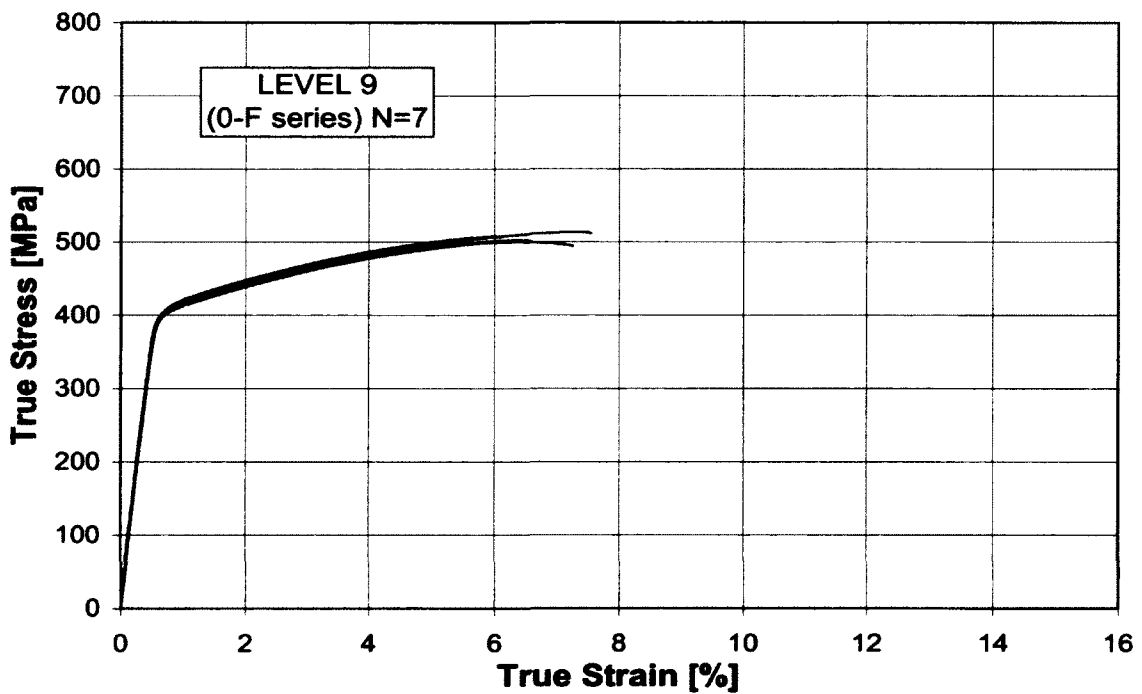


Figure 4.48: Flow curves of 0-F series: 3-step ST (515°C/3h, 530°C/8h, 535°C/4h), 1-step AA @ (175°C/12h).

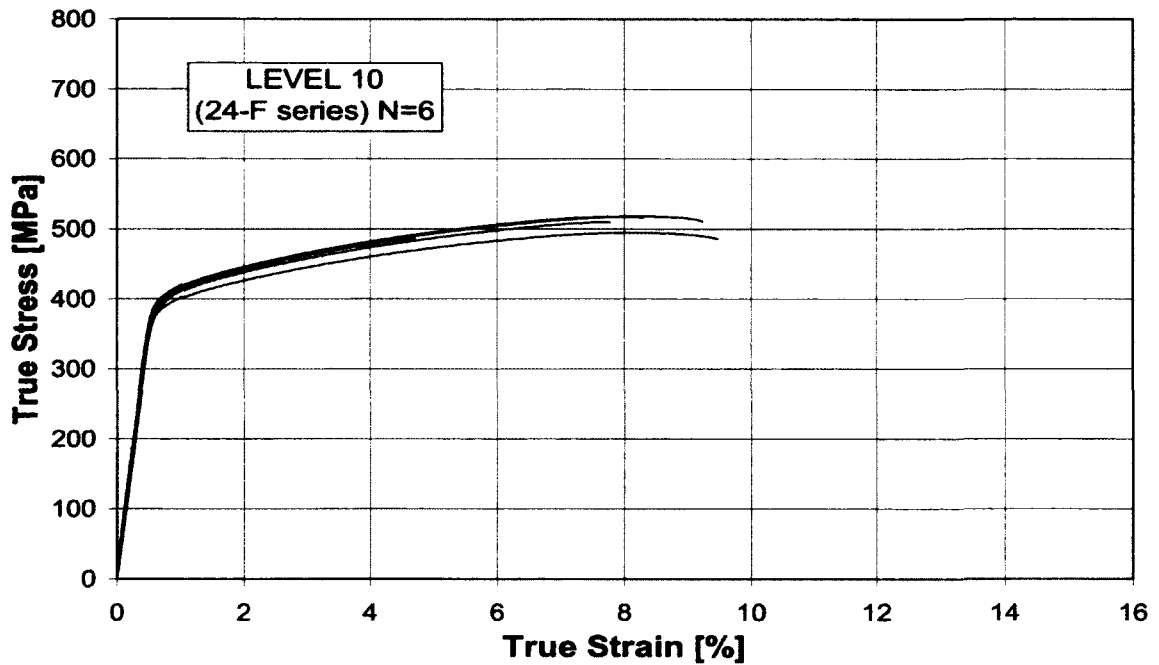


Figure 4.49: Flow curves of 24-F series: 3-step ST (515°C/3h, 530°C/8h, 535°C/4h), 24h NA, 1-step AA @ (175°C/12h).

#### 4.9.2 K & n values

Table 4.10: n and K values for the third series heat treated samples (section 3.5).

Level	Series	Number of samples, N	Average, n	Std. Dev., n	Average, K, MPa	Std. Dev., K,
1	0-B	7	0.162	0.0091	785	27.232
2	0-C	6	0.149	0.0031	773	7.3484
3	0-D	7	0.093	0.00754	703	15.1516
4	0-E	7	0.095	0.00648	700	11.326
6	24-C	7	0.160	0.0046	797	4.391
7	24-D	7	0.097	0.00332	706	7.41619
9	0-F	7	0.100	0.00214	706	7.416
10	24-F	6	0.105	0.00192	698	8.55236

### 4.9.3 Quality Index Plot

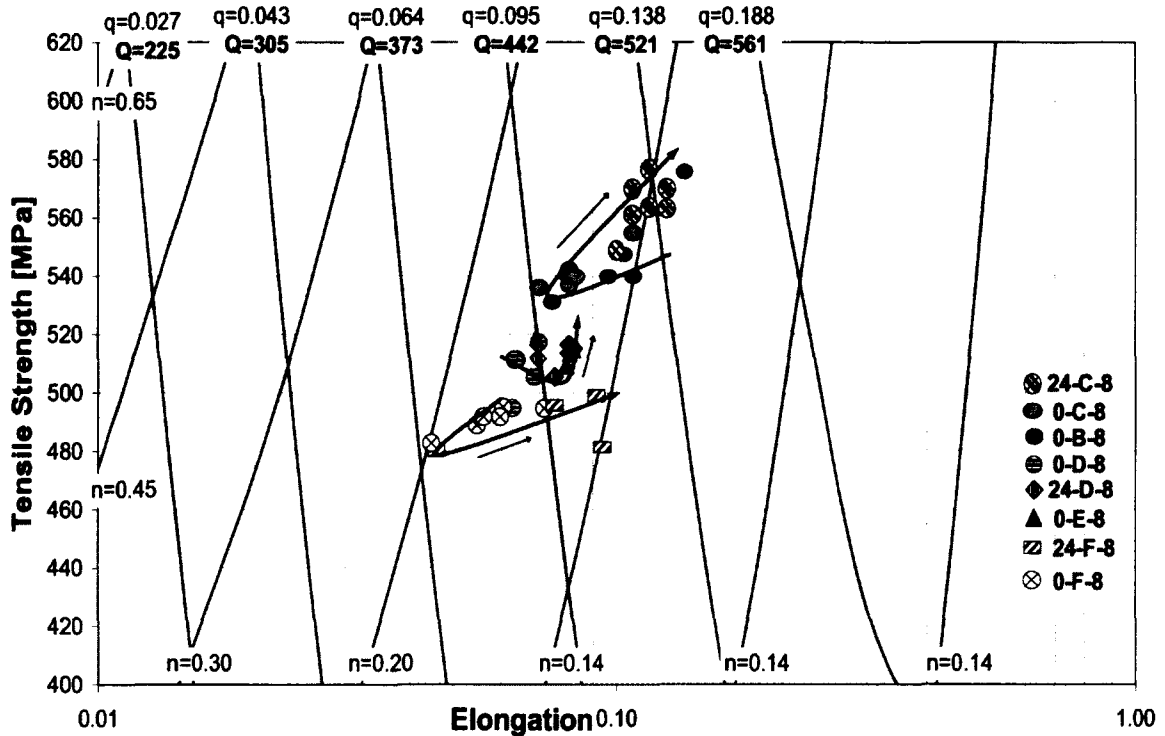


Figure 4.50: A quality index chart for the B206 alloy. The iso-q lines, identified by the q-value and the iso-YS lines, identified by the n-value, were calculated from Eq. (2.7) and (2.5). Q values were calculated from Eq. (4.3), with  $K = 736$  MPa. The arrow indicates the strength-ductility path of the B206 alloy (3-step ST, NA (0&24h), 2-step AA).

The strength and ductility were decreased as the samples were overaged. Overaging causes a fall in quality as the data points follow a circular path: see Fig. 4.50. When the B206 test samples were subjected to a longer first step AA time (4 hrs), a decrease in the K value (strength coefficient) was observed (see Table 4.10). 24-C series test samples (3-step ST (515°C/3h, 530°C/8, 535°C/4h), NA (24h), 2-step AA @ (190°C/0.5h, 50°C/1h (water quenching), 130°C/30h)) show higher elongation and tensile strength. The 24h NA operation performed in 24-C series samples was the reason for high elongation compared to the 0-C series samples.

#### 4.10 Potentiodynamic Polarization testing

The potentiodynamic polarization curves for the third series heat treatment conditions are given in Figure 4.51. Table 4.11 presents the values of the corrosion parameters ( $\beta_a$ ,  $\beta_c$ ,  $E_{corr}$ ,  $i_{corr}$ ,  $R_p$ ) obtained from these curves.  $i_{corr}$  varied from 6 to 56  $\mu A/cm^2$  and  $R_p$  varied from 430 to 48  $ohm.cm^2$ . The corrosion potential,  $E_{corr}$ , varied from -0.57 V to -0.80 V. No passive region and pitting potential were obvious in any of the polarization curves presented in Figure 4.51. This would indicate that localized corrosion occurs at open circuit ( $E_{corr}$ ), i.e.,  $E_{corr} > E_{pit}$ . Hence the measured corrosion current will be largely due to such phenomena and, as such, do not reflect the extent of uniform/general corrosion – unless of course pitting is so extensive that uniform corrosion by pitting occurs. Strictly, therefore,  $R_p$  should not be used as a measure of uniform corrosion resistance.  $R_p$  is, however, still related to the rate of metal dissolution and has been used for purposes of comparison.

In terms of overall corrosion, the heat treatment schedule that gave the best corrosion resistance (highest  $R_p$ ; lowest  $i_{corr}$ ) was 0-C-8 which had no NA and a 2-step AA treatment.  $E_{corr}$  for 0-C-8 (-0.596 V) was also amongst the most noble recorded for the nine different heat treatments. The least corrosion resistant condition was 24-D-8 (NA + 2-step AA) which had the lowest  $R_p$  (48  $ohm.cm^2$ ), highest  $i_{corr}$  (56  $\mu A/cm^2$ ) and least noble  $E_{corr}$  (-0.80 V). It is interesting to note that the potentiodynamic polarization curves for both 0-C-8 and 24-D-8 show an apparent breakdown potential. The significance of this apparent breakdown potential is unclear since the current immediately prior to these breakdowns is much higher than normally associated with passivity. No definite conclusions can be drawn as to the benefits, or otherwise of either a 1-step, 2-step AA or NA prior to AA, on the overall corrosion resistance.

**Table 4.11: Results of potentiodynamic corrosion testing**

Sample ID	Third series heat treatment conditions	$\beta_a$	$\beta_c$	$E_{corr}$ (V)	$i_{corr}$ ( $\mu\text{A}/\text{cm}^2$ )	Polarisation Resistance, $R_p$ (ohms. $\text{cm}^2$ )
0-B-8	NA(0h), AA(190°C/0.5h, (water quenching) 50°C/1h, 130°C/20h)	0.0104	0.0153	-0.577	20.493	131.36
0-C-8	NA(0h), AA(190°C/0.5h, (water quenching) 50°C/ 1h, 130°C/30h)	0.0097	0.0152	-0.596	5.979	430.58
0-D-8	NA(0h),AA(190°C/4h, (water quenching) 50°C/1h, 130°C/20h)	0.0154	0.0164	-0.635	44.149	78.21
0-F-8	NA(0h),AA(175°C/12h)	0.0113	0.0107	-0.661	21.402	111.65
24-B-8	NA(24h),AA(190°C/0.5h , (water quenching) 50°C/1h, 130°C/20h)	0.0128	0.0163	-0.574	12.275	253.95
24-C-8	NA(24h),AA(190°C/0.5h , (water quenching) 50°C/1h, 130°C/30h)	0.0112	0.0148	-0.585	14.406	192.41
24-D-8	NA(24h),AA(190°C/4h, (water quenching) 50°C/1h, 130°C/20h)	0.0146	0.0107	-0.80	56.246	47.73
24-E-8	NA(24h),AA(190°C/4h, (water quenching) 50°C/1h, 130°C/30h)	0.0105	0.0166	-0.614	47.472	58.91
24-F-8	NA(24h),AA(175°C/12h)	0.0142	0.0153	-0.775	25.82	124.01

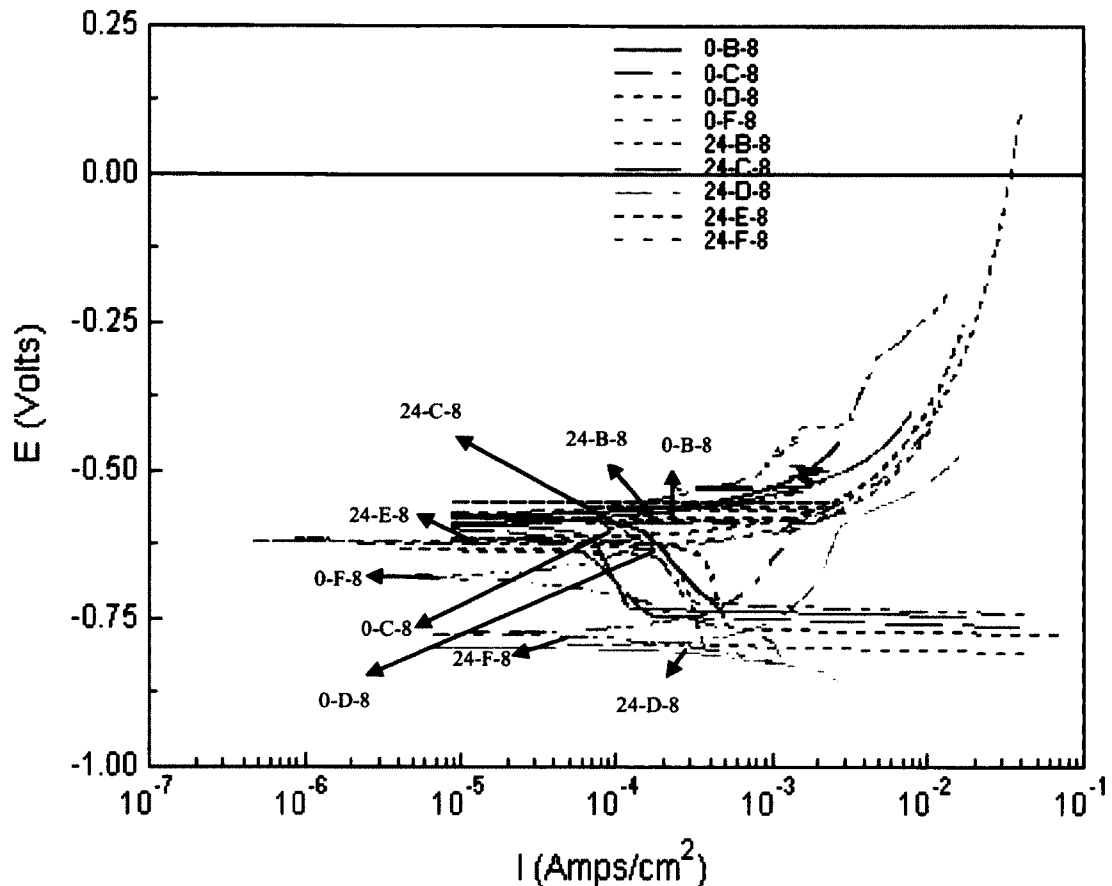


Figure 4.51: Potentiodynamic polarization curves for heat treated B206 alloy.

#### 4.10.1 SEM examination of selected specimens from potentiodynamic corrosion testing.

SEM micrographs of four selected specimens following potentiodynamic corrosion testing are shown in Figures 4.52 (a)-(d) and 4.53 (e)-(h). There are two micrographs for each heat treatment condition, one at low magnification (75X) and one at a higher magnification (500X). If we compare Figures 4.52 (a) & (b) for 24-F-8 with Figures 4.52 (c) & (d) for 0-F-8 we can readily see the effect of natural aging on one-step artificially aged specimens: more pits are visible in the specimen (0-F-8) without natural aging and the pits are reasonably well distributed. It should also be noted that 0-F-8 did not show intergranular corrosion in the immersion corrosion testing (see section 4.10.2). Figures 4.53 (e) & (f) for 0-C-8 and Figures 4.53 (g) & (h) for 0-D-8 show the effects of varying the aging times in the 2-step artificial aging (no natural aging). Larger pits were seen in 0-D-8 which had the longer first-step aging time at 190°C. No intergranular corrosion was



seen for 0-D-8 in the immersion testing. 0-C-8 (Figures 4.53 (e) & (f)) had the highest value of  $R_p$  and the lowest value of  $i_{corr}$  but exhibited the greatest depth of intergranular corrosion in the immersion testing.

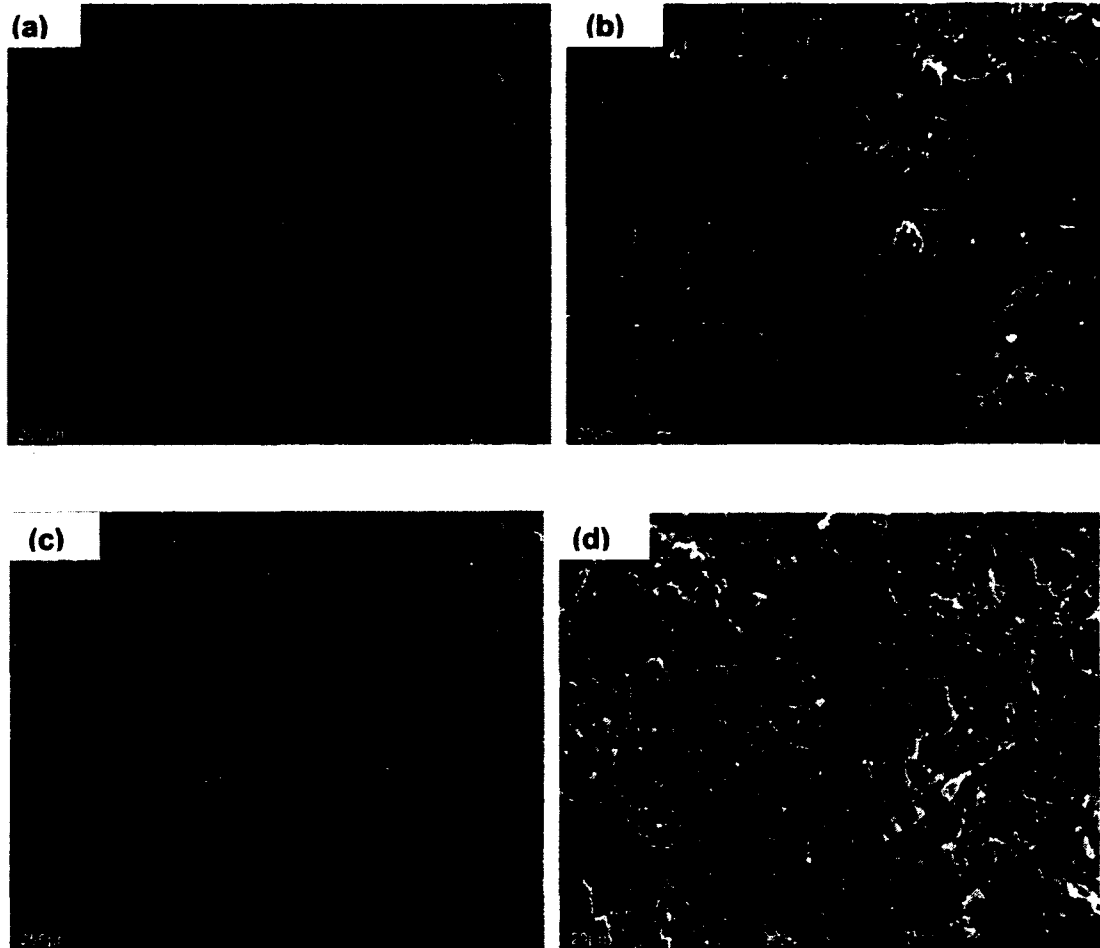


Figure 4.52: SEM micrographs of specimens following potentiodynamic corrosion testing

- 24-F-8: 3-step ST (515°C/3h, 530°C/8h, 535°C/4h, water quenching 66°C), 24h NA, 1-step AA @ (175°C/12h): (a) 75X and (b) 500X.
- 0-F-8: 3-step ST (515°C/3h, 530°C/8h, 535°C/4h, water quenching 66°C), 1-step AA @ (175°C/12h): (c) 75X and (d) 500X.

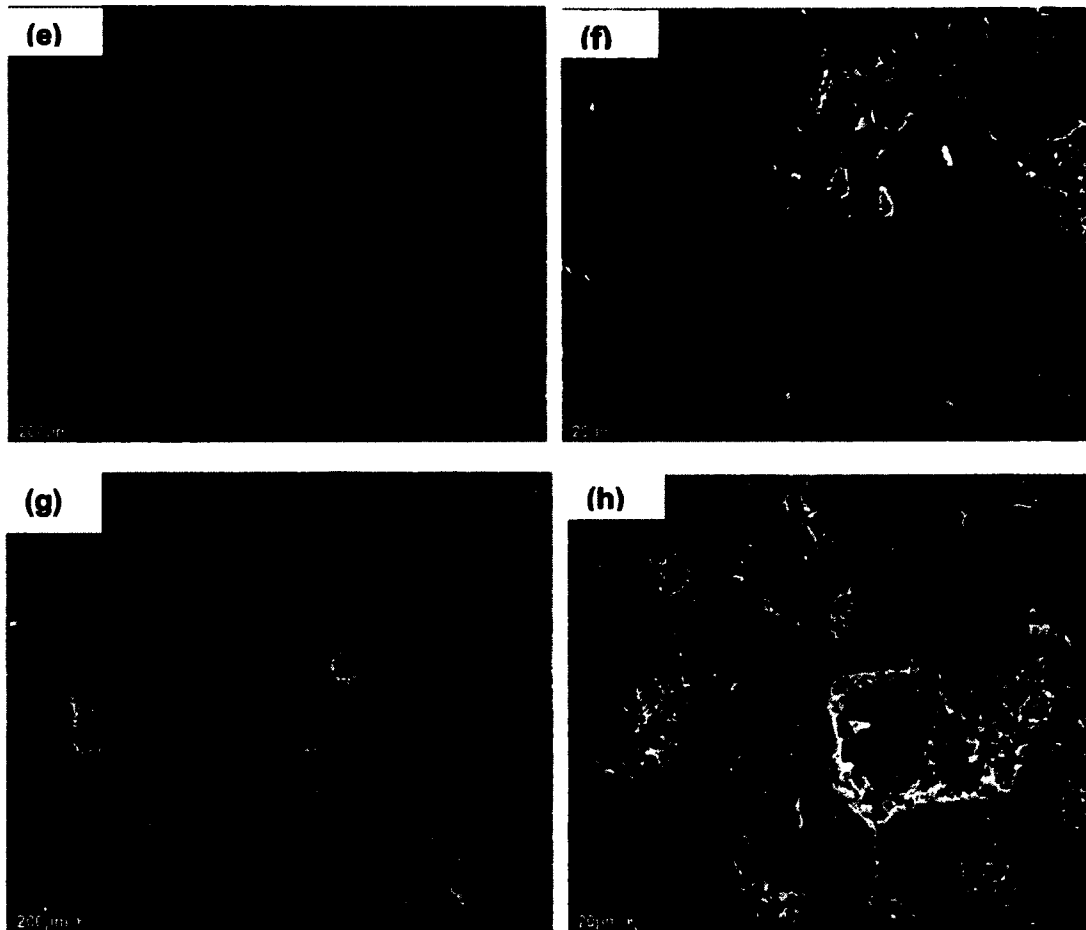


Figure 4.53: SEM micrographs of specimens following potentiodynamic corrosion testing

- 0-C-8: 3-step ST (515°C/3h, 530°C/8h, 535°C/4h, water quenching 66°C), 2-step AA @ (190°C/0.5h, 50°C/1h (water quenching), 130°C/30h): (e) 75X and (f) 500X.
- 0-D-8: 3-step ST (515°C/3h, 530°C/8h, 535°C/4h, water quenching 66°C), 2-step AA @ (190°C/4h, 50°C/1h (water quenching), 130°C/20h): (g) 75X and (h) 500X.

#### 4.10.2 Comparison of potentiodynamic and immersion corrosion testing results and mechanical testing (elongation)

In this section a comparison is made of the results from potentiodynamic corrosion testing, immersion corrosion testing and mechanical testing (elongation). For the immersion testing, results are presented on both the depth of intergranular penetration (if any) and depth of pitting. For intergranular corrosion and pitting corrosion, two values are given: these are for the non machined specimens/machined surface specimens. The tabular summary, Table 4.12, is setup in a ranked order with the specimen with the

“best” performance for that particular parameter being ranked 1 and the “worst” being ranked 9.

The first general observation is that if there was no intergranular corrosion, then the specimens exhibited a higher level of “general” corrosion (as evidenced by higher  $i_{corr}$ ; lower  $R_p$ ) and lower elongation (below the 7% threshold). The second general observation is that as  $E_{corr}$  became more anodic (from -0.57V to -0.80V) there was a general trend to greater depths of intergranular penetration (and to a lesser extent, a greater depth of pitting). This may be related to the size and distribution of the Cu-containing intermetallic precipitates. The microstructures of two specimens (0-C-8 and 0-D-8) exhibiting the highest level of intergranular corrosion (0-C-8) and no intergranular corrosion (0-D-8) are discussed in section 4.10.3.

**Table 4.12:** Comparison of potentiodynamic polarization testing with the immersion testing and mechanical property results.

Rank	$E_{corr}$ (V)	$i_{corr}$ ( $\mu A/cm^2$ )	Polarisation Resistance, $R_p$ (ohms $cm^2$ )	Immersion Testing		Elongation (%)
				Intergranular ( $\mu m$ )	Pitting ( $\mu m$ )	
1	(24-B-8) -0.574	(0-C-8) 5.979	(0-C-8) 430.58	(0-D-8) 0	(24-C-8) 0*/120	(24-B-8) 14.3
2	(0-B-8) -0.577	(24-B-8) 12.275	(24-B-8) 253.95	(0-F-8) 0	(24-B-8) 70*/120	(24-C-8) 13.2
3	(24-C-8) -0.585	(24-C-8) 14.406	(24-C-8) 192.41	(0-B-8) 230*/300	(0-B-8) 90*/100	(0-B-8) 12.1
4	(0-C-8) -0.596	(0-B-8) 20.493	(0-B-8) 131.36	(24-D-8) 250*/250	(24-D-8) 100*/200	(0-C-8) 9.6
5	(24-E-8) -0.614	(0-F-8) 21.402	(24-F-8) 124.01	(24-B-8) 300*/375	(0-C-8) 130*/50	(24-D-8) 7.33
6	(0-D-8) -0.635	(24-F-8) 25.82	(0-F-8) 111.65	(24-C-8) 300*/400	(24-F-8) 130*/125	(24-F-8) 7.3
7	(0-F-8) -0.661	(0-D-8) 44.149	(0-D-8) 78.21	(24-E-8) 350*/225	(0-D-8) 170*/120	(0-F-8) 6.5
8	(24-F-8) -0.775	(24-E-8) 47.472	(24-E-8) 58.91	(24-F-8) 380*/250	(24-E-8) 200*/100	(0-D-8) 6.2
9	(24-D-8) -0.80	(24-D-8) 56.246	(24-D-8) 47.73	(0-C-8) 400*/500	(0-F-8) 200*/250	(24-E-8) Not Tested

\* - specimens that were not machined before immersion testing

#### **4.10.3 SEM & Optical Metallography (OM) showing the relationship between the distributions of Cu-intermetallics and intergranular corrosion.**

SEM and optical metallography was performed on polished and etched specimens (not corroded) of 0-C-8 and 0-D-8 to determine the size and distribution of the Cu-containing intermetallic precipitates. [0-D-8 exhibited no intergranular corrosion whereas 0-C-8 exhibited the highest depth of intergranular attack in the immersion corrosion test]. Selected SEM and OM micrographs are shown in Fig. 4.54. The OM micrographs in Fig. 4.54 show a similar distribution of precipitates as observed in the first series heat treatments, although, third series samples (0-C-8 & 0-D-8) show fine precipitates inside the grains. Precipitates of varying sizes and shapes are visible, including some that are needle-like. The OM micrographs, Figures 4.54 (e) & (f), show precipitate-free (denuded) zones at the grain boundaries and within the grains. The denuded zones appear to be more prevalent in 0-C-8 which also appeared to have more, larger, interconnected precipitates at the grain boundaries than specimen 0-D-8.

As noted by Buchheit et al [77], copper-rich intermetallic particles are noble with respect to the remainder of the alloy microstructure and function as local cathodes. Secondly, copper dissolved in an  $\alpha$ -Al solid solution raises the electrochemical potential of a given phase and increases resistance to galvanic attack. Consequently, elements of the alloy microstructure in which copper is depleted are most susceptible to electrochemical dissolution. The presence of the grain boundary denuded zones (Cu-depleted) and larger interconnected intermetallic precipitates in 0-C-8 would help explain the higher depth of intergranular attack. The magnitude of the galvanic couple between the intermetallic precipitate and the Cu-depleted zone would depend on the nature of the intermetallic precipitate since different precipitates exhibit different corrosion potentials in the NaCl/H<sub>2</sub>O<sub>2</sub> environment [77]. Values given in the literature for corrosion potentials of intermetallic precipitates that can be formed in B206 are: Al<sub>2</sub>Cu -0.44 or -0.64 V<sub>SCE</sub>; Al<sub>2</sub>CuMg -0.91 V<sub>SCE</sub>; Al<sub>6</sub>Mn -0.76 V<sub>SCE</sub> [78].

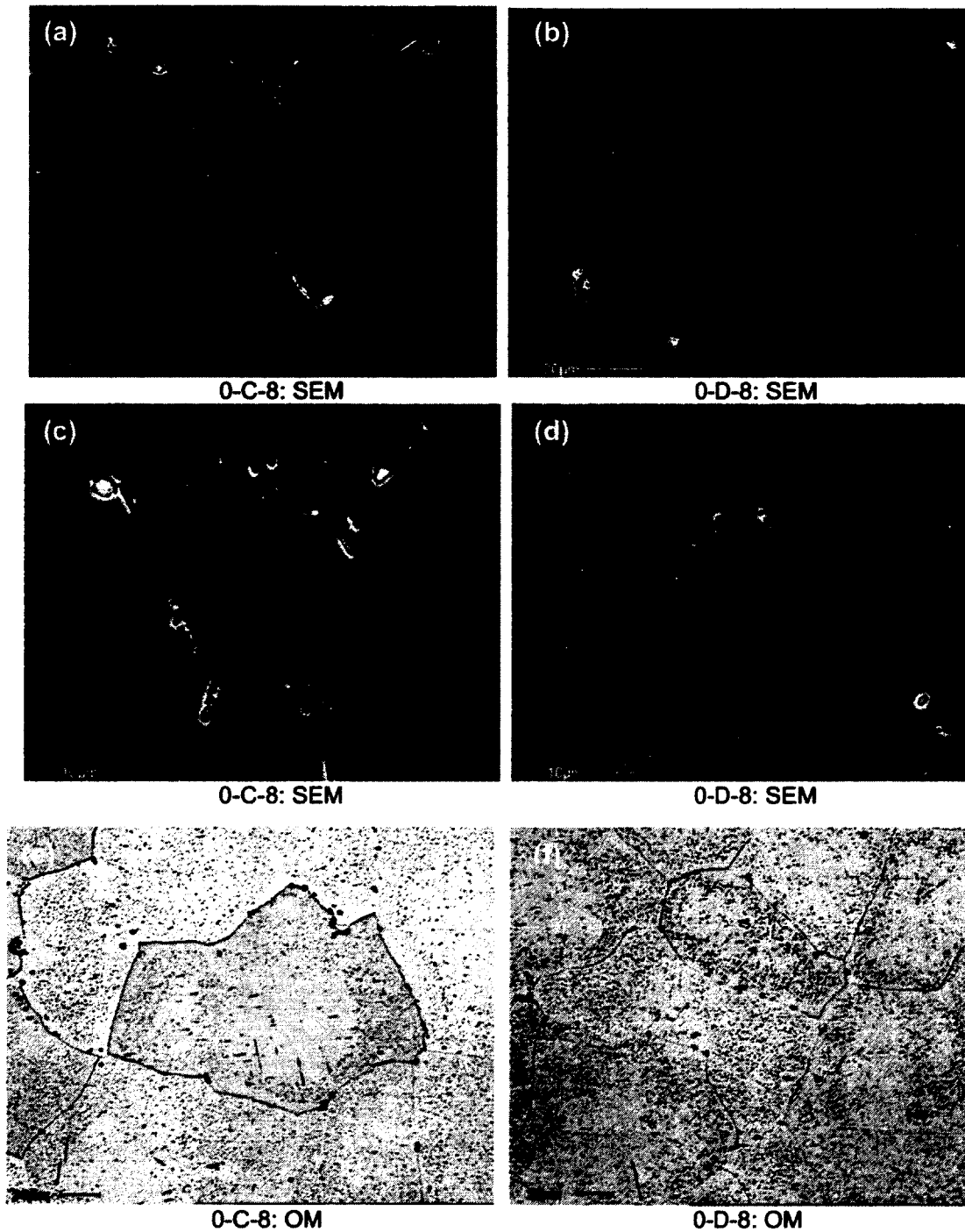


Figure 4.54: SEM & Optical Metallography images: (a), (c), (e) 0-C-8 (shorter first step AA time (0.5 hr) at 190°C and the second stage at 130°C for 30 hrs without NA). (b), (d), (f) 0-D-8 (longer first step AA time (4 hrs) at 190°C and the second stage at 130°C for 20 hrs without NA). Specimens were immersed for a few seconds in the etchant containing 920 ml of distilled water, 60 ml of nitric acid, and 20 ml of hydrofluoric acid for OM & SEM examination.

## 4.11 Tribocorrosion testing

### 4.11.1 Dry Wear Test

0-C-8, 24-F-8 and 0-D-8 having low, intermediate and high corrosion resistance (determined by immersion corrosion test) were selected for the dry wear test. The dry wear test (in the absence of corrosive medium) was performed against a 5mm alumina ball with a normal force of 9 N. Figure 4.55 shows the wear track of samples 24-F-8, 0-C-8 and 0-D-8. There is no significant difference in the wear track width: Table 4.13.

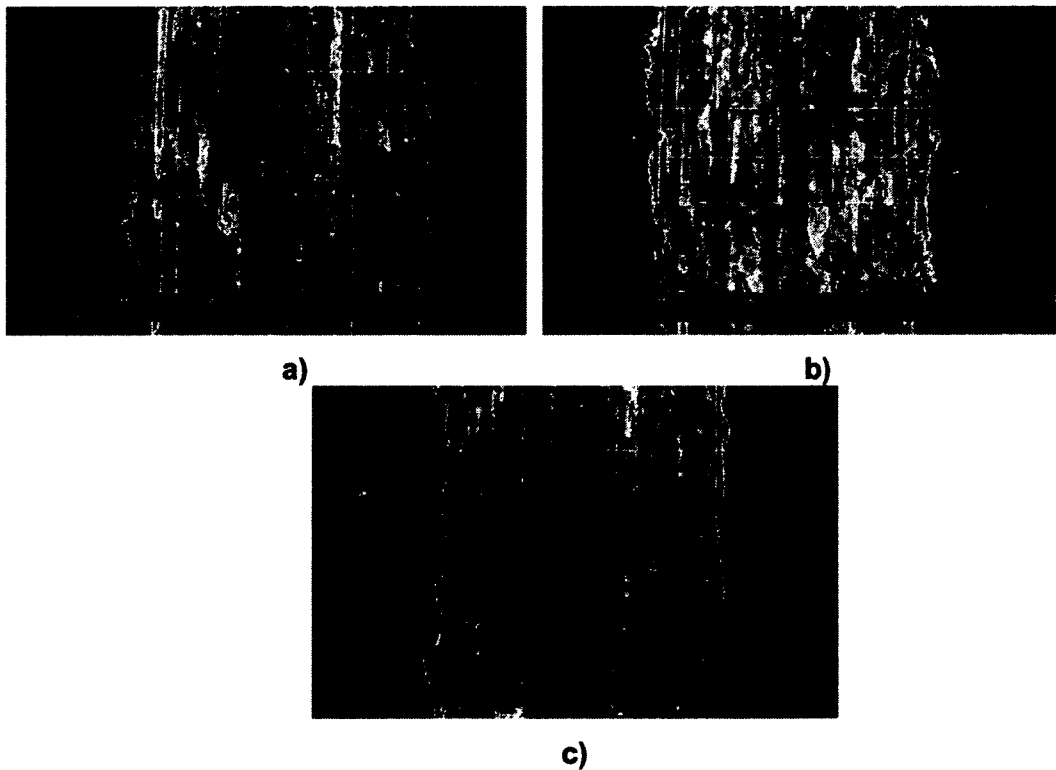


Figure 4.55: Dry wear track for test samples:

- a) 24-F-8: 3-step ST (515°C/3h, 530°C/8h, 535°C/4h, water quenching 66°C), 24h NA, 1-step AA @ (175°C/12h).
- b) 0-C-8: 3-step ST (515°C/3h, 530°C/8h, 535°C/4h, water quenching 66°C), 2-step AA @ (190°C/0.5h, 50°C/1h (water quenching), 130°C/30h).
- c) 0-D-8: 3-step ST (515°C/3h, 530°C/8h, 535°C/4h, water quenching 66°C), 2-step AA @ (190°C/4h, 50°C/1h (water quenching), 130°C/20h).

**Table 4.13:** Results of wear track width.

<b>Sample ID</b>	<b>Average Track width (mm)</b>	<b>Range (mm)</b>
24-F-8	1.26	1.23-1.28
O-C-8	1.24	1.23-1.26
O-D-8	1.22	1.21-1.23

#### **4.11.2 Wear in a Corrosive Medium**

A wear test (in the presence of a corrosive medium 3.5% NaCl solution) was performed on all three samples. This corrosive medium is different from the corrosive medium (57 g of sodium chloride, 10 ml of 30% hydrogen peroxide in 1 litre of distilled water) used for the immersion corrosion and potentiodynamic tests. The wear tracks of all three samples are shown in the Figure 4.56. Sample O-D-8 exhibits a minimum track width and sample 24-F-8 exhibits a maximum track width. In test sample 24-F-8 containing more  $\theta$  phase than O-C-8 & O-D-8, a higher corrosion rate was observed at more cathodic potential resulting in maximum removal on the surface of the sample. The track widths are detailed in Table 4.14.

On comparing Table 4.14 with Table 4.13, it is clear that the corrosive medium decreases the track width for all three samples. The track width for test sample O-C-8 was decreased from 1.24 to 1.03 mm and the track width for test sample O-D-8 was decreased from 1.22 to 0.94 mm.

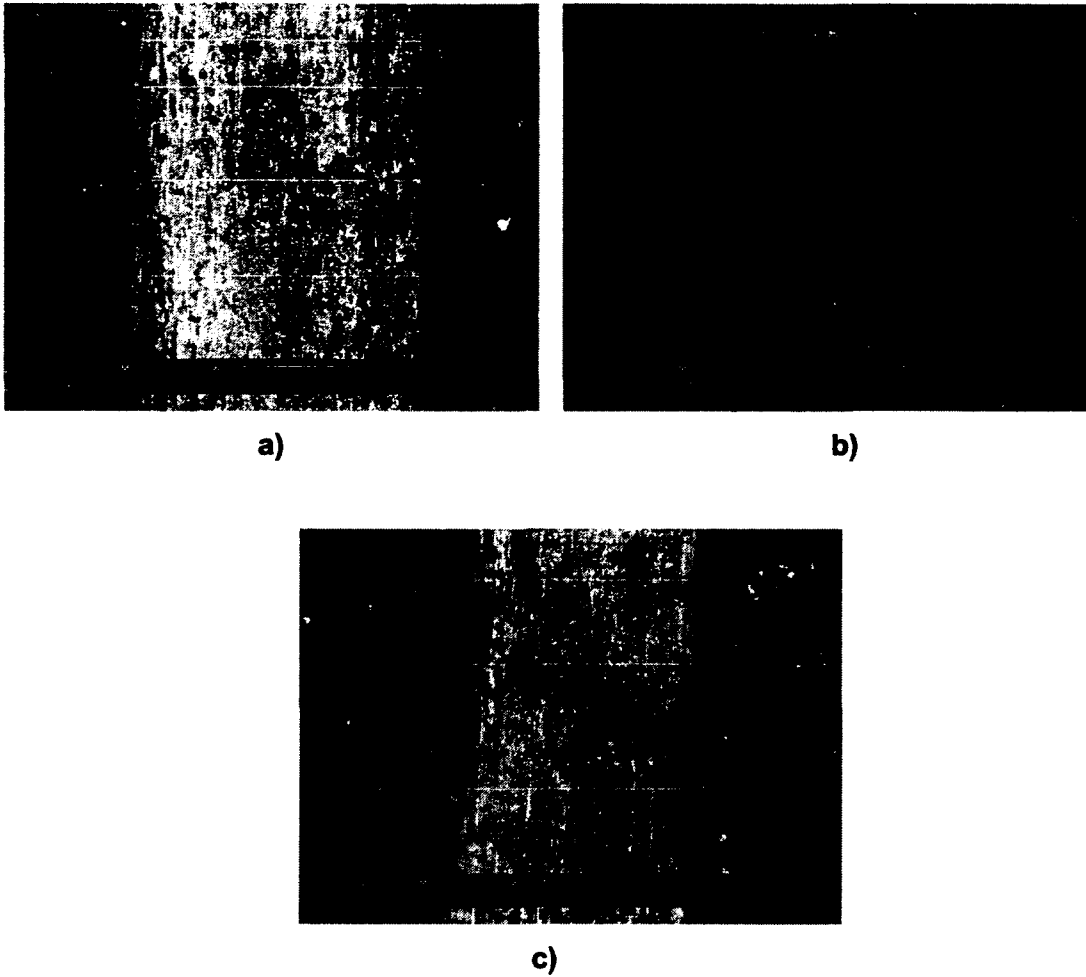


Figure 4.56: Wear track measured when the samples were exposed to a corrosive medium

a) 24-F-8: 3-step ST (515°C/3h, 530°C/8h, 535°C/4h, water quenching 66°C), 24h NA, 1-step AA @ (175°C/12h).

b) 0-C-8: 3-step ST (515°C/3h, 530°C/8h, 535°C/4h, water quenching 66°C), 2-step AA @ (190°C/0.5h, 50°C/1h (water quenching), 130°C/30h).

c) 0-D-8: 3-step ST (515°C/3h, 530°C/8h, 535°C/4h, water quenching 66°C), 2-step AA @ (190°C/4h, 50°C/1h (water quenching), 130°C/20h).



**Table 4.14:** Results of wear track width (in the presence of corrosive medium).

<b>Sample ID</b>	<b>Average Track width (mm)</b>	<b>Range (mm)</b>
24-F-8	1.22	1.21-1.22
O-C-8	1.03	1.01-1.04
O-D-8	0.94	0.937-0.947

The friction coefficient was calculated by dividing the tangential force obtained in the tribocorrosion experiment by the normal force applied. This plays a vital role in material removal. Test sample O-D-8 has the lowest coefficient of friction and sample 24-F-8 has the highest coefficient of friction in a corrosive medium. An increase in the friction coefficient will increase the material removal on the surface of the sample.

**Table 4.15:** Coefficient of friction measured during corrosive wear (3.5% NaCl solution).

<b>Sample ID</b>	<b>Coefficient of friction (<math>\mu</math>)</b>
<b>24-F-8</b>	<b>0.16</b>
<b>O-C-8</b>	<b>0.10</b>
<b>O-D-8</b>	<b>0.04</b>

Sample O-D-8 with the best intergranular corrosion resistance and lower levels of pitting (determined by immersion corrosion test) has the lowest wear track width and coefficient of friction compared to 24-F-8 and O-C-8. Sample O-D-8 has better wear resistance than 24-F-8 and O-C-8. Hence, there is a good relationship between the corrosive wear, coefficient of friction and corrosion resistance of the alloy.

### 4.11.3 Open Circuit Potential (OCP) Measurements

The open circuit potential (OCP) recorded during uni-directional pin-on-disk sliding tests is a mixed potential reflecting the state of the unworn disk material and the state of the material in the wear track (disk is the material under investigation). During the tribocorrosion tests, test sample 0-D-8 showed a higher potential of approx. -1.14 V compared to the other two samples (refer to Figure 4.57). This behaviour is due to the presence of the  $\theta$  phase, since the  $\theta$  phase is stable at the higher potential and unstable at the lower potential. So, at more negative potential, sample 0-D-8 shows good corrosion resistance when compared to samples 24-F-8 and 0-C-8. However, OCP measurements made before and after the tribocorrosion tests showed that sample 24-F-8 is more stable at the anodic potential. During the tribocorrosion tests, test sample 24-F-8 showed a potential of approx. -1.16V and sample 0-C-8 showed a potential of approx. -1.18V. Therefore, the sample 24-F-8 shows good resistance to corrosion at the anodic potential, whereas the test sample 0-D-8 shows good resistance to corrosion during accelerated corrosion.

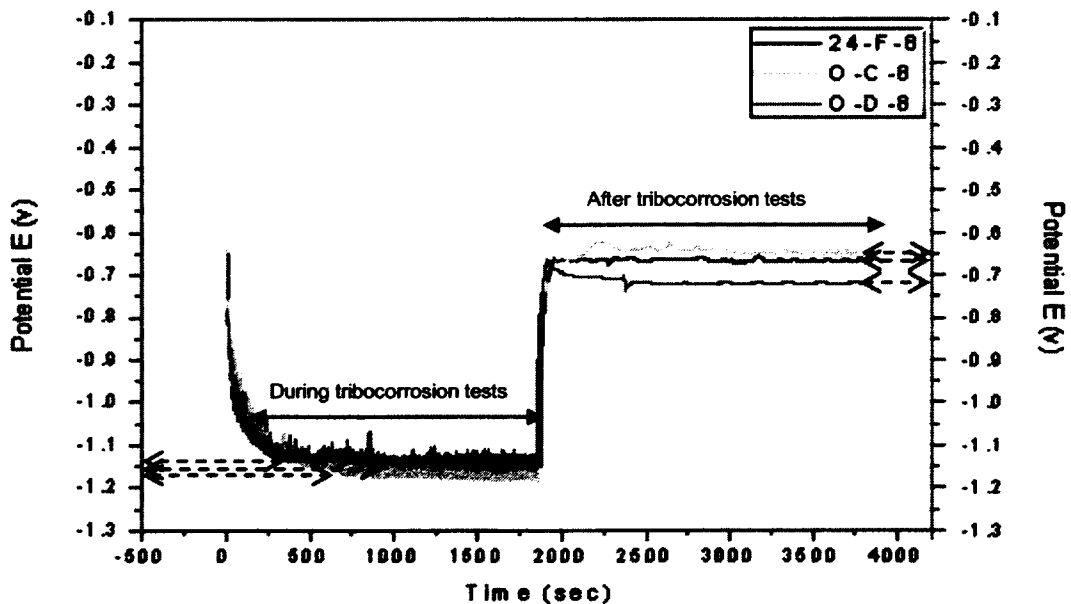


Figure 4.57: OCP varying with time during and after the tribocorrosion experiments.

## **CHAPTER 5: SUMMARY AND CONCLUSIONS**

The following conclusions may be drawn from this study:

1. A heterogeneous distribution of Cu containing intermetallic precipitates present on the grain boundaries of the as-cast sample resulted in severe intergranular corrosion. Improved 3-step ST & 2-step AA treatments result in finer aluminum-copper precipitates compared to the 2-step ST & 1-step AA treatments.
2. Samples with Natural Aging (NA) + Artificial Aging (AA) exhibited higher elongation compared to the Artificially Aged samples with no NA. However, Naturally Aged samples are susceptible to intergranular corrosion. Thus, NA is detrimental for both the one and two step artificially aged B206 test samples as far as the corrosion mode and severity are concerned.
3. High temperature AA was performed to improve the corrosion resistance of the B206 alloy. In both first series (2-step ST, NA (0 & 24 hrs), 1-step AA) and third series (3-step ST, NA (0 & 24 hrs), 2-step AA) heat treatments, high temperature AA decreases the intergranular corrosion depth. Third series heat treatments with longer first step AA time eliminate the intergranular corrosion and resulted in minimum pitting attack. NA aged samples in third series heat treatments are susceptible to both intergranular and pitting corrosion.
4. Comparison of corrosion results for the 3-step ST & 2-step AA with 2-step ST & 1-step AA indicates that a 2-step AA treatment could provide better control of the corrosion mode and severity than 1-step AA. Aging treatments that lead to grain boundary denuded zones and larger intermetallic precipitates along grain boundaries, suffered from intergranular attack. High AA temperature and Longer AA holding time will reduce the amount of intermetallic precipitates in the grain boundaries and also reduce the precipitate free zones near the grain boundaries. This is the reason for high corrosion resistance in sample 0-D-8.

5. Modes of corrosion and severity obtained from the non machined test samples are similar to that of the machined test samples because of the corrosive solution and the removal of the passive layer by aggressive chemical pre-treatment using concentrated  $\text{HNO}_3$  prior to corrosion testing.
6. The range of elongations exhibited for the second series (2-step ST, NA (72 hrs), 1-step AA) heat treatments was very wide, varying from 4 - 20%. High temperature AA and longer AA holding time decreases the elongation in both the second and third series heat treatments. However, high temperature AA and longer AA time gives better corrosion resistance. Thus, it is difficult to produce high corrosion resistance + high elongations for high temperature AA and longer AA times.
7. The 3-step ST and the 2-step AA conditions show a 7.7% maximum improvement in Ultimate Tensile Strength (UTS) and a 5.3% maximum improvement in Yield Strength (YS) compared to the 2-step ST & 1-step AA conditions. The YS and UTS have met the target requirements.
8. Third series heat treatment experiments resulted in elongations between 6 and 14 %. For maximizing the elongation with a 2-step AA treatment, the first step AA temperature and time was more important than the second step AA temperature and time.
9. Samples 24-C-8 and 0-B-8 with shorter first step AA time (0.5h) have smaller dimples (10-15 $\mu\text{m}$ ) while sample 0-D-8 with longer aging time (4h) has larger dimples (up to 25 $\mu\text{m}$ ). An increase in first step AA time from 0.5 to 4 hrs decreased the dimple ruptures and increased the brittle fracture. This may be the reason for higher elongation in samples 24-C-8 and 0-B-8 compared to 0-D-8.
10. OCP measurements made before and after the tribocorrosion tests showed that test sample 24-F-8 is more stable at the anodic potential. However, during the tribocorrosion tests, test sample 0-D-8 shows more corrosion resistance than 24-F-8 and 0-C-8.

11. None of the investigated heat treatment conditions gave rise to the desired properties, namely good overall corrosion resistance, no intergranular and pitting corrosion and elongations  $\geq 10\%$ . Those heat treatments that did not give rise to intergranular corrosion in the immersion testing, generally lead to higher overall corrosion (in the potentiodynamic testing) and lower elongations. Aging treatments that lead to grain boundary denuded zones and larger intermetallic precipitates along grain boundaries, suffered from intergranular attack. Future aging treatments need to be designed which do not produce denuded zones but produce a homogeneous distribution of intermetallic precipitates that do not adversely affect either the ductility or the general corrosion resistance. Larger intermetallic precipitates within the grains appear to lead to deeper pitting.
  
12. The quality index (Q) decreases for longer AA times in the third series heat treatments. Sample 24-C-8 (3-step ST, NA (24hrs), 2-step AA (190°C/0.5h, 50°C/1h, 130°C/30h) has the highest quality index (Q). This is due to the Natural Aging treatment and shorter first step AA time (0.5h).

## **CHAPTER 6: RECOMMENDATIONS FOR FUTURE WORK**

It is recommended that future work concentrate on the following two areas:

1. The resistance against intergranular/pitting corrosion depends on the type and shape of precipitates on the grain boundaries and grain matrix. More extensive SEM/TEM work is required to determine the nature and distribution of the Cu containing intermetallic precipitates on the grain boundaries and in the grain matrix.
2. Future aging treatments needs to be designed to control the size and distribution of Cu-containing intermetallic precipitates that do not adversely affect either the ductility or the corrosion resistance.

## REFERENCES

1. Sigworth, G.K. and Major, J.F. Factors influencing the mechanical properties of B206 alloy castings, in TMS Light Metals 2006. 2006. p. 795-799
2. Major, J.F. and Sigworth, G.K. Chemistry/Property relationships in AA206 alloys. AFS Transactions, 2006. Paper 06-209: p. 12.
3. Tresla, E., Aluminum Casting Alloys and Properties. AFS Transactions, 1964. 72: p. 840-849.
4. Duralumin: Retrieved on 7/23/2008. [cited; Available from: <http://en.wikipedia.org/wiki/Duralumin>.
5. Sigworth, G.K. and Dehart, F. Recent Developments in the High Strength Aluminum-Copper Casting Alloy A206. AFS Transactions, 2003. 11: p. 341-354.
6. Davies, V.d.L., The influence of grain size on hot tearing. The British Foundryman, April 1970. 63: p. 93-101.
7. Pacz, A., Aluminum Alloy Casting and Process of Making the Same. 31 May 1932: U.S Patent, No. 1,860,947.
8. Sicha, W.E. and Boehm, R.C. Effect of titanium on grain size and tensile properties on an Aluminum-4.5% Copper (No.195) Casting Alloy. AFS Transactions, 1948. 56: p. 398-409.
9. Fasoyinu, F.A., Thomson, J.P., Sahoo, M., Burke, P., Weiss, D. Permanent Mold Casting of Aluminum Alloys A206.0 and A535.0. AFS Transactions, 2007. 115, Paper 07-095(2).
10. Wannasin, J., Schwamm, D., Yurko, J.A., Rohloff, C., Woycik, G. Hot Tearing Susceptibility and Fluidity of Semi-Solid Gravity Cast Al-Cu Alloy. Diffusion and Defect Data Pt. B: Solid State Phenomena, 2006. 116-117: p. 76-79.

11. Sigworth, G.K., High Strength casting alloys for automotive applications, in TMS Annual Meeting. 2002. p. 133-140.
12. Dimitrov, N., Mann, J.A., and Sieradzki, K. Copper redistribution during corrosion of aluminum alloys. *Journal of The Electrochemical Society*, 1999. 146 [1]: p. 98-102
13. Van Horn K. R. Aluminum:vol I: Properties, physical metallurgy and phase diagrams. 1967, Metals park, Ohio, USA: ASM Handbook. 425.
14. Deshpande, J.U., The Effect of Mechanical Mold Vibration On the Characteristics of Aluminum Alloys, in *Manufacturing Engineering*. 2006, Worcester Polytechnic Institute. p. 113.
15. Davis, J.R. and Associates, Aluminum and Aluminum alloys. 4 ed. 1993: ASM International. 784.
16. Vadim S. Zolotarevsky, Nikolai A. Belov, and Glazoff, M.V. *Casting Aluminum Alloys*. 2007: Elsevier,. 544.
17. Chitty, A., The effect of Silicon, Manganese, and Iron on the ageing characteristics of Aluminium-Copper Alloys containing 3.0 and 4.5 percent Copper. *Journal of the Institute of Metals*, 1957-58. 84: p. 65-76.
18. Zlaticanin, B., Filipovic, M., Valcic, A., Aleksic, R., Nikolic, S., Radonjic, B, Bosnjak, B. The effects of magnesium and titanium additions on the microstructure and properties of as-cast Al-5% Cu alloys. *Materiali in tehnologije*, 2004. 38(1-2): p. 25-31.
19. Ringer, S.P., Hono, K and Sakurai, T. The effect of trace additions of Sn on precipitation in Al-Cu alloys: an atom probe field ion microscopy study. *Metallurgical and Materials Transactions A (Physical Metallurgy and Materials Science)*, Sept. 1995. 26A(9): p. 2207-17.



20. Radonjic, B., Directionality of cast aluminum structure. *Aluminium*, 1982. 58(11): p. 646-649.
21. Mondolfo, L.F., *Aluminium Alloys: Structure and Properties*: Butterworth and Co (Publishers) Ltd, London 1976. 253.
22. Backarud, L., Chai, G and Tamminen, J. Solidification characteristics of Aluminum Alloys: Vol 2: Foundry alloys, AFS/ SKANALUMINUM. 1990.
23. CLARK., T. Retrieved on March 15, 2009. [cited; Available from: <http://www.mccannsales.com/book/permanentmold.pdf>
24. Light Metals Permanent Mold Casting. U.S Department of Energy. Office of Energy Efficiency and Renewable Energy. Retrieved on March 30, 2009. 2005 [cited; Available from: [http://www1.eere.energy.gov/industry/metalcasting/pdfs/canmet314\\_fs.pdf](http://www1.eere.energy.gov/industry/metalcasting/pdfs/canmet314_fs.pdf)
25. Weijing, L., Shihai, C., Jianmin, H., Chao, X. Effect of Si on the casting properties of Al-5.0%Cu alloy. *Rare Metals*, Dec 2006. 25: p. 133-135.
26. Skallerud, B., Iveland, T and Harkegard, G. Fatigue Life Assessment of Aluminum Alloys With Casting Defects. *Eng. Fracture Mech.*, 1993. 44(6): p. 857-874.
27. Rading, G.O., Li, J and Berry, J.T. Fatigue Crack Growth in cast Al-Cu Alloy A206 with different levels of porosity, in American Foundrymen's Society, Inc. 98th Casting Congress. May 1-4, 1994: Hamilton, Ontario.
28. Sablonniere, H. and Samuel, F.H. Solution Treatment of 319 Alloys containing 0.5wt.%Mg, Part 1 and Part 2. *Int., J. Cast Metals Res.*, 1996: p. 195-211.
29. Wang, G., Bian, X., Wang, W., Zhang, J. Influence of Cu and minor elements on solution treatment of Al-Si-Cu-Mg cast alloys. *Materials Letters*, 2003. 57(24-25): p. 4083-4087.

30. Han, N., Bian, X., Li, Z., Mao, T., Wang, C, Effect of Si on the microstructure and mechanical properties of the Al-4..5%Cu alloys. *Acta Metallurgica Sinica* 2006. 19(6): p. 405-410.
31. Belov, N.A., Eskin, D.G and Aksenov, A.A, *Multicomponent Phase Diagrams: Applications for Commercial Aluminum Alloys*. 2005: Elsevier. 424.
32. Marants, B.D. and Teslya, V.I, Study of the mechanism of manganese precipitation from supersaturated solid solution of aluminum alloys. *Material Science and Heat Treatment*, July-Aug. 1986. 28(7-8): p. 602-4.
33. Davis, J.R. and Associates, *Aluminum and Aluminum alloys*. 4 ed: ASM International Handbook. page no. 34-35.
34. *Heat Treating*. Vol. 4. ASM International Handbook, printed in USA, 1998.
35. Abis, S., Massazza, M., MEngucci, P., Riotinto, G. Early aging mechanisms in a high-copper AlCuMg alloy. *Scripta Materialia*, 2001. 45: p. 685-691.
36. N. Gao, Starink, M.J., Kampa, N., Sinclair, I, Application of uniform design in optimisation of three stage ageing of Al-Cu-Mg alloys. *Journal of Materials Science*, 2008. 42: p. 4398-4405.
37. A. Somoza, Dupasquier, A., Polmear, I.J., Folegali, P., Ferragut, R, *Phys. Rev. B*, 2000. 61: p. 14454-14463.
38. Lumley, R.N., Polmear, I.J and Morton, A.J. in *Proceedings from Materials Solutions Conference*. 5-8 November,2001. Indianapolis, IN, : ASM International.
39. Meissner, K.L., *The artificial ageing of duralumin and super-duralumin*. Institute of Metals, 1930: p. 207-223.
40. Lumley, R.N., Polmear, I.J and Morton, A.J. *Materials Science and Technology*, November 2003. 19(11): p. 1483-1490.

41. Seah Lee Goh, Bourgeois, L., Muddle, B.C., Embury, J.D., Nie, J.F.,. The Effects of Multi-Stage Ageing Treatments on Age Hardening Response of Aluminium Alloys, 2006. Retrieved on April 14, 2009. [cited; Available from: [http://www.arclightmetals.org.au/content/documents/workshop\\_posters/2006/Poster%20PS1-14%20Sally%20Goh.pdf](http://www.arclightmetals.org.au/content/documents/workshop_posters/2006/Poster%20PS1-14%20Sally%20Goh.pdf)
42. R.N. Lumley, Polmear, I.J and Morton, A.J, Control of secondary precipitation to improve the performance of aluminium alloys. Materials Science Forum 396-402, 2002: p. 893-898.
43. Buha, J., Lumley, R.N., Munroe, P,R., Crosky, A.G., in: Nie, J.F., Morton, A.J., Muddle, B.C. in Proc. 9th Int. Conf. on Aluminium Alloys. 2-5 August 2004. Institute of Materials Engineering Australasia Ltd, Brisbane, Australia.
44. Zeren, M., Effect of copper and silicon content on mechanical properties in Al-Cu-Si-Mg alloys. Journal of Materials Processing Technology, 2005. 169: p. 292-298.
45. Sanchez-Majado, S., Torralba, J.M and Jimenez-Morales, A. Assessment of the corrosion behavior of a sintered Al-Cu-Mg alloy in aeronautical environments as a function of the heat treatment. Material Science Forum, 2007. 534-536: p. 497-500.
46. Khoshnaw, F.M. and Gardi, R.H, Effect of aging time and temperature on intergranular corrosion of aluminium alloys. Anti-Corrosion Methods and Materials, 2006. 53 [6]: p. 339-342.
47. Foley, R.T., Localized Corrosion of Aluminum Alloys - A review. Corrosion, 1986. 42 [5]: p. 277-288.
48. Zhang, W. and Frankel, G.S, Transitions between pitting and intergranular corrosion in AA2024. Electrochimica Acta, 2003. 48: p. 1193-1210.

49. Agarwala, V.S. and Murty, Y.V, A controlled-potential corrosion study of Al-4.5Cu alloy in 3.5% NaCl solution. *Metallography*, Oct. 1977. 10(4): p. 451-460.
50. Misra, M.S. and Oswald, K.J, Corrosion Behavior of Al-Cu-Ag (201) Alloy. *Metals Engineering Quaterly*, May 1976. 16(2): p. 39-44.
51. Stress corrosion cracking of Aluminum alloys: Retrieved on April 13,2009. [cited; Available from: <http://www.keytometals.com/Article17.htm>.
52. Haynes, M.J. and Gangloff, R.P, Elevated temperature fracture toughness of Al-Cu-Mg-Ag sheet: characterization and modeling. *Metallurgical and Materials Transactions A (Physical Metallurgy and Materials Science)*, 1997. 28A(9): p. 1815-1829.
53. Galvele, J.R. and Micheli, S.M.d.D. *Corrosion Science*, 1970. 10: p. 795-807.
54. Galvele, J.R., Micheli, S.M.d.D., Muller, I.L., de Wexler, S.B., Alanis, I,L in U.R Evans Conference on Localized Corrosion, National Association of Corrosion Engineers. 1971. Williamsburg, VA.
55. Holroyd, N.J.H., Gangloff, R.P. and Ives, M.B, in *Proceedings of Environment-induced cracking of metals*, National Association of Corrosion Engineers. 1988. Kohler, Wisconsin.
56. Muller, I.L. and Galvele, J.R. Pitting potential of high purity binary aluminum alloys-I. Al-Cu alloys. Pitting and intergranular corrosion. *Corrosion Science*, 1977. 17(3): p. 179-193.
57. Little, D.A., Connolly, B.J. and Scully, J.R. An electrochemical framework to explain the intergranular stress corrosion behavior in two Al-Cu-Mg-Ag alloys as a function of aging. *Corrosion Science*, 2007. 49: p. 347-372.
58. Mondolfo, L.F., *Aluminum Alloys: Structure and Properties*. 1979: Butterworth Inc., Boston.

59. Davis, J.R., Corrosion of Aluminum and Aluminum alloys. 1999: ASM International, Metals Park, OH, USA.
60. Mohammed A. Amin, Abd El Rehim, S., Moussa, S.O., Ellithy, A.S, Pitting corrosion of Al and Al-Cu alloys by  $\text{ClO}_4^-$  ions in neutral sulphate solutions. *Electrochimica Acta*, 2008. 53(18): p. 5644-5652.
61. Ambat, R. and Dwarakadasa, E.S. Studies on the influence of chloride ion and pH on the electrochemical behaviour of aluminium alloys 8090 and 2014. *Journal of Applied Electrochemistry*, 1994. 24: p. 911-916.
62. Kim, Y. and Buchheit, R.G. A characterization of the inhibiting effect of Cu on metastable pitting in dilute Al-Cu solid solution alloys. *Electrochimica Acta*, Feb 1, 2007. 52(7): p. 2437-2446.
63. Blanc, C., Lavelle, B. and Mankowski, G. The role of precipitates enriched with copper on the susceptibility to pitting corrosion of the 2024 Aluminium alloy. *Corrosion Science*, 1997. 39(3): p. 495-510.
64. Foley, R.T., Localized corrosion of Aluminum alloys - A review. *Corrosion*, May 1986. 42(5): p. 277-288.
65. Warraky, A.A.E., El-Aziz, A.M. and Soliman, K.A. Copper redeposition and surface enrichment during the dissolution of Al-Cu alloys in different concentrations of NaCl solution. Part 2 – spectroscopic analysis measurements. *Anti-Corrosion Methods and Materials*, 2007. 54(3): p. 163–172.
66. Campestrini, P., et al., Influence of quench delay time on the corrosion behavior of aluminium alloy 2024 *Materials and Corrosion*, 2000. 51: p. 616-627.
67. Zailiang, C., Yourong, Q. and Shuyi, X. Stress Corrosion Cracking of High Strength Al-Cu-Mg-Si Alloys After Two-Step Aging. *Key Eng Mat*, 1987. 20-28(1-4): p. 2081-2087.

68. Cáceres, C.H., Sokolowski, J.H. and Gallo, P. Effect of ageing and Mg content on the quality index of two model Al-Cu-Si-Mg alloys. *Materials Science and Engineering A (Structural Materials: Properties, Microstructure and Processing)*, Nov 1999. A271(1-2): p. 53-61.
69. H. Westengen and Holta, O. Low pressure permanent mould casting of magnesium- Recent developments, in *International Congress and Exposition, Detroit MI. (Paper c880509)*. 1988, SAE, Warrendale, PA.
70. Tiryakioğlu, M., Campbell, J. and Alexopoulos, N.D. On the Ductility Potential of Cast Al-Cu-Mg (206) Alloys. Article in press. *Materials Science and Engineering: A, Structural materials*, 2008. doi:10.1016/j.msea.2008.10.044
71. Cáceres, C.H., *Microstructure Design and Heat Treatment Selection for Casting Alloys Using the Quality Index*. *Journal of Materials Engineering and Performance*, 2000. 9(2): p. 215-221.
72. M. Tiryakioğlu, Staley, J.T. and Campbell, J. Evaluating structural integrity of cast Al-7%Si-Mg alloys via work hardening characteristics II. A new quality index *Materials Science and Engineering A*, 2004. A368(1-2): p. 231-238.
73. ASTM Designation: G 110 - 92 (Reapproved 2003). *Standard Practice for Evaluating Intergranular Corrosion Resistance of Heat Treatable Aluminum Alloys by Immersion in Sodium Chloride + Hydrogen Peroxide Solution*.
74. Jones, D.A., *Principles and Prevention of Corrosion, Second Edition*. 1996, Prentice Hall (Saddle River, NJ, USA). p148.
75. <http://www.resmat.com/szpunar/equipment.htm>. Retrieved on May 15, 2009.
76. Lumley, R.N., Polmear, I.J. and Morton, A.J. Temper developments using Secondary Aging. *Materials Forum*, 2004. 28: p. 85-95.

77. Buchheit, R.G., Boger, R.K., Carroll, M.C., Leard, R.M., Paglia, C., Searles, J.L, The Electrochemistry of intermetallic particles and localized corrosion in Al alloys. JOM, 2001. 53: p. 29-33, 36.
  
78. Buchheit, R.G, A compilation of corrosion potentials reported for intermetallic phases in aluminum alloys, Journal of The Electrochemical Society, 1995. 142(11): p. 3994-3996.

## **PUBLICATIONS RESULTING FROM THIS WORK**

1. M. Manivannan., J.H. Sokolowski and D.O. Northwood, An investigation of the effect of various heat treatments on the corrosion resistance of a high-strength Aluminum-Copper casting alloy, *Corrosion & Prevention 2008*, Wellington, New Zealand, November 16-19, 2008. Conference Proceedings, ISSN. 1442-0139, Paper 019, p. 1-10.
2. M. Manivannan, D.O. Northwood and J.H. Sokolowski, Developing ductility and resistance to intergranular corrosion for aluminum casting alloy B206. Abstract accepted for "Integrity, Reliability & Failure", 3<sup>rd</sup> International Conference, Porto, Portugal, July 20-24, 2009.



## **VITA AUCTORIS**

**Name:** Madhavan Manivannan

**Place and Date of Birth:** Chennai, India and 06/22/1985

**Education:** Central ElectroChemical Research Institute (CECRI), India  
B. Tech., Chemical and Electrochemical Engineering, 2002-2006

University of Windsor  
M. A. Sc., Engineering Materials, 2007-2009